CHALMERS

UNIVERSITY OF TECHNOLOGY

Spalling in Concrete Subjected to Shock Wave Blast

Fracture due to cyclic crack propagation

Master's Thesis in the Master's Programme Structural Engineering and Building Technology

ERIK FLINCK
MARTIN OLSSON

MASTER'S THESIS BOMX02-16-26

Spalling in Concrete Subjected to Shock Wave Blast

Fracture due to cyclic crack propagation

Master's Thesis in the Master's Programme Structural Engineering and Building Technology

ERIK FLINCK

MARTIN OLSSON

Department of Civil and Environmental Engineering
Division of Structural Engineering
Concrete Structures
CHALMERS UNIVERSITY OF TECHNOLOGY

Göteborg, Sweden 2016

Spalling in Concrete Subjected to Shock Wave Blast
Fracture due to cyclic crack propagation

Master's Thesis in the Master's Programme Structural Engineering and Building Technology

ERIK FLINCK

MARTIN OLSSON

Department of Civil and Environmental Engineering
Division of Structural Engineering
Concrete Structures
Chalmers University of Technology
SE-412 96 Göteborg
Sweden
Telephone: + 46 (0)31-772 1000

Spalling in Concrete Subjected to Shock Wave Blast

Fracture due to cyclic crack propagation

Master's thesis in the Master's Programme Structural Engineering and Building Technology

ERIK FLINCK
MARTIN OLSSON
Department of Civil and Environmental Engineering
Division of Structural Engineering
Concrete Structures
Chalmers University of Technology

ABSTRACT

Over the past 20 years, Chalmers University of Technology has been conducting research on structures subjected to explosions. One field within this research relates to the structural resistance to withstand spalling, which is a fracture phenomenon where material breaks lose at the opposite side from the loaded one. The conventional method of evaluating spalling, developed in the late 1980s, suggested that spalling in concrete occurs when a compression wave reflects at the free side of the structure and causes tensile stresses equal to the tensile strength. This method on how to evaluate spalling was recently questioned by PhD student Jonas Ekström, who instead suggested that spalling takes place during cyclic loading/unloading, where material ductility will influence the structural response. This results in that spalling does not occur instantaneously nor necessarily at the same location as predicted in the conventional theory.

To support his claim, Ekström developed a numerical routine which showed that spalling does not occur instantaneously as the tensile stress reaches the tensile strength, but rather over cyclic loading/unloading where material ductility is included. For this reason, the objective of this thesis focuses mainly on providing improved understanding of the spalling phenomenon, as well as supporting the current research project by performing a parametric study of this numerical model.

This thesis provides an overview of the spalling phenomenon. It further highlights the difficulties in representing a shock wave in numerical modelling. The results from the parametric study show that the shock wave properties will influence the structural response significantly, as well as that some parameters, such as the damping and number of elements, cannot be parameterized without causing complications in the results. Further, preliminary results show that the depth of spalling does not change when including non-linearity in both strain softening and pressure time gradient. A main concern with the numerical model throughout this entire thesis is the inconsistency in fracture zone. More or less all results in the parametric study have a distribution of inelastic strains not consistent with the assumed fracture zone, which is problematic. Therefore, this thesis presents a method on how to partly adjust for this inconsistency.

Key words: Spalling, concrete, spalling depth, wave propagation, shock wave, strain softening, pressure-time gradient, inelastic strains, fracture zone

Utstötning i betong belastad av stötvåg
Brott på grund av cyklisk sprickutbredning

Examensarbete inom masterprogrammet Structural Engineering and Building
Technology

ERIK FLINCK
MARTIN OLSSON
Institutionen för bygg- och miljöteknik
Avdelningen för konstruktionsteknik
Betongkonstruktioner
Chalmers tekniska högskola

SAMMANFATTNING

Under de senaste tjugo åren har Chalmers Tekniska Högskola forskat kring explosionsbelastade konstruktioner. Ett ämne inom denna forskning relaterar till konstruktioners kapacitet att motstå utstötning, vilket är ett brottfenomen där material slits loss på motsatt sida av den belastade. Den konventionella metoden för att utvärdera utstötning, utvecklad under sent 1980-tal, föreslår att utstötning sker när en tryckvåg reflekteras på en fri yta och skapar dragspänningar som uppnår draghållfastheten. Denna metod att utvärdera utstötning på ifrågasattes nyligen av doktorand Jonas Ekström, som istället menar på att utstötning sker under cyklisk på- och avlastning, där materialets seghet påverkar strukturens beteende. Detta resulterar i att utstötning inte inträffar omedelbart när dragspänningen uppnår draghållfastheten. Det innebär vidare att utstötning nödvändigtvis inte sker i samma del av strukturen som antas i den konventionella teorin.

För att stödja sin hypotes utvecklade Ekström en numerisk modell, vilken visade på att utstötning faktiskt inte inträffar momentärt utan snarare under cyklisk på- och avlastning där materialets seghet är inkluderat. Av denna anledning fokuserar detta examensarbete på att förse läsaren med en ökad förståelse om utstötning, såväl som att stödja den pågående forskningen genom att bland annat tillhandahålla en parametrisk studie på Ekströms numeriska modell.

Mot denna bakgrund, tillhandahåller detta examensarbete en genomgång av utstötning som fenomen. Vidare visar den på svårigheterna i att återskapa en stötvåg i en numerisk modell. Resultaten från parameterstudien visar att en stötvågs egenskaper påverkar strukturens beteende betydligt, och att några parametrar, såsom systemets dämpning och antalet element, inte kan varieras för mycket utan att orsaka problem i resultaten. Vidare så tyder preliminära resultat på att utstötningsdjupet inte förändras när icke-linjärt töjningsmjuknande och icke-linjär tryck-tid gradient inkluderas. Slutligen ifrågasätts resultaten från den numeriska modellen med anledning av brottzonens inkonsekvens. Mer eller mindre alla resultat i parameterstudien visar på en fördelning av icke-elastiska töjningar som inte motsvarar den antagna brottzonen. Av denna anledning presenterar detta arbete en metod som kan användas för att delvis justera denna inkonsekvens.

Nyckelord: Utstötning, betong, utstötningsdjup, vågutbredning, stötvåg, töjningsmjuknande, tryck-tid gradient, icke-elastisk töjning, brottzon

Contents

Preface

This Master's thesis was carried out between January 2016 and June 2016 at the Department of Civil and Environmental Engineering, Division of Structural Engineering, at Chalmers University of Technology. The research within this thesis is mainly based on earlier work at Chalmers by PhD student Jonas Ekström and Adjunct Professor Morgan Johansson at ÅF Infrastructure. It can also be considered to be a continuation of parts of Ekström's licentiate thesis.

Firstly, we would like to thank our supervisor and examiner Morgan Johansson for invaluable weekly guidance and assistance. We would also like to thank and express our gratitude to Mattias Carlsson at ÅF Infrastructure in Göteborg as well as Jonas Ekström for valuable input throughout the entire project.

Further, we would also like to thank our opponents, Anton Lindqvist and Henrik Nilsson, for valuable input during the entire process.

Lastly, we would like to thank ÅF Infrastructure in Göteborg, and their employees, for giving us the chance to take part in this field of research.

Gothenburg, June 2016
Erik Flinck and Martin Olsson

Notations

Roman upper case letters

A	Area
C	Damping
C_d	Cratering depth
E	Young's modulus
E_{dyn}	Dynamic Young's modulus
E_{qs}	Quasi-static Young's modulus
F	Load
F_{dyn}	Dynamic load capacity
F_{sta}	Static load capacity
G_f	Fracture energy
$G_{f,dyn}$	Dynamic fracture energy
$G_{f,qs}$	Quasi-static fracture energy
K	Stiffness matrix
L	Concrete thickness, specimen length
M	Mass matrix
N	Number of elements
P_{peak}	Peak pressure
P_r^{+}	Reflected overpressure
P_s^{+}	Incoming overpressure
S_d	Spalling depth
U_p	Particle velocity
W	Equivalent amount of TNT

Roman lower case letters

c	Pressure wave velocity
$f_{cc,cube}$	Characteristic compressive cube strength of concrete
f_{ct}	Characteristic tensile strength of concrete
f_{dyn}	Dynamic tensile strength of concrete
f_t	Tensile strength of concrete
$f_{t,qs}$	Quasi-static tensile strength of concrete
$f(w)$	Crack softening function
h	Time interval
i	Impulse intensity
i^{+}	Positive phase of impulse density

r	Distance from explosion source
r_K	Spalling reduction factor
t	Time, structural element thickness
t_0	Initial time
t_{dur}	Load duration
u	Displacement
$\dot{u}$	Velocity
$\ddot{u}$	Acceleration
q	Internal force
v	Velocity
w	Crack opening
w_u	Ultimate crack opening
x	Coordinate

Greek upper case letters

ΔL	Elongation
$\Delta \sigma$	Change in stress
Δx	Equalization distance of pressure wave
Λ	Reflexion coefficient

Greek lower case letters

δ^+	Damage parameter
ε	Strain
$\dot{\varepsilon}$	Strain rate
ε_{inel}	Inelastic strain
ε_{tot}	Total strain
ε_u	Ultimate strain
ν	Poisson's ratio
ξ	Damping ratio
ρ	Density
σ	Stress
ψ	Spalling parameter
ω_{max}	Highest response frequency

1 Introduction

1.1 Background

Over the past 20 years, the Division of Structural Engineering at Chalmers has been conducting research within structures exposed to explosions. The application of this research focuses on civil structures with increased demands to withstand explosions in the urban environment. Spalling, where material breaks lose at the opposite side from the loaded one, is an important phenomenon that a structure has to withstand with regard to nearby explosions. One way of evaluating the structural response of structures subjected to shock wave blast from explosions was presented by McVay (1988). There, it is suggested that spalling in concrete occurs when a compression wave with negative time-pressure gradient reflects on the free side of the wall and causes tensile stresses equal to tensile strength of the material.

This model of how to evaluate spalling in concrete was recently further developed in a Licentiate thesis by PhD student Jonas Ekström at Chalmers. Ekström (2016) suggests that the conventional way of evaluating spalling can be inaccurate since it does not consider material ductility. Ekströms hypothesis states that the effect of material ductility is that spalling cracks do not occur instantaneously when tensile strength is reached, as conventionally assumed. Another important discovery presented by Ekström is that the spalling cracks do not necessarily appear at the same position as for fully brittle materials. Further development within this field is therefore necessary for a better understanding of the spalling phenomenon.

1.2 Aim

The aim of this master's thesis is to improve the understanding of the underlying physics of the phenomenon spalling in concrete due to a nearby explosion. Further, a related aim is to support a current PhD research project at Chalmers, which recently presented a hypothesis on how to evaluate this phenomenon. The support consists of a further development and study of a numerical routine developed in Ekström (2016), for which the aim is to determine whether the preliminary results presented by Ekström are repeated and reliable.

An additional aim is to provide the reader with overall knowledge regarding how spalling due to blast loading can be evaluated and tested experimentally, as well as how it can be estimated empirically.

1.3 Methodology

To provide sufficient understanding of spalling in concrete, a literature study is carried out. This literature study extends further to provide understanding in experimentally and empirically methods on how to evaluate spalling in concrete. This part of the thesis is mainly based on literature by McVay (1988), Ekström (2016) and Johansson (2013). Additional literature is gathered elsewhere when required.

In order to support the current research project with additional studies on the numerical Matlab routine developed by Ekström, a parametric study is carried out in order to determine whether the preliminary results are repeated. This parametric study consists of variations in geometry, load properties and material properties.

In addition to the parametric study, a detailed description of how the model operates and evaluates spalling is included. Further development of the model is also presented by including non-linearity in both crack softening and pressure-time gradient. This is mentioned in Ekström's licentiate thesis as an important part of further studies.

1.4   Limitations

Throughout the numerical analysis in this thesis, blast loading is considered to have a plane pressure distribution from the source. This can only be considered as true if the point of observation is sufficiently far away from the explosion. If a non-plane pressure distribution is to be implemented, a two or three dimensional model is required instead of a one dimensional.

The numerical routine is limited in such way that no consideration is taken to strain rate effects due to the complexity of accurately determine the material properties at strain rates corresponding to blast loading. The exclusion of strain rate makes it difficult to compare the results from the numerical analysis with results from experiments. For this reason, such a comparison is neglected in this thesis. This limitation is important to mention, since research in general is preferable if it is possible to compare the results with experiments.

The parametric study is limited in such way that only one parameter at a time is varied. One may reason that a parametric study should include multiple parameter variations. This is, however, beyond the scope of this thesis.

1.5   Outline of the report

Chapter 2 is a theory chapter based on a literature study. The purpose of this chapter is to provide the reader with sufficient understanding of the spalling phenomenon. Summarily, this chapter covers understanding in loads from by explosions, material overview and fracture due to blast loading.

Chapter 3 contains examples of how to evaluate spalling experimentally. This is a continuation of the literature study in Chapter 2.

Chapter 4 includes the numerical analysis. This chapter contains an overview of the numerical model developed by Ekström as well as the results from the parametric study. Further development of the numerical model with corresponding results are also presented. Lastly, it includes a method on how to adjust for inconsistency, obtained in the fracture zone.

Chapter 5 includes a discussion of the most important observations and results. In addition to this chapter, discussions are also included in Chapter 4 along with the presented results.

Chapter 6 includes and summarizes the most important conclusions from the entire thesis. This chapter contains suggestions on further studies and developments of the presented results.

2   Theory

2.1   Loads caused by explosions

Loads on structures can roughly be separated in three categories: static, quasi static and dynamic loading, Ekström (2016). What differentiates these different types of loads is the duration of how long they act on the structure. A dynamic load is either applied repeatedly on the structure or applied on the structure faster in relation to a static load, while the quasi static is applied slower on the structure. This load duration will influence both the global and local response of the structure, which will yield in different design approaches for the different load types. An explosion is a dynamic load with very short load duration, and the blast wave generated by the explosion can have load durations in the range of milli- and microseconds, Gebekken *et al.* (2001).

2.1.1   Shock wave in air

An explosion in air gives rise to a sudden release of energy to the surroundings. This release of energy is due to a volumetric expansion of the matter which causes an overpressure that forces the surrounding air volume away. This overpressure can be described as a shock wave, which propagates away from the source with supersonic speed. The blast wave front is followed by a region where pressure, temperature, density and the speed of the air particles are much higher than the air ahead of the blast wave front. The blast wave front propagates spherically from the epicentre of the explosion, see Figure 2.1, and decreases successively in intensity with increasing distance from the source, Johansson and Laine (2012a).
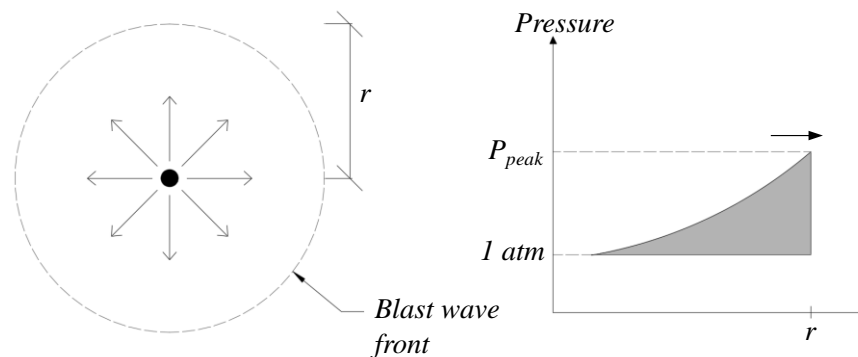
Figure 2.1   Illustration of shock wave propagation, based on Johansson and Laine (2012a).

There are several important parameters used to describe the propagation of a shock wave. Terms such as pressure, impulse intensity and duration are important when describing how an explosion expands from the source, Johansson and Laine (2012a). To illustrate this, consider the example given in Figure 2.2 with an explosion and a reference point *A* at a distance *r*.
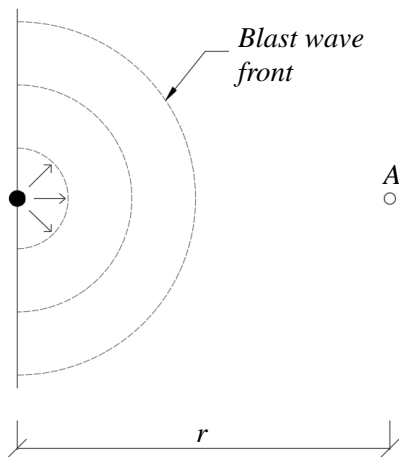
Figure 2.2   Example of explosion.

Almost instantaneously after detonation the pressure rises from atmospheric to a peak pressure, Johansson and Laine (2012a). There is however a certain arrival time for the shock wave to reach point *A*. The peak pressure at point *A* then decreases exponentially with time to atmospheric pressure, after which a negative pressure acts in point *A*. Figure 2.3 shows the principle pressure-time relation for point *A*.
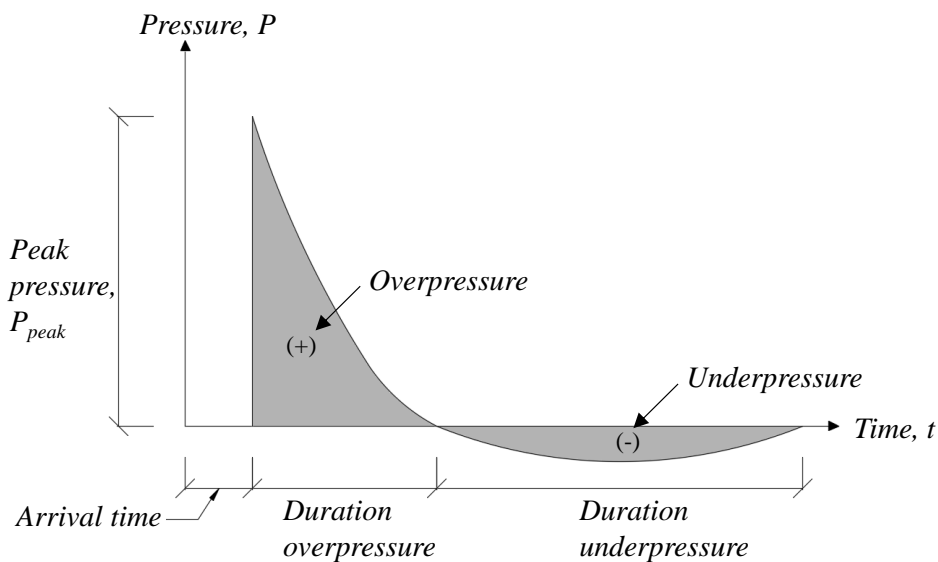
Figure 2.3   Principle pressure time relation for a shock wave. Based on Johansson and Laine (2012a).

In a structural analysis the pressure-time relation, shown in Figure 2.3 is often simplified to a linear decrease where the negative pressure is ignored, Johansson and Laine (2012a). The pressure-time relation for the example in Figure 2.2 could therefore be described as shown in Figure 2.4.
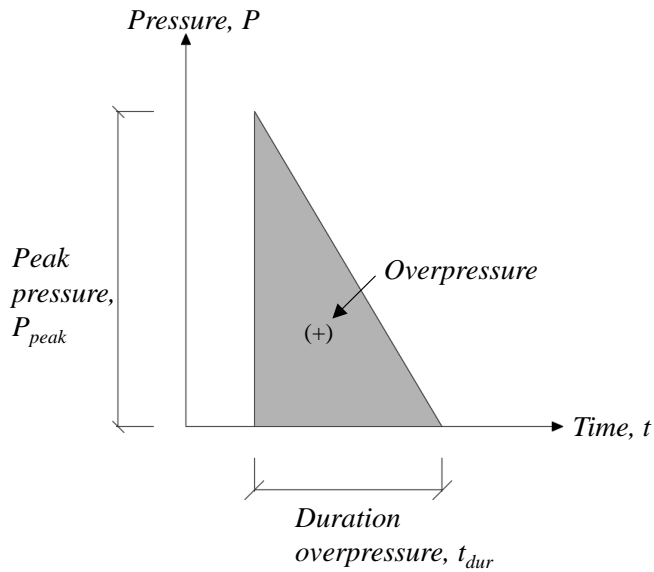
Figure 2.4   Simplified pressure-time relation.

By combining the pressure and the time duration, one can define the impulse intensity as the area under the pressure-time graph, i.e.

$$i = \int_{t_0}^{t} P(t)dt \tag{2.1}$$

The impulse intensity i together with the peak pressure P_{peak} and duration time t_{dur} are important factors when describing propagation of a shock wave, Johansson and Laine (2012a). Figure 2.5 shows two examples of simplified pressure-time relations with the same peak pressure, but different impulse intensity.
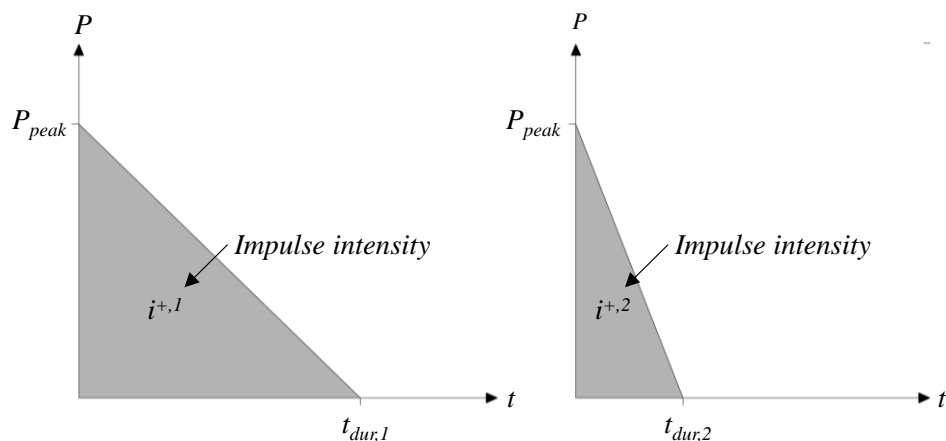
Figure 2.5   *Illustration and definition of impulse intensity as the area under the pressure-time relation. Comparison of two cases with same P_{peak} but different load duration.*

2.1.2   Reflexion of shock wave

The propagation of a shock wave in urban environments does not only dependend on the magnitude of the explosion and the distance to the observation point. There are

also phenomena such as confinement, diffraction and reflexion, Johansson and Laine (2012b). This thesis will briefly treat the latter.

Reflexion occurs when a shock wave hits a denser medium. At this point, the characteristics of the shock wave can change drastically, Johansson and Laine (2012a). Therefore, it is important to understand the principle of reflexion, i.e. how an incoming shock wave becomes a reflected shock wave. Figure 2.6 shows the principle of this, where P_s^+ denotes the incoming overpressure and P_r^+ the reflected overpressure.
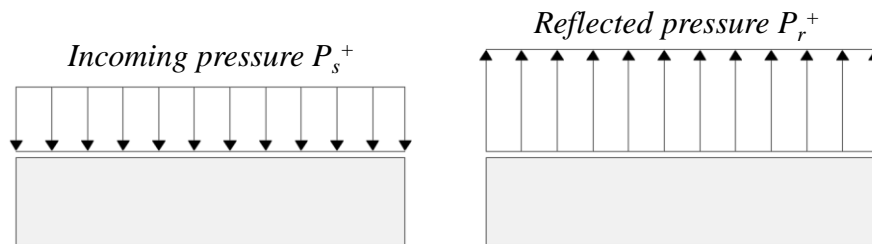

Figure 2.6   Illustration of a) incoming overpressure b) reflected overpressure, based on Johansson and Laine (2012a).

The relation between the reflected overpressure and the incoming overpressure can be established using a reflexion coefficient Λ, Johansson and Laine (2012a). Hence, the reflected overpressure is determined as the incoming overpressure multiplied with the reflexion coefficient. The value of the reflexion coefficient varies dependent on the incoming overpressure, which is illustrated in Figure 2.7.
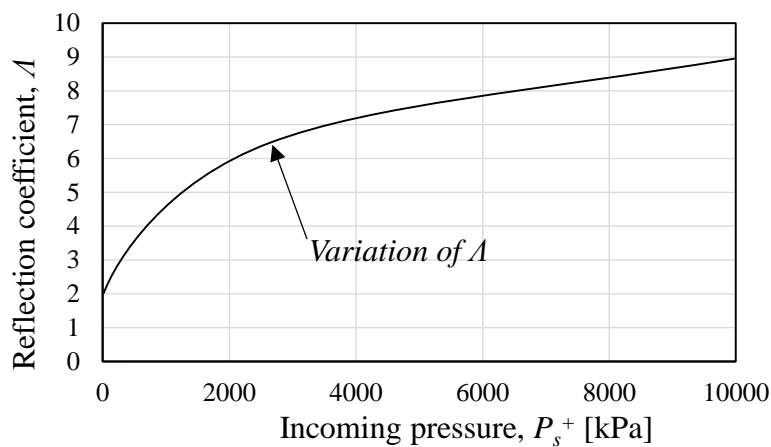
Figure 2.7   Relation between reflection coefficient and the incoming overpressure, based on Johansson and Laine (2012).

The reason why the concept of reflexion is important when studying blast loaded structures is that the applied overpressure to the structure is not the incoming overpressure, but rather the reflected overpressure.

2.1.3   Influence of pressure profile due to distance

The magnitude of the peak pressure is not the only important factor when discussing the distance between the explosion and observation point. Another factor is the shape of the shock wave at different distances. To illustrate this, consider the scenario in Figure 2.8 where a principle shock wave profiles and resulting pressures are illustrated in a reference area at different distances from the explosion.
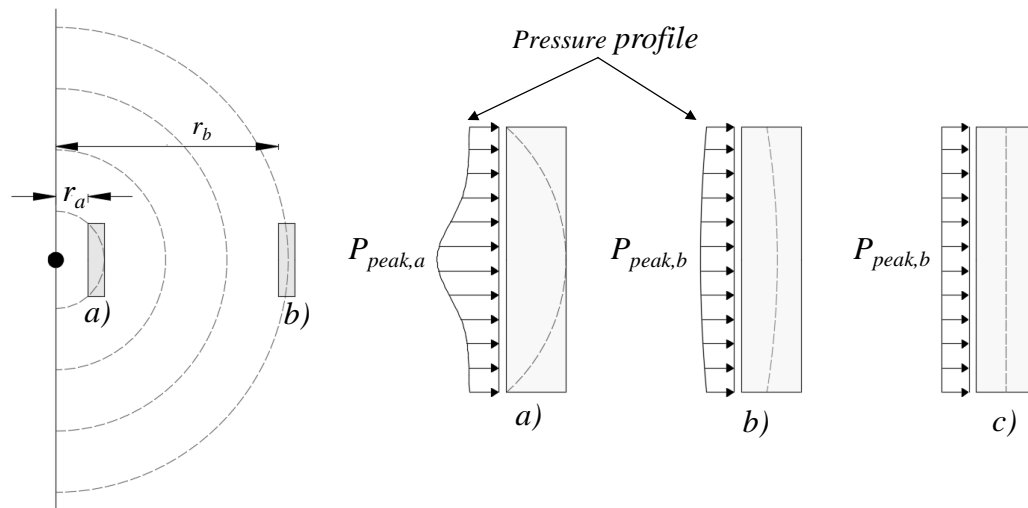
Figure 2.8   *Illustration of different shock wave profiles at different distances:*
a) shock wave profile at close range, b) shock wave profile at longer
range and c) simplification of case b).

The conclusion of Figure 2.8 is that the shock wave flattens out with increased distance from the epicentre of the explosion. The pressure profile illustrated in Figure 2.8c is therefore a simplification since the shock wave can never be considered to be completely flat. However, the important conclusion is that one may consider the pressure profile to be flat unless the explosion occurs in absolute proximity to the structural element. Thus, in further sections there will be a distinction between two different load cases: nearby explosion and contact detonation, which are illustrated in Figure 2.9.
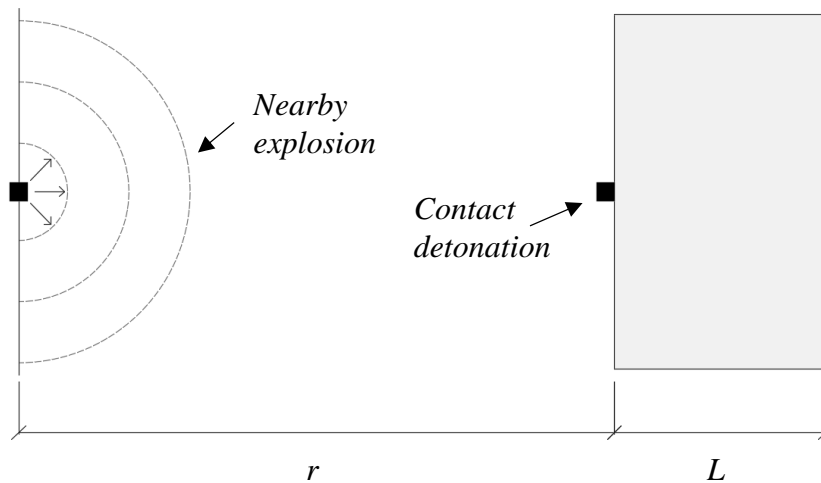
Figure 2.9   *Distinction between nearby explosion and contact detonation.*

2.1.4   TNT as a measurement of released energy

Because the unit of energy released is defined as work, the SI-unit for energy release is Joule. For practical reasons though, a different unit for quantifying the energy released by an explosion is commonly used. "Weight of TNT" describes the approximate amount of energy released in a detonation of 1000 kg TNT. The effect obtained by a detonation of 1 kg TNT is equivalent to an energy amount of 4.6 MJ,

Johansson and Laine (2012a).To give a picture of the amount of TNT that can be confined in different containers and the distance at which these containers can cause minor damage on structures, see Table 2.1Table 2.1Table 2.1   Quantities of different containers with TNT. Based on NCTC (2014).

Explosive source		Amount of TNT [kg]	Minor damage on buildings [m]
Pipe Bomb		2.3	21
Briefcase bomb		23	46
Sedan		227	98
Small truck		4 545	263
Trailer truck		27 273	475

2.2   Structures subjected to blast wave

2.2.1   Overview

The structural response of blast loaded structures is important to understand in order to evaluate fracture phenomena related to this type of loading. The blast wave generated from an explosion will transfer from the air to the structure and create stresses in the material, Leppänen (2012). This can further be described by studying wave propagation in matter.

2.2.2   Wave propagation in matter

Leppänen (2012) describes how to consider wave propagation in matter using an example of a loaded bar, see Figure 2.10. By using a bar and a fixed wall it can be illustrated how waves propagate by studying the state of the bar at different steps in time. The bar is subjected to a shock wave at time t_0, which is achieved by giving the bar an initial velocity v_0 and allowing it to collide into the fixed rigid wall. Leppänen then illustrate the state of the bar for different times $t > t_0$, which shows how the bar is subjected to alternating tension/compression. The state of the bar is determined by looking at wave propagation, stress and velocity at seven different time-steps, which is illustrated in Figure 2.10.
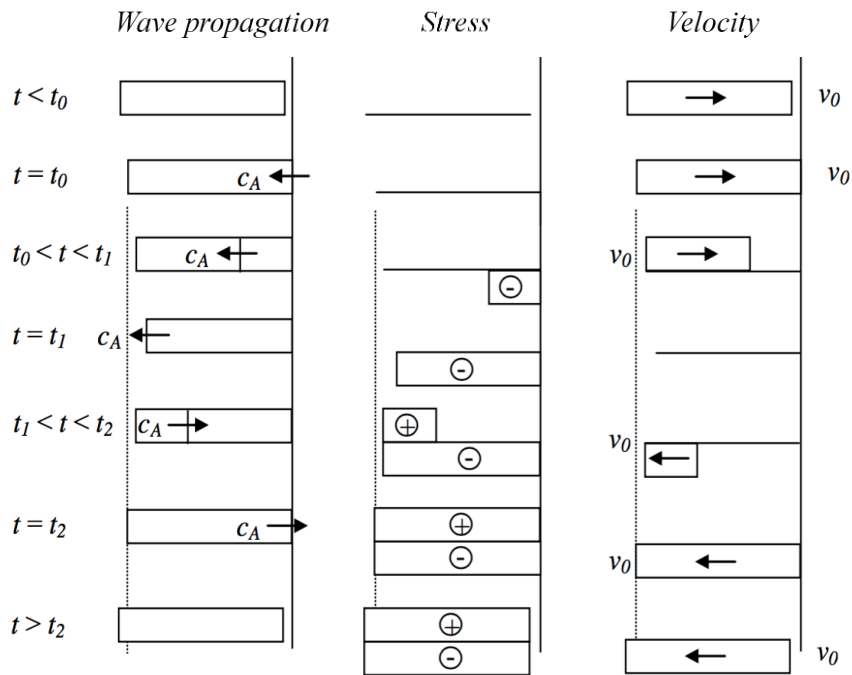
Figure 2.10   Wave propagation, stresses and velocity of the bar. Based on Leppänen (2012).

$t < t_0$:

The bar is initially given a velocity v_0. At this time, before collision with the wall, there are no stresses and no wave propagation in the bar.

$t = t_0$:

State of the bar at collision with the wall. The right side of the bar will stop since the wall is considered to be fixed and fully rigid. This will create a change in velocity for the right most point in the bar causing a compression wave to start propagate to the left with speed c_A. This wave, though, is still at the right most point of the bar meaning that the bar can still be considered stress free.

$t_0 < t < t_1$:

The compression wave continues to propagate to the left in the bar. At this state, compression stresses will appear to the right of the wave front, while the left side of the wave front still is "unknown" of the impact with the wall. This means that this side of the bar will continue with initial velocity v_0 towards the wall.

$t_1 < t < t_2$:

At the left side of the bar, the compression wave reflects and becomes a tension wave of equal magnitude, propagating towards the right side of the bar, which will create tensile stresses behind the wave front. This will also result in change of velocity v_0 for the part of the bar behind the wave front.

$t = t_2$:

The tension wave reaches the right side of the bar. The tension wave has caused tensile stresses in the entire bar. However, this tensile stress will cancel out the compression stress resulting in a stress free bar. The entire bar is also given initial velocity v_0, but now in the opposite direction.

t > t₂:

The stress free bar moves with velocity v_0 in opposite direction from $t < t_0$.

What Figure 2.10 is meant to demonstrate is that when a body is subjected to a shock wave, the state of stress and velocity within the body alternates due to shock wave propagation.

2.2.3 Particle velocity

As the shock wave velocity c describes how fast the shock wave front travels through a medium, the particle velocity U_p describes the compression and separation on a material level, Leppänen (2012). The concept of particle velocity is briefly treated in Figure 2.10, and will be further described in this section.

The concept of particle velocity is described using shock wave propagation seen in Figure 2.11, where two arbitrary materials *A* and *B* are studied, Leppänen (2012). The given shock wave c_A in material *A*, see Figure 2.11a, will generate a particle velocity $U_{p,I}$ in the material that propagates in the same direction as the shock wave. Further, as the shock wave reaches the interface between *A* and *B*, both a reflected and transmitted shock wave is generated. Figure 2.11c illustrates the reflected and transmitted particle velocity, the magnitude of which depends on the material properties for material *A* and *B*.
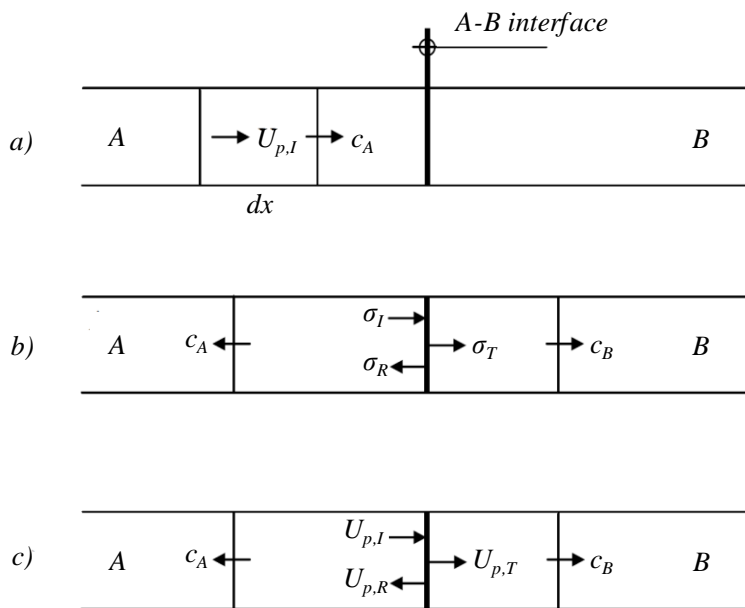
Figure 2.11   Schematic illustration of particle velocity, Leppänen (2012).

Leppänen (2012) further derives the magnitude of the stress, based on that the impulse is equal to the change in momentum, such as

$$\sigma = \rho \cdot c \cdot U_p \tag{2.2}$$

where ρ is the density, c is the shock wave velocity and U_p is the particle velocity. Further, continuity conditions at the interface between material A and B yields that

$$\sigma_I + \sigma_R = \sigma_T \qquad (2.3)$$

$$U_{pI} + U_{pR} = U_{pT} \qquad (2.4)$$

The incoming, reflected and transmitted particle velocities can be described using equation (2.2). By expressing the particle velocities based on equation (2.2) and insert them in equation (2.4), Leppänen derives expressions for how the reflected and transmitted particle velocities depends on the incoming particle velocity such as

$$\frac{U_{pT}}{U_{pI}} = \frac{2\rho_a c_a}{\rho_a c_a + \rho_b c_b} \qquad (2.5)$$

$$\frac{U_{pR}}{U_{pI}} = \frac{\rho_a c_a - \rho_b c_b}{\rho_a c_a + \rho_b c_b} \qquad (2.6)$$

In the special case where the impedance $\rho_B c_B$ is zero, i.e. the interface between *A* and *B* can be considered to be a free edge, the relation between transmitted and reflected particle velocity becomes

$$\frac{U_{pT}}{U_{pI}} = 2 \qquad (2.7)$$

$$\frac{U_{pR}}{U_{pI}} = 1 \qquad (2.8)$$

In spalling evaluation the case with a free edge is considered, why the underlying theory presented in this chapter is of importance when describing stress distribution and particle velocities in blast loaded structures.

2.2.4 Stress-distribution in blast loaded structures

The purpose of Figure 2.10 is to illustrate a general approach for how to consider wave propagation in an arbitrary material. This thesis, however, focuses more on wave propagation in structural elements caused by explosions. So instead of using a general approach of wave propagation as in Figure 2.10, this section will more in detail describe the response when subjecting a structural element to an explosion. To illustrate this, the example in Figure 2.12 is used, where a structural element with thickness *t* is placed at a distance *r* from a nearby explosion
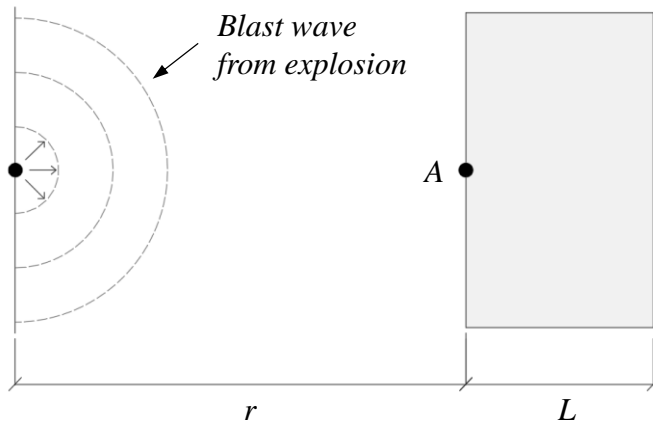
Figure 2.12   Model used to illustrate stress distribution in blast loaded structural elements.

At the edge of the structural element, in point *A*, the pressure caused by the nearby explosion will have a pressure-time relation as discussed in Section 2.1.1. This principle pressure-time relation is illustrated in Figure 2.13. The actual peak pressure acting on the edge of the structure, point *A,* is in analogy with Section 2.1.2 dependent on the actual reflected overpressure rather than the incoming. A flat pressure profile is assumed since the explosion is not considered to be placed in absolute proximity to the element, and a linear pressure-time relation is assumed.
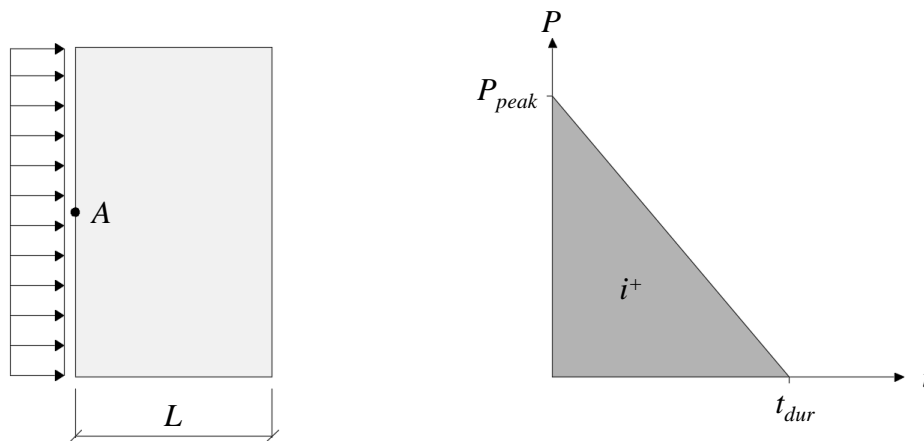
Figure 2.13   Pressure-time relation at the edge of a structural element.

The shock wave from the overpressure at the edge of the structure will cause a shock wave to propagate within the structural element, Johansson (2013a). This shock wave will propagate with a velocity *c* determined by equation (2.9). For concrete, the velocity is approximately 3500 m/s.

$$c = \sqrt{\frac{E}{\rho}} \tag{2.9}$$

The blast load that impacts the structural element can be distinguished between short load duration and long load duration. Short load duration is here defined as a load with shorter extension than twice the thickness of the structural member. Long load duration is, consequently, defined as a load with greater extension than twice the thickness of the structural member. This is illustrated in Figure 2.14.
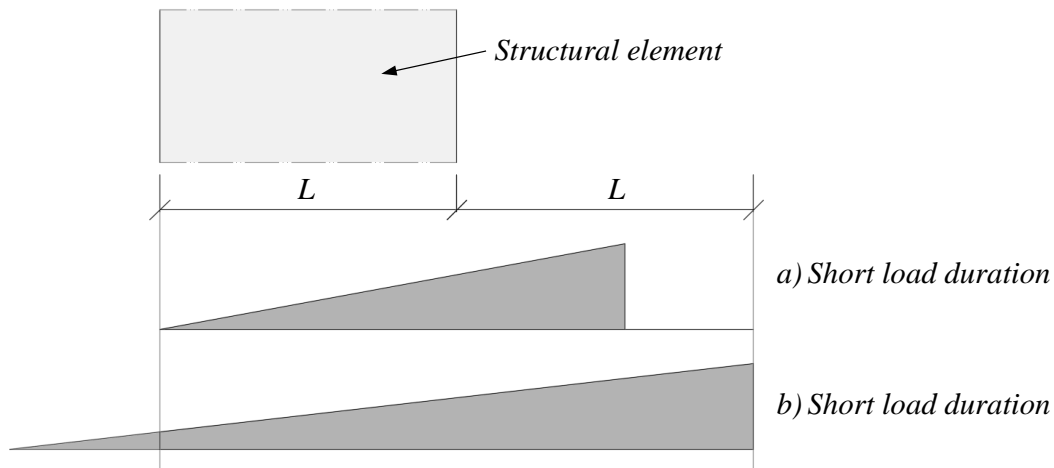
Figure 2.14   Illustration of a) short duration load and b) long duration load.

The main difference between short and long load duration is how the stresses develop and distribute within the structural element. Figure 2.15 shows principle shock wave propagation for short load duration in an arbitrary structural element for three different steps in time. The principle of shock wave propagation in a structural element is summarized in Figure 2.15.
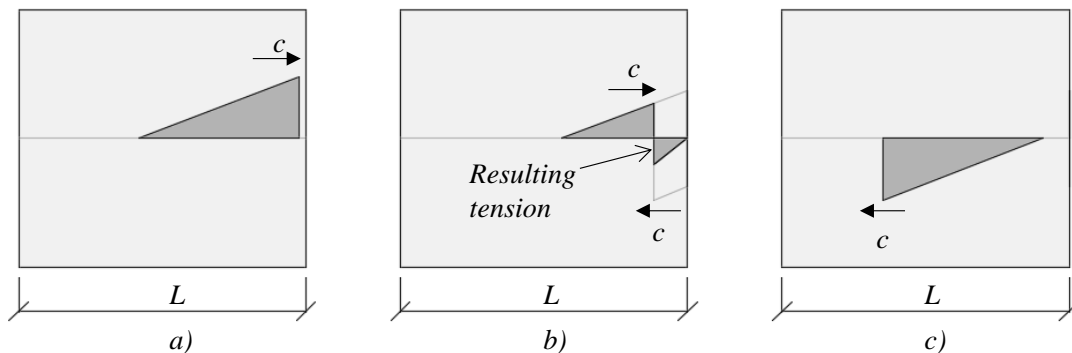
Figure 2.15   Shock wave propagation and stress distribution in blast loaded structures. Short load duration.

a) The shock wave is transferred from the air into the structure and propagates with speed c towards the free edge in the structure.

b) Upon reaching the free edge the compressive shock wave reflects and propagates as a tension wave in opposite direction. If air is considered to be a material with infinitesimal impedance, the entire magnitude of the peak pressure will be reflected, see equation (2.6). Due to the gradient of the shock wave, a net tensile stress is found over the region where the compressive wave and the tension wave interact.

c) When the entire compressive shock wave has reflected, a tension wave propagates towards the other free edge in the structure.

The principle of how the compressive shock wave propagates and reflects at the free edge is the same for a longer load duration, which is illustrated in Figure 2.16. Important here, though, is to compare the resulting stress wave after reflection, see

Figure 2.15b and Figure 2.16b. Hence, the magnitude of the net tensile stress after reflection will decrease as the load duration increases if the same peak stress is assumed.
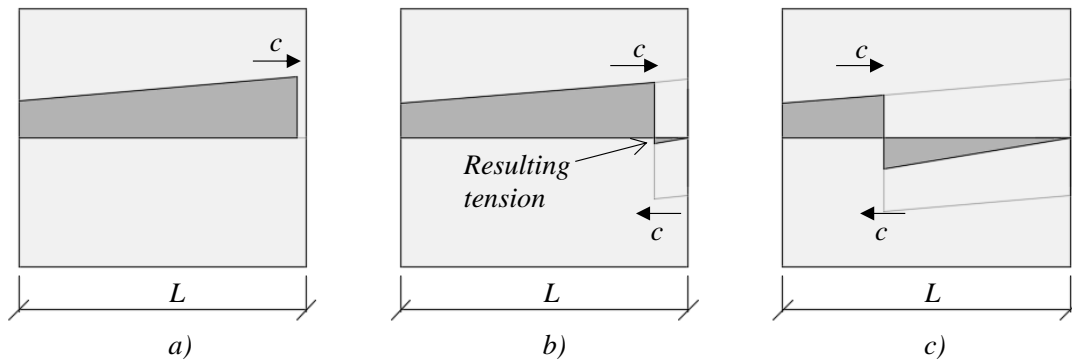
Figure 2.16   Shock wave propagation and stress distribution in blast loaded structures. Long load duration.

Furthermore, the changed state of stress seen in Figure 2.16b will cause a change in particle velocity. Since the change in stress $\Delta\sigma$ is constant after reflection, as seen in Figure 2.17a, the particle velocity after reflection will be constant in the zone where the compression and tension waves interact. However, the magnitude of the particle velocity U_{p2} in Figure 2.17b is dependent on both the magnitude of the peak pressure and the gradient of the pressure-time relation.
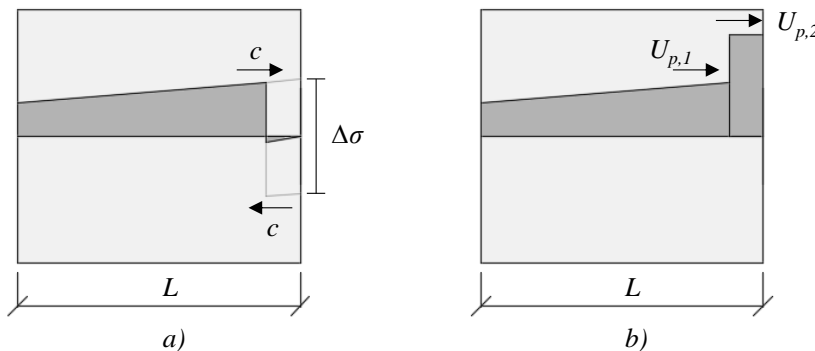
Figure 2.17   a) stress distribution and b) particle velocity in blast loaded structures.

The illustration of stress distribution and particle velocity in this section is presented without consideration to material response. To further develop the response of the structure, the material response needs to be incorporated.

2.3   Material

2.3.1   Overview

The response of a structure is highly dependent on the response of its material. The properties of concrete are very dependent on the stress state and characterized by the uniaxial stress-strain relation shown in Figure 2.18. Normal concrete shows a significant difference between tensile and compressive strength, where the tensile strength can be less than a tenth of the compressive strength, Leppänen (2004).
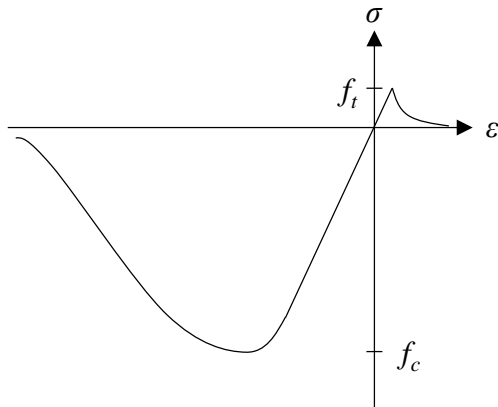
Figure 2.18   Typical stress-strain relationship of concrete under uniaxial loading, based on Leppänen (2004).

2.3.2   Fracture mechanics

Before the peak stress is reached in a specimen loaded in tension, micro-cracks start to form in local weak points in the material, see point *A* in Figure 2.19. Up to this point concrete shows a linear behaviour. As the load increases, the micro-cracks begin to connect and deformations localize in weak sections. This plastic response continues until the maximum load is reached, see point *B* ($\sigma = f_t$), after which the deformations increase with decreasing stress within the fraction zone, see point *C*, Plos (1996).
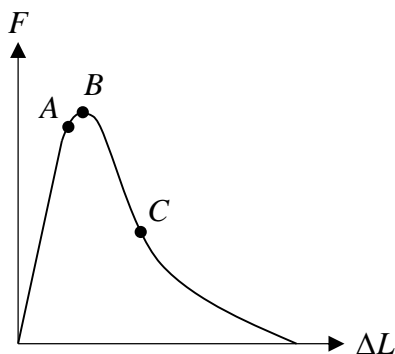
Figure 2.19   Force-elongation graph for tensile test of concrete specimen.

A measured stress-displacement relation for a concrete specimen can be recalculated to a stress-strain relation by dividing the elongation with the specimen length. However, it is not possible to directly translate the load-displacement relation to a stress-strain relation when there is a localization of the deformations due to cracking, since different specimen lengths would give different stress-strain relations, Plos (1996). To solve this, the material properties needs to be divided into an elastic stress-strain relation for the material behaviour that occur outside the fracture zone, and a stress-crack opening relation representing the additional deformations that occur within the fracture zone, see Figure 2.20. The stresses transferred within the fracture zone now depends on the crack opening *w*, and the stress is defined as $\sigma = f(w)$, where *f(w)* describes the softening behaviour of the concrete.
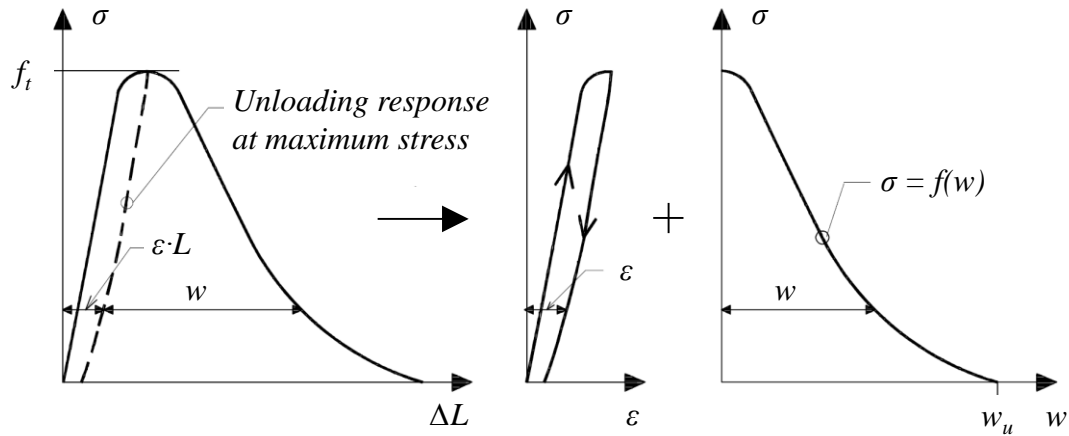
Figure 2.20   Stress-displacement relation divided into a general stress-strain relation and a stress-displacement relation representing additional localized deformations, Plos (1996).

The most characteristic parameter in fracture mechanics is the fracture energy, G_f, Plos (1996). This is the energy dissipated by fracture per unit area of the crack plane, Bažant (2002) and can be represented by the area under the stress-crack opening curve in the post-peak behaviour of the concrete, see Figure 2.21.
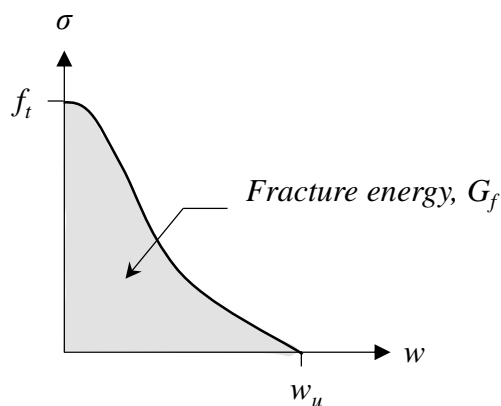
Figure 2.21   Illustration of fracture energy in the stress-crack opening relation.

2.3.3   Constitutive models for concrete in tension

When analysing the behaviour of a structure subjected to dynamic loading, the post-peak behaviour in tension is of great importance. If concrete is statically loaded in tension the stress will decrease with increasing deformation after the peak stress is reached. This tension softening develops more or less exponentially, but can according to Gylltoft (1983) be simplified as a bi-linear or linear relation. A linear tension softening for plain concrete subjected to monotonically increasing load in tension is shown in Figure 2.22. However, since the studied phenomenon in this thesis occurs under non-monotonic loads described in Section 2.2.4, the unloading of the structure becomes of significance.
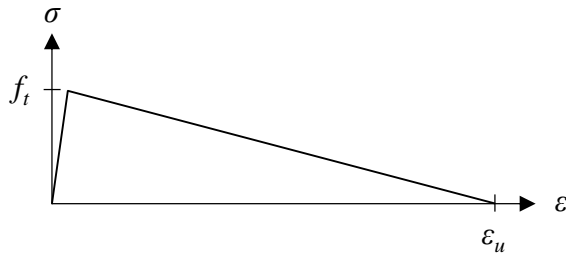
Figure 2.22   Linear strain softening of monotonically loaded concrete.

In Reinhardt (1984), several test of concrete subjected to non-monotonic tension was studied and numerical expressions for the post-peak behaviour and unloading and reloading were derived. Concrete specimens were subjected to cyclic tension with different lower stress values, see Figure 2.23. In Figure 2.23a, the lower stress is considered to be 5% of the tensile strength and in the second test it is considered to be equal to the tensile strength but in compression. Furthermore, a present model to approximate the loading and unloading behaviour is plotted in the same figure. In the present model the damage is considered in equation (2.10) as the damage parameter δ^+ that varies from 0 (material without deterioration) and 1 (completely damaged material), Sima *et al* (2008), changing the effective elastic modulus *E*.

$$E = (1 - \delta^+) \cdot E_0 \tag{2.10}$$
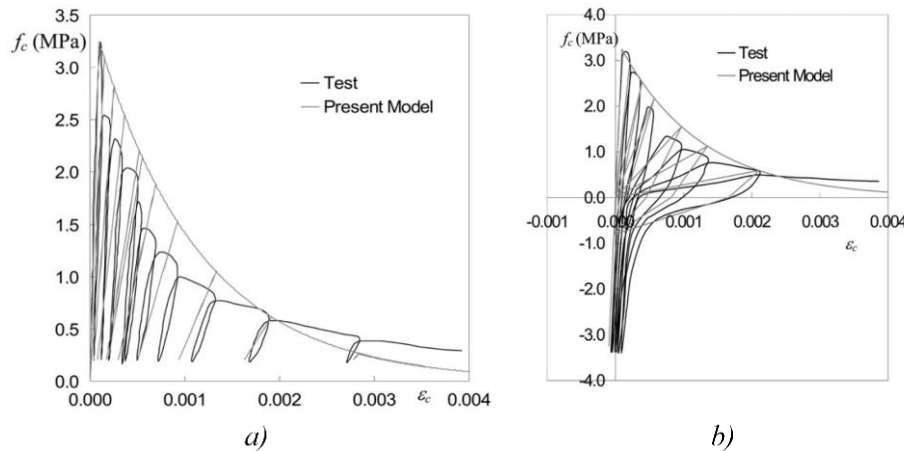
Figure 2.23   a) Cyclic tension test and b) cyclic tension test with high incursions in compression, Sima et al. (2008).

When simplifying to a linear strain softening, three constitutive laws will mainly be considered in this thesis; a plasticity model, a damage model and a combined damage-plasticity model. The main differences between the models are that the unloading response in the plasticity model is based on the original stiffness, while in the damage and damage-plasticity model, the stiffness will be reduced, illustrated in Figure 2.24.
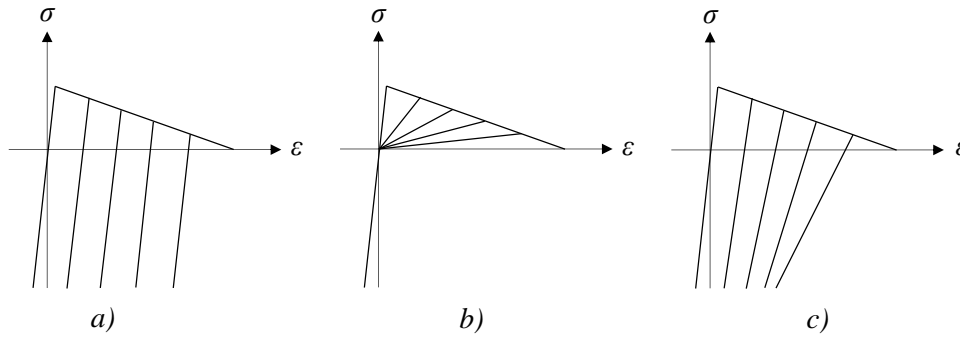
Figure 2.24   Stress-strain relation for non-monotonic loading of concrete for a) plasticity model, b) damage model and c) damage-plasticity model.

2.3.4   Strain rate

2.3.4.1   Overview

Strain rate can be defined as how fast an imposed strain develops within a material. This measurement is a material specific parameter that can distinguish between long and short time intervals for the specific material. Johansson (2000) illustrates a generalized range of different strain rates and the corresponding load application, see Figure 2.25. This thesis focuses mainly on hard impact and blast loading, which will correspond to strain rates in the range of 10^0-10^3 [s^{-1}]. These strain rates can be compared with 10^{-5} [s^{-1}], which corresponds to static loading. Thus, the strain rate for blast loading can be 10^8 times greater, which may be important to consider for blast loaded structures.
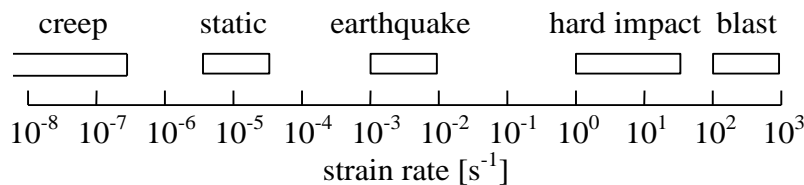
Figure 2.25   Approximate strain rates for different load cases, Johansson (2000).

Concrete is a material that is strain rate dependent, giving changes in material properties for different strain rates, Johansson (2000). To illustrate this change in mechanical properties at high strain rates, it is common to use the concept of a dynamic increase factor (DIF). This factor describes the relation between the dynamic strength and the static strength of the material, see equation (2.11) and is determined experimentally.

$$DIF = \frac{F_{dyn}}{F_{sta}} \tag{2.11}$$

Further, Figure 2.26 show test results of how the concrete compressive and tensile strength are influenced at different strain rates.
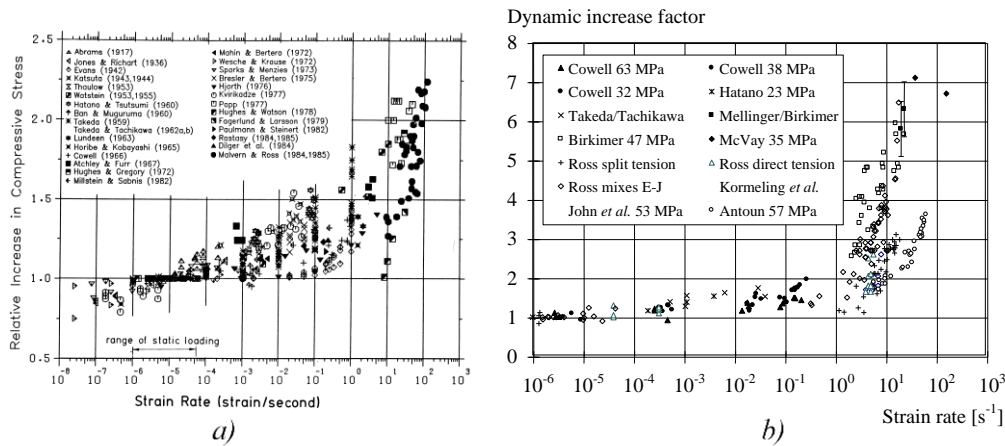
Figure 2.26   Relative increase in concrete strength for a) compressive strength and b) tensile strength at different strain rates. Based on Bischoff and Perry (1991), and Malvar and Ross (1998).

For strain rates corresponding to blast loading, the dynamic increase factor is different whether the compressive or tensile strength is considered, Johansson (2000). Figure 2.26a shows that the compressive strength can be increased up to two times when considering strain rate effects, while the corresponding factor for tensile strength is approximately 6-7 according to Figure 2.26b.

Bischoff and Perry (1991) suggest that the large scatter in dynamic increase factor indicates the difficulties related to high strain rate effects. High dynamic testing is in general much more complicated to carry out compared to corresponding static tests. However, the large scatter in dynamic increase factor is considered to be partially explained by parameters such as concrete strength, specimen dimension, moisture content and test method. This is why test results in Figure 2.26 are not necessarily comparable fully with each other, since the stated parameters can vary between the different tests.

2.3.4.2   Strain rate influence on concrete strength found in literature

In order to make Figure 2.26 applicable in reality, several researchers have proposed expressions that more accurately relate strain rate to concrete strength, Johansson (2000). For compressive strength, expressions have been established by Seabold (1970), Dilger *et al.* (1984), Soroushian *et al.* (1986) and the CEB-FIP Model Code, CEB (1993) and are illustrated in Figure 2.27a. For tensile strength, CEB (1993), Ross *et al.* (1996) and Malvar and Ross (1998) have proposed expressions in accordance with Figure 2.27b.
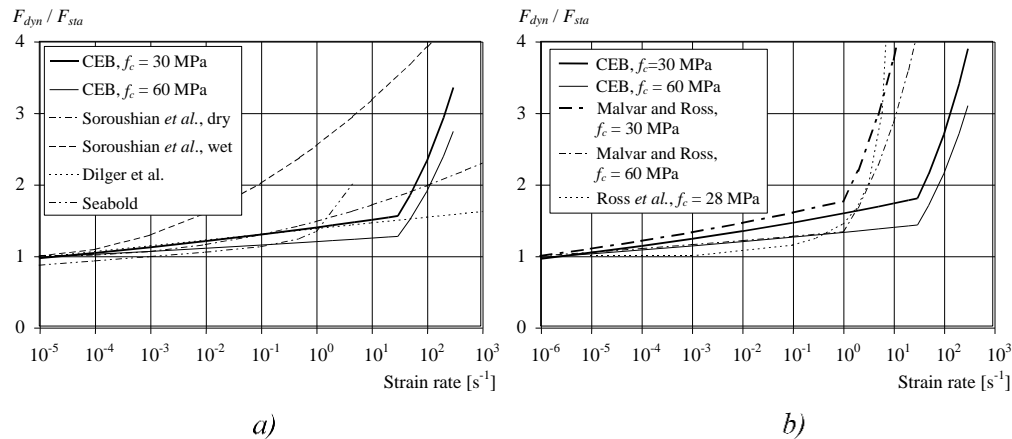
Figure 2.27   Concrete strength related to strain rate found in literature, a) compressive strength and b) tensile strength. Johansson (2000).

What can be concluded from Figure 2.27 is that the different expressions vary noticeable between the different researchers. However, these relations are not necessarily comparable to each other since in some cases they depend on different properties. For example, Soroushian *et al.* (1986) distinguish between dry and wet concrete which gives different dynamic increase factor, see Figure 2.27a. Furthermore, the influence of concrete compressive strength is also included in several expressions, such as Ross *et al.* (1996) who even included fracture toughness, see Figure 2.27b.

According to Johansson (2000), the most accepted relation between strain rate and dynamic increase factor for concrete in tension is the one presented by Malvar and Ross (1998). For this relation, the DIF is related to the compressive strength of the concrete, see Figure 2.27b.

2.3.4.3   Possible explanations for increased strength

Even though the different expressions for the dynamic increase factor vary considerably between different researchers, seen in Figure 2.26 and Figure 2.27, they all conclude that the concrete strength increases with increasing strain rate. For both compressive and tensile loading, a transition zone can be identified where the strain rate dependency changes drastically, Magnusson (2007). This change is due to a change in mechanism causing strain rate effects on the concrete strength, Johansson (2000). For strain rates lower than the transition zone, Johansson suggests that the DIF depends on viscous effects. However, for strain rates higher than the transition zone the DIF is dominated by structural effects. This is schematically illustrated in Figure 2.28.
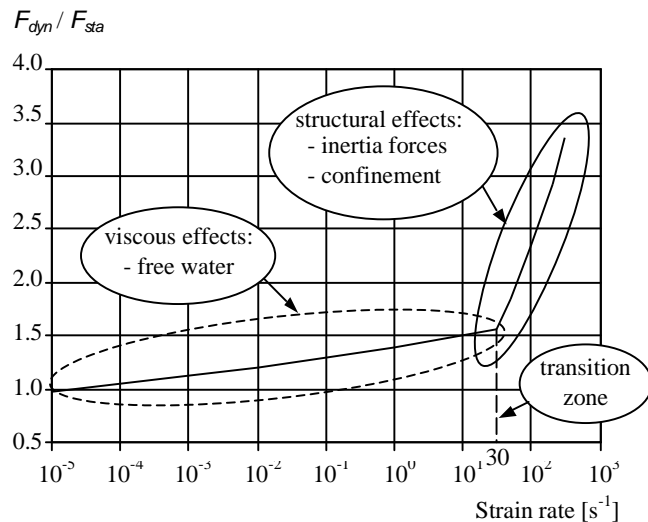
Figure 2.28   Illustration of transition zone where the strain rate effects are dominated by either viscous effects or structural effects. From Johansson (2000).

What can be concluded by Figure 2.28 is that the strength enhancement due to viscous effects is relatively small compared to the structural effects, Johansson (2000). Viscous effects relate to free water in the micro-pores of the concrete. Magnusson (2007) describes that the free water, in a specimen loaded in compression, will build up an internal pressure which can help to resist the compressive load. Furthermore, Magnusson suggests that the increase in tensile strength can be considered to act in a similar way as a thin film of water trapped between two plates moving apart, which will create resisting forces.

At higher strain rates the mechanism of strength enhancement changes from viscous effects to structural effects. These structural effects relate mostly to inertia effects, such as inertia forces and lateral inertia confinement, Johansson (2000). These effects will be studied more in detail in Section 2.4.5.

2.4   Fracture due to blast loading

2.4.1   Overview

The two different fracture phenomena evaluated in this section are cratering and spalling. Cratering is a form of damage that occurs on the same side of the structure as the explosion and is a result of the high pressure crushing the concrete. Spalling in concrete is defined as an ejection of material fragments at the opposite side from which the structure was loaded, see Figure 2.29. If the loading is highly intense, spall fragments can eject with a velocity high enough to damage persons and equipment, McVay (1988). Since material is removed from the structural element when spalling and cratering occurs, the structure is weakened and can lead to a local or even global collapse, Johansson (2013a). Breaching is another phenomenon that occurs when the blast load is of such magnitude that the cratering and spalling depths reach each other.
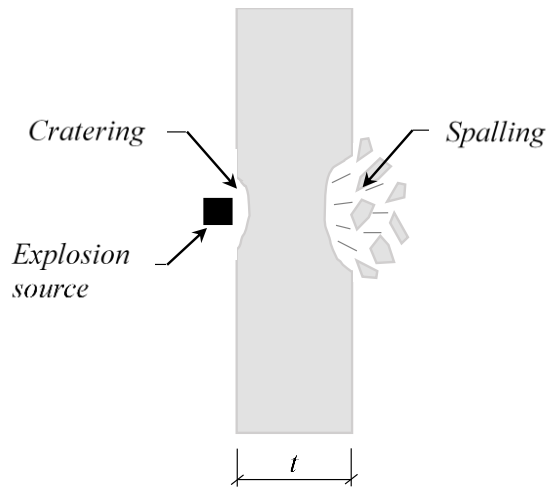
Figure 2.29   Illustration of cratering and spalling in a structure subjected to a contact detonation.

In accordance with Figure 2.15 in Section 2.2.4, the reason why spalling occurs is due to the appearance of tensile stresses in the structure when the compressive shock wave reflects at the free edge, Johansson (2013a). However, there is one conventional way of evaluating spalling and one recently developed hypothesis by PhD student Jonas Ekström at Chalmers University of Technology. These will both be described in Section 2.4.2 and 2.4.3. The assumption in both these sections is that the shock wave from a nearby explosion is considered to have a flat profile and a linear pressure-time relation, in accordance with Figure 2.13.

2.4.2   Conventional spalling evaluation

The conventional way of evaluating spalling in concrete, considered by several researchers such as McVay (1988), is to assume that spalling occurs when the tensile stress at the rear side of the structure reaches the tensile strength. This can also be referred to as fully brittle spalling. The illustration in Figure 2.30 is based on a linear pressure-time decrease with long load duration. When the resulting tensile stress from the reflected shock wave reaches the tensile strength of the concrete, a crack will fully develop and eject a portion of the structural element with velocity v_1, as illustrated in Figure 2.30b.
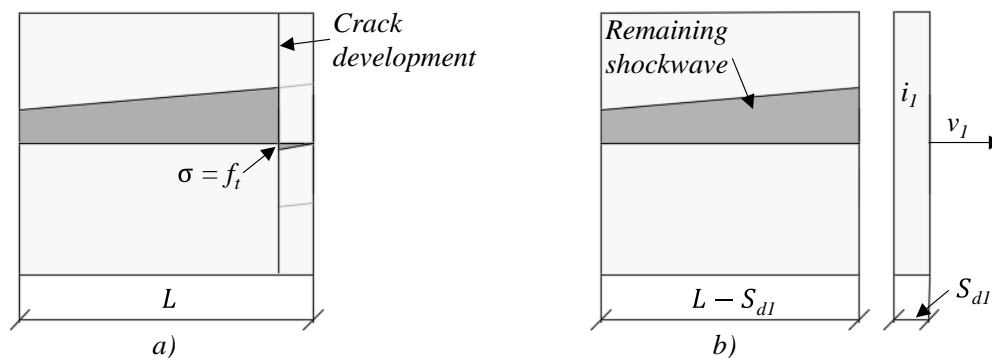
Figure 2.30   Illustration of conventional spalling evaluation.

The remaining shock wave after the first ejection, see Figure 2.30b, will reflect once again on the developed free edge and can cause further spalling in accordance with

Figure 2.31a. The new crack will eject another portion of the element with velocity v_2, see Figure 2.31b.
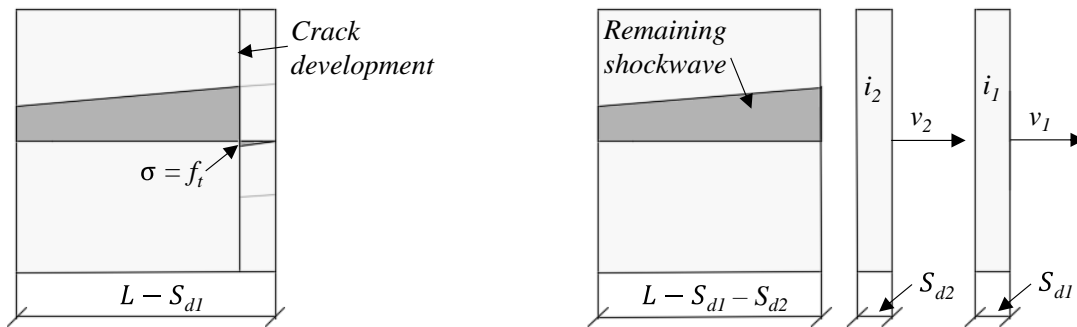
Figure 2.31   Illustration how the remaining shock wave generates further spalling.

The remaining shock wave will once again reflect on the developed free edge, which is the ongoing principle until the shock wave no longer has high enough intensity to cause spalling, McVay (1988).

This process could also be illustrated using the pressure-time relation of the blast loaded structure, see Figure 2.32. The velocities v_1 and v_2 are generated by impulses i_1 and i_2 respectively and can be regarded as that the impulse is "trapped" between the developed crack and the free edge, Johansson (2013). Due to the linearity of the pressure-time relation, the time duration of both impulses t_{dur} will be the same. Thus, the first impulse i_1 will be greater than i_2 which consequently results in $v_1 > v_2$.
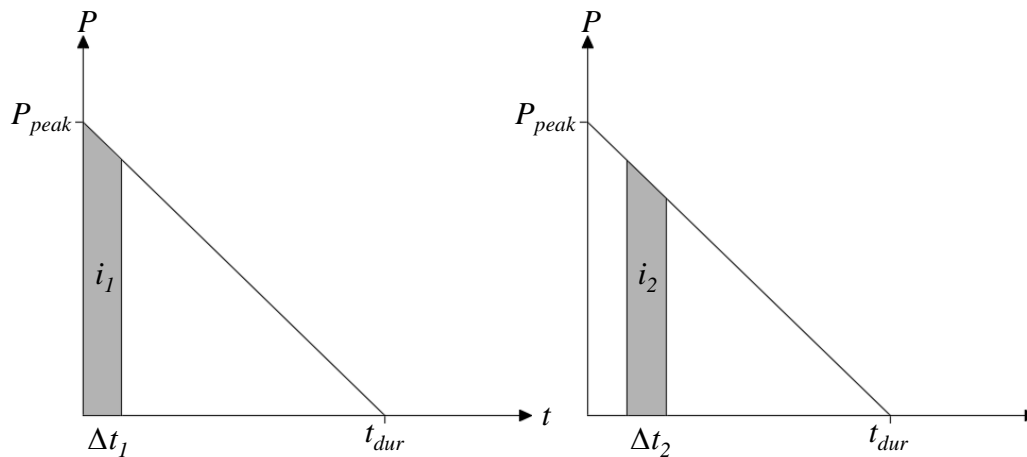
Figure 2.32   Schematic view of the spalling process a) impulse given to firstly ejected portion and b) impulse given to secondly ejected portion, based on Johansson (2013).

McVay (1988) have derived several expressions for how the spalling depth depends on the shape of the pressure-time relation. For linearly decreasing shape, the spall depth is determined as

$$S_{d,i} = \frac{c \cdot t_{dur} \cdot f_t}{2 \cdot P_{Peak}}$$

(2.12)

where c is the velocity of the shock wave in accordance with equation (2.9), t_{dur} is the duration of the impulse, f_t is the tensile strength of the concrete and P_{peak} is the peak pressure. Based on equation (2.12) it is clear that the spall depth S_{d1} and S_{d2} from Figure 2.31 will be the same. However, this is only true when the pressure-time relation decreases linearly.

To conclude this section, it is clear that the spalling process is highly dependent on several parameters. Both the thickness of the studied element and the properties of the pressure-time relation will decide how the spalling process develops.

2.4.3 Hypothesis on spalling

The principle described in Section 2.4.2 assumes that a fully developed spalling crack appears instantaneously as the tensile stress reach the tensile capacity. However, as described in Section 2.3.2, a fully developed crack is not reached until the fracture energy has dissipated. This is the reason why Ekström (2016) claims that the conventional method for evaluating spalling is inaccurate. Ekström reason that the most obvious limitation of the fully brittle crack spalling approach is that the strain softening of concrete in tension becomes irrelevant since the structure will eject material as soon as the tensile strength is reached. This means that the strain reaches infinity within a stress-time singularity.

If the strain where to reach infinity within a time singularity, the applied energy in the cracking plane must be infinite. However, the energy within a pressure wave is finite, which means that the spalling process is unlikely to proceed in accordance with Section 2.4.2. This is why Ekström reason that a crack can only be initiated, and not fully developed, within this time singularity. Figure 2.33 illustrates a principle view of the time-singularity when the stress reaches the tensile strength.
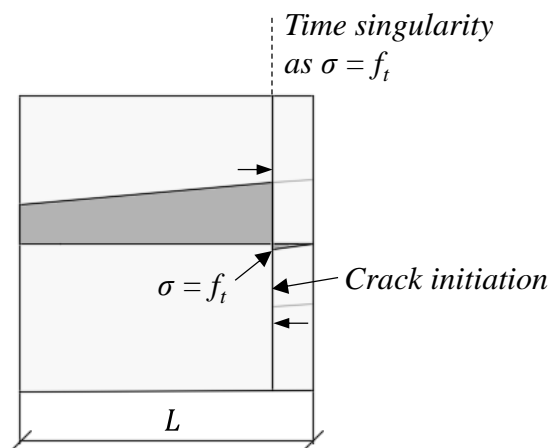
Figure 2.33   Crack initiation within the defined time singularity when $\sigma = f_t$.

By the reasoning that the crack only can be initiated and not fully developed during the defined time singularity, the crack must develop some time after the stress wave front have passed the material point in the cracking plane, Ekström (2016). This is why Ekström claims that a fully developed spalling crack appears after cyclic development of inelastic strains, as the shock wave propagates in alternating tension and compression.

By applying this concept, it is not obvious where the spalling crack will occur. It will be dependent on the post peak behavior of concrete in tension, as well as the material response during cyclic loading/unloading. For this reason it is complicated to predict and illustrate a schematic view of how the stress profile will look at any certain time after crack initiation, which was illustrated for the brittle crack spalling approach in Figure 2.31.

2.4.4 Empirical estimations

2.4.4.1 Overview

The response of blast loaded structures is a complex issue to evaluate. The fact that blast loading is mostly related to military applications makes it difficult to find extensive information in the literature. However, experiments on the subject have been made and based on these, empirical estimations have been developed. The main advantage of empirical methods is that their simplicity makes it easy to get a rough estimation of the effects that can be expected, Johansson (2013b). On the other hand, the downside of empirical methods is the fact that the estimations are only based on the conditions given by the specific case.

2.4.4.2 FKR 2011

In the report FKR 2011, Fortifikationsverket (2011), recommendations of the required minimum thickness t of a concrete element is given to meet different levels of acceptable damage from a contact detonation. These different levels of acceptable damage are:

   a) No spalling occurs
   b) Spalling occurs
   c) Breaching occurs

A schematic picture of the damage magnitude estimated for case b), when spalling is expected is shown in Figure 2.34.
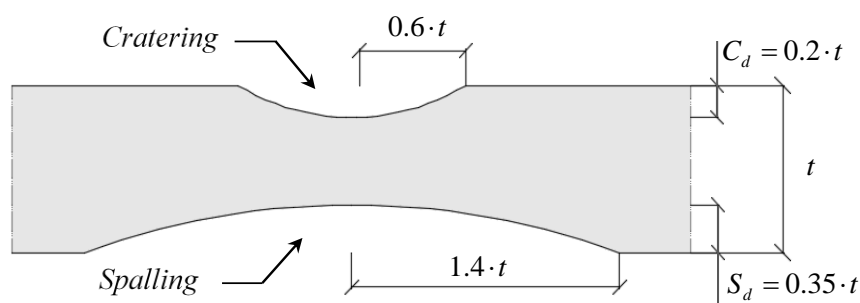
Figure 2.34   Schematic picture of the estimated damage on a structure subjected to a contact detonation for case b), spalling is expected. Based on Fortifikationsverket (2011).

The required thickness t for the case when no spalling is expected is described as

$$t_{a,FKR} = 0.78 \cdot W^{1/3} \cdot r_K \tag{2.13}$$

when spalling is expected as

$$t_{b,FKR} = 0.31 \cdot W^{1/3} \cdot r_K \tag{2.14}$$

and when breaching is expected as

$$t_{c,FKR} = 0.18 \cdot W^{1/3} \cdot r_K \tag{2.15}$$

where W is the equivalent amount of TNT of the load and r_K is a reduction coefficient that takes the strength of the concrete into account. Equations (2.13) to (2.15) are only viable if the characteristic compressive strength of the concrete $f_{cc,cube} \geq 40$ MPa. If the compressive strength exceeds 40 MPa the thickness can be reduced with r_K, which can be described with the expression

$$r_K = \sqrt{\frac{40}{f_{cc,cube}}} \qquad (f_{cc,cube} \leq 48 \text{ MPa}) \tag{2.16}$$

As can be seen in Figure 2.34, the crater and spalling depth for acceptable damage level b) is

$$C_d = 0.2 \cdot t_{b,FKR} \tag{2.17}$$

$$S_d = 0.35 \cdot t_{b,FKR} \tag{2.18}$$

For acceptable damage level A and C no such expressions are given, but according to Johansson (2013b) it can be assumed that the crater depth is the same, independent of the concrete thickness. In agreement with that assumption, equations (2.13) to (2.18) can be combined to estimate the crater and spalling depths for these cases as well, resulting in

$$t_{b,FKR} = \frac{0.31}{0.78} \cdot t_{a,FKR} = 0.40 \cdot t_{a,FKR} \tag{2.19}$$

$$C_d = 0.2 \cdot 0.4 \cdot t_{a,FKR} = 0.08 \cdot t_{a,FKR} \tag{2.20}$$

$$C_d = 0.2 \cdot \frac{0.31}{0.18} \cdot t_{c,FKR} = 0.34 \cdot t_{c,FKR} \tag{2.21}$$

It can be observed in equation (2.21) that the crater depth is about 1/3 of the thickness when breaching occurs. The fact that the estimated crater depth is smaller than the spalling depth is in accordance with what has been shown in experimental tests by McVay (1988), Wang *et al*. (2008) and Yamaguchi *et al*. (2009).

2.4.4.3 Unified Facilities Criteria (UFC)

In the Unified Facilities Criteria (UFC), found in Acosta (2011), similar criteria as in Section 2.4.4.2 are presented but with the exception that the distance to the load can be taken into account. Here, two different levels of damage are given:

b) Spalling occurs
c) Breaching occurs

The required thickness $t_{b,UFC}$ can be evaluated with the expression

$$t_{b,UFC} \geq \frac{r}{-0.02511 + 0.01004 \cdot \psi^{2.5} + 0.13616 \cdot \psi^{0.5}} \qquad (2.22)$$

and required thickness $t_{c,UFC}$ as

$$t_{c,UFC} \geq \frac{r}{0.028205 + 0144308 \cdot \psi + 0.049265 \cdot \psi^{2}} \qquad (2.23)$$

where r is the distance from the element face to centre of charge in [ft]. The factor ψ is a spalling parameter that can be expressed as

$$\psi = r^{0.926} \cdot f_c^{0.266} \cdot W^{-0.353} \quad (0.5 \leq \psi \leq 14) \qquad (2.24)$$

where f_c is the concrete compressive strength in [psi] and W is the charge weight expressed in [lb]. The expression in equation (2.24) is in imperial units, hence the thickness t in equations (2.22) and (2.23) is returned in [ft].

2.4.4.4 Cormie *et al.*

In Cormie *et al.* (2009), a spall depth of half the thickness of the element is the approximate threshold at which breaching occurs. However, shear and flexural reinforcement can limit the disengagement through confinement of spalling fragments. The thickness of an element required to prevent spalling and breaching from a spherical charge at distance r is expressed as

$$t_{b,Cormie} \geq 0.07 \left(\frac{r}{W^{1/3}} \right)^{-0.62} \cdot W^{1/3}$$

and

$$t_{c,Cormie} \geq 0.03 \left(\frac{r}{W^{1/3}} \right)^{-0.62} \cdot W^{1/3}$$

where W is the charge weight in [kg].

2.4.5 Spalling and cratering effected by high strain rate effects

The general approach for considering strain rate effect was presented in Section 2.3.4, where it was found that the concrete strength is dependent on the strain rate. Since blast loading may correspond to very high strain rates in the range of 10^2-10^3 [s^{-1}], the compressive and tensile strength could be increased with a factor 2-3 and 6-7 respectively, see Section 2.3.4. This strength enhancement will most likely influence the response at blast loading.

The mechanism behind the rapid tensile strength growth after the transition zone can be described by a changed stress and energy distribution at the crack tips due to inertia effects, Johansson (2000). This effect could, according to Johansson, also describe some of the strength enhancements on the compressive side, since compressive failure also is governed by cracking.

Bischoff and Perry (1991) reason that the structural effect causing enhancement of the compressive strength also can be described by lateral inertia confinement. This effect can be described by comparing a statically loaded and a blast loaded elastic material. When the material is statically loaded in compression, it will expand laterally due to the effect of Poisson's ratio. However, at blast loading in compression the material will not have time to expand in such way, causing inertial restraint which results in strength enhancement.

Compressive strength enhancements, however, will not directly influence the resistance of spalling in the structure. Although it will enhance the structures resistance to cratering, which is a common damage at contact detonation. By increasing the resistance to cratering the structure is able to transfer higher compressive loads, which consequently leads to that the risk of spalling increases as the compressive wave reflects at the free edge. The tensile strength enhancement though, will clearly enhance the structures resistance to spalling since the structures capacity to transfer tensile stresses increase.

In conclusion, high strain rate effects can, and most likely will affect the structural response in both compression and tension. This phenomenon though, will not be treated in the numerical analysis in this thesis.

3 Experimental methods to evaluate spalling

3.1 Overview

The material properties of concrete under high strain rates were discussed in Section 2.3.4, where it was found that the properties could change drastically at strain rates corresponding to blast loading. In order to evaluate phenomenon such as spalling accurately, the model of concrete at static loading has to be extended by dynamic material properties, Schuler *et al.* (2005). Several experiments have been performed to study this effect.

To study the effect of high strain rate loading, a common experimental set up is to use the Split Hopkinson Pressure Bar (SHPB), Schuler *et al.* (2005). This bar can be used in different configurations to study both compressive and tensile loading, and based on the results determine material properties at the given load. Figure 3.1 shows a simplified illustration of a SHPB, used to determine compressive properties under impact loading. The concept of such a bar is to not impact the specimen directly, but rather impact it via an elastic rod which is called incident bar. The elastic rod on the other side of the specimen is called transmission bar, Chen and Song (2011). Both the incident bar and the transmission bar are used to record the conditions caused by the external impact.
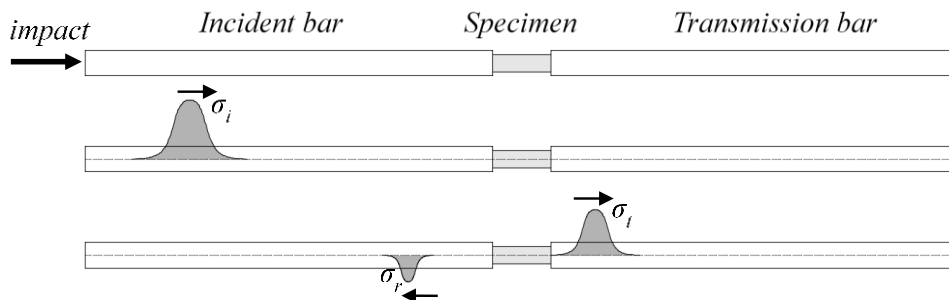
Figure 3.1   Illustration of a Split Hopkinson Pressure Bar design, based on Chen and Song (2011)

The external impact will cause a stress wave σ_i to propagate in the incident bar, which will reflect and transmit at the interface of the specimen to become σ_r and σ_t, respectively, see Figure 3.1. Thus, the impact event for the specimen is controllable and quantitative which is important in order to accurately determine material properties.

By adjusting the specimen connection in Figure 3.1 the setup can be used for tension tests as well, Wu *et al.* (2005). This is achieved by adjusting the specimen connection to extend within the incident and transmission bar, see Figure 3.2. In such way, it is possible to utilize the reflected stress wave in the incident bar to apply tensile stress to the specimen. Wu *et al.* refers to this experimental setup as a Split Hopkinson Tension Bar (SHTB).

Figure 3.2   Illustration of a Split Hopkinson Tension Bar design, based on Wu et al. (2005)

Schuler *et al.* (2005) reason that this type of direct tension tests is suitable for strain rates in the range of 10^{-1} to 10^1 [1/s]. Higher strain rates, e.g. blast loading, can be achieved by spall experiments, which is a further development of the SHPB. This section will study two different spalling experiments conducted by Schuler *et al.* (2005) and Wu *et al.* (2005).

3.2   Schuler *et al.*

To investigate the tensile behavior under high strain rates, Schuler *et al.* (2005) conducts experiments with a modified SHPB. The setup consists of a projectile, incident bar and a concrete specimen glued to the surface of the incident bar, see Figure 3.3. The modified SHPB lacks a transmission bar, instead it uses an acceleration gauge to determine the particle velocity at the right edge of the specimen.
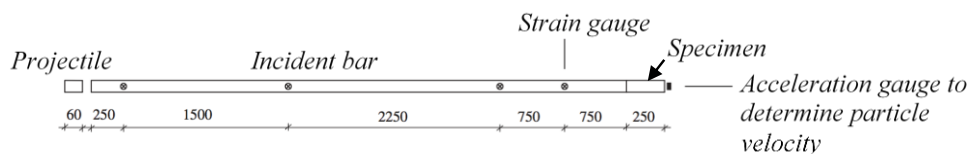
Figure 3.3   Experimental setup by Schuler et al. (2005), modified SHPB with strain gauge in the incident bar and acceleration gauge at the free edge of the specimen.

The projectile generates a stress wave in the incident bar, which reflects and transmits at the surface between the incident bar and the specimen. The transmitted stress wave in the specimen will, as described in Section 2.2.4, reflect at the free edge and become a tensile wave that interacts with the compression wave. The stress propagation in the modified SHPB is summarized in Figure 3.4.
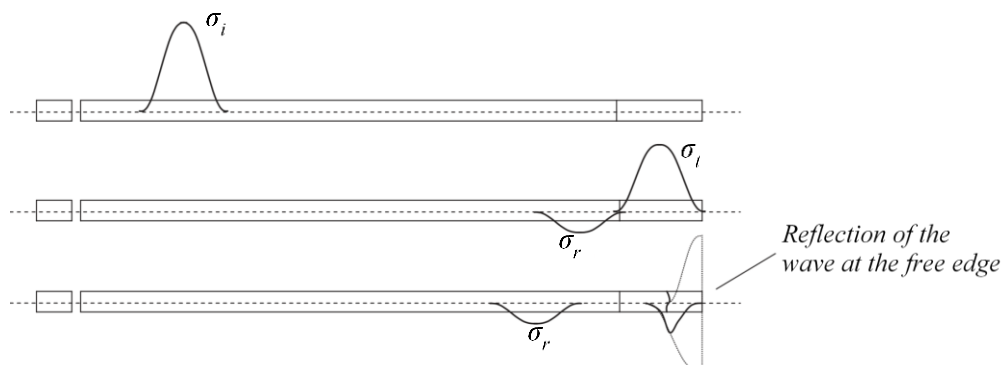
Figure 3.4   Stress propagation in the modified SHPB. Reflection at the free edge creates tensile stresses which can result in spalling, Schuler et al. (2005).

By using the acceleration gauge at the right end of the specimen, Schuler can determine the velocity of the free surface. The strain gauge at the end of the incident bar is used to measure the applied strain to the specimen. Figure 3.5 shows the particle velocity at the end of the specimen, as well as the strain at the beginning of the specimen, i.e. at the end of the incident bar.
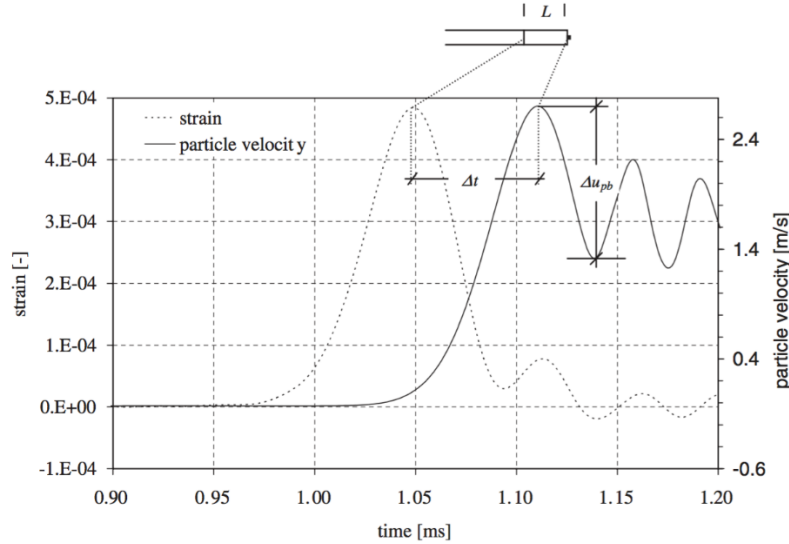
Figure 3.5   *Strain at the end of the incident bar (beginning of the specimen) and particle velocity at the end of the specimen, Schuler et al. (2005).*

Based on the data in Figure 3.5 the dynamic Young's modulus can be determined as

$$c_0 = \frac{L}{\Delta t} \Rightarrow E_{dyn} = \rho \cdot c_0^2 \qquad (3.1)$$

where L is the length of the specimen, Δt is the time it takes for the stress wave to propagate through the specimen, ρ is the density and c_0 is the pressure wave velocity. Further, Schuler determines the dynamic tensile strength based on the measurements from the velocity gauge at the free end of the specimen. By using the pullback velocity, Δu_{pb} in Figure 3.5, the dynamic tensile strength is determined as

$$f_{dyn} = \frac{1}{2} \cdot \rho \cdot c_0 \cdot \Delta u_{pb} \qquad (3.2)$$

Another parameter evaluated is the dynamic fracture energy. However, Schuler claims that in spall experiments it is not possible to measure stress over crack opening as it can be done in static tension tests. For this reason, the dynamic fracture energy is calculated based on the reduction in velocities for the ejected fragments. By considering the time t_1, when crack initiation starts, and t_2 when the crack is fully developed, the fracture energy corresponds to the dissipated energy in this time interval.

The principle of evaluating the dynamic Young's modulus, tensile strength and fracture energy is conducted for several different specimens with different properties. This thesis, though, will only briefly present results on one of them to illustrate the gained knowledge from this experiment. The concrete specimen used in the experiments has quasi static properties in accordance with Table 3.1.

Table 3.1 *Quasi static material properties for tested specimen, based on Schuler et al. (2005).*

E_{qs} [MPa]	$f_{t.qs}$ [MPa]	$G_{f.qs}$ [N/m]
38.9	3.24	125.0

The test results of dynamic material properties are presented, for one specific case, in Table 3.2.

Table 3.2 *Measured material properties for impact loading, based on Schuler et al. (2005).*

E_{dyn} [MPa]	$f_{t,dyn}$ [MPa]	$G_{f.dyn}$ [N/m]	$\dot{\varepsilon}$ [1/s]
38.6	13.2	175.3	37.1

The conclusion of Table 3.1 and Table 3.2 is that the material properties change drastically at higher strain rates. However, the dynamic Young's modulus does not deviate from the quasi-static properties, why Schuler claims that this material property is more or less strain rate independent. Further, by comparing the dynamic tensile strength with the quasi static tensile strength the dynamic increase factor corresponds to $DIF_f = 4.1$, which agrees well with Section 2.3.4.

Another important observation in the experiment is how the fracture energy is highly dependent on the strain rate. In the case described by Table 3.1 and Table 3.2, the dynamic increase factor corresponds to $DIF_{Gf} = 1.4$ for the fracture energy.

3.3 Wu *et al.*

When testing materials with high dynamic tensile strength and high ductility, the results of a Split Hopkinson Tension Bar (SHTB) described in Section 3.1, are reliable. However, for brittle material such as concrete the results from a SHTB may present errors that cannot be neglected. The errors are mainly governed by three causes;

a) The low dynamic tensile strength of concrete requires the experimental setup to be highly rigid.
b) The difficulty of data processing and repeatability of the experiment due to the brittle nature of concrete.
c) The difficulties with ensuring a sufficiently good connection between the concrete test specimen and the incident bar.

In Wu *et al*. (2005), the dynamic tensile strength of concrete is investigated through a spalling experiment using modified setup of the Hopkinson pressure bar, see Figure 3.6, that overcomes the inherent disadvantages of the original SHTB test. FE simulations are conducted in order to support the dynamic tensile experiments.
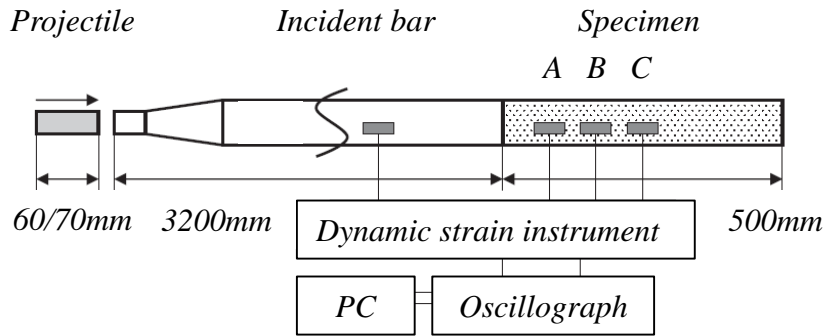
Figure 3.6   Setup for dynamic tensile test, Wu et al. (2005).

The experimental setup consists of an incident pressure bar pasted with a strain gauge and a 500 mm cylindrical test specimen with a diameter of 74 mm. A projectile is launched and strikes the incident bar, which transmits the compressive wave into the test specimen. Spalling is caused by the tension wave reflected at the free end of the specimen. The striking speed of the projectile is ensured not to cause any compressive damage as the compressive stress wave propagates through the specimen.

Since concrete is a viscoelastic material a wave attenuation will be observed. The stress wave attenuation will be considered based on measurements of the attached strain gauges. The stress wave propagation is described using the exponent annotation rule

$$\sigma = \sigma_0 \cdot e^{-\alpha \cdot x} \tag{3.3}$$

where σ_0 represents the stress amplitude at the end of the incident bar and α is the attenuation coefficient. Therefore, the incident stress wave form at the free edge is predicted based on the attenuation rule in equation (3.3) and the measured wave shape and is illustrated in Figure 3.7.
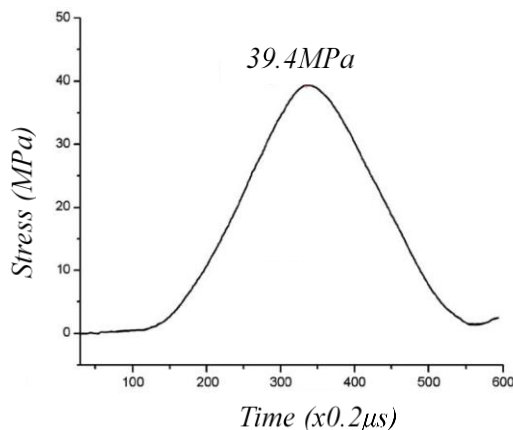
Figure 3.7   Stress wave shape for experimental data, Wu et al. (2005).

The reflected tensile stress wave from the incident compressive wave at the free edge can be predicted using one-dimensional wave analysis. Based on that theory the tensile stress distribution over the length of the specimen can be obtained as a function of time, giving the position of the generated stress peak. Furthermore, the

fracture stress in tension and strain rate can be determined by such procedure. The strain rate is determined from the evolution of stress in the tensile fracture location as

$$\dot{\varepsilon}_{spalling} = \frac{1}{E}\left(\frac{\partial \sigma_t}{\partial t}\right)_{cracklocaion}$$

(3.4)

where the considered time interval is between the time when tensile stress occurs and the time when the crack takes place. The variation of dynamic tensile strength and the logarithm of strain rate are presented in Figure 3.8.
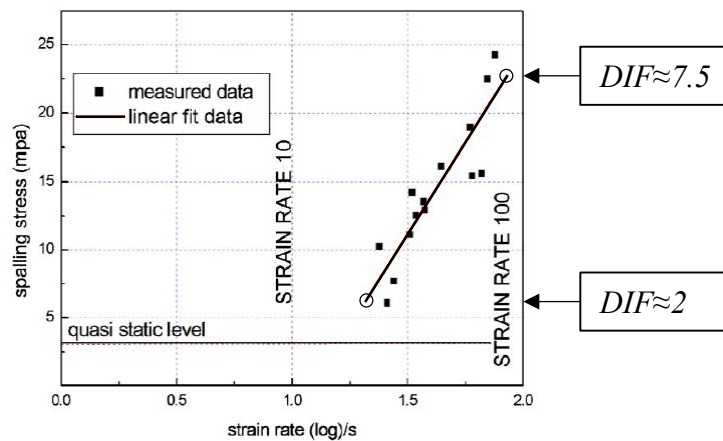
Figure 3.8   Spalling stress as a function of strain rate, Wu et al. (2005).

It can be concluded that the obtained relation of dynamic tensile strength and strain rate indicates that concrete has high strain rate sensitivity. The dynamic increase factor for the tensile strength is as high as 7.5, which is in accordance with conventional theory in Section 2.3.4.

4 Numerical analysis

4.1 Overview

The response of structures exposed to explosions can be somewhat complicated to evaluate and are in most cases determined based on experiments, as described in Chapter 3. Since the conventional method of how to evaluate spalling in concrete, presented by McVay (1988), does not consider material ductility, Ekström (2016) rejects this hypothesis as described in Section 2.4.3. In order to show that the structural behaviour supports his hypothesis, Ekström developed a numerical model which can simulate the spalling phenomenon for structures subjected to blast loading.

This chapter will include an overview of the model, and further analyses, in addition to the results presented by Ekström, are performed as a part of a parametric study. Further, this chapter will present results of how the structural response, with regard to spalling, will be influenced by using non-linear strain softening and non-linear pressure time relation.

4.2 Model

Wave propagation and spalling in concrete can be simulated using a structural element of plain concrete that is subjected to blast loading. This structural element is studied using a one-dimensional (1D) finite element model. Each element is modelled using bar elements, with a certain stiffness and mass. The assembled model is subjected to a load corresponding to an explosion at a certain distance from the structure, which means that a flat pressure profile is assumed in accordance with Section 2.1.3. A principle figure of the structural element and FE-model is illustrated in Figure 4.1.
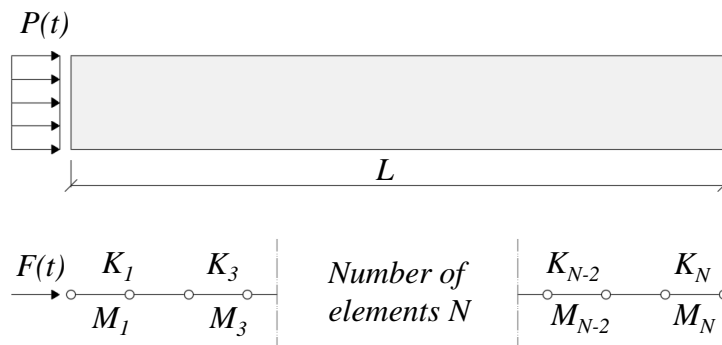

Figure 4.1   Structural concrete element and finite element approximation using a one dimensional model.

Since the model consists of bar elements, stiffness matrix *K* and mass matrix *M* of each element is obtained using equation (4.1) and (4.2) respectively

$$K_i = \frac{A_i \cdot E_i}{L_i} \cdot \begin{pmatrix} 1 & -1 \\ -1 & 1 \end{pmatrix} \tag{4.1}$$

$$M_i = \frac{\rho_i \cdot A_i \cdot L_i}{6} \cdot \begin{pmatrix} 2 & 1 \\ 1 & 2 \end{pmatrix} \qquad (4.2)$$

where A_i is the area, E_i is the Young's modulus, L_i is the element length and ρ_i is the density. The load acting on the structure, i.e. $P(t)$ in Figure 4.1, is based on the magnitude of the explosion and the distance between the explosion and the structure. In analogy with Figure 2.3 in Section 2.1.1, the shape of the pressure time relation can be somewhat complex. However, by only including the overpressure and the duration of the load, the pressure-time relation can be determined using equation (4.3)

$$P(t) = P_{peak} \cdot \left(1 - \frac{t}{t_{dur}}\right)^n \quad n = 0..1..2... \qquad (4.3)$$

The exponent n governs the shape of the pressure-time relation, hence for exponent $n \geq 2$ (where $n \in 0..1..2..$) the pressure-time gradient becomes non-linear. Since the analysis only includes the positive phase of the pressure-time relation, equation (4.3) is only valid for $t \leq t_{dur}$. Principle pressure-time relations are illustrated in Figure 4.2.
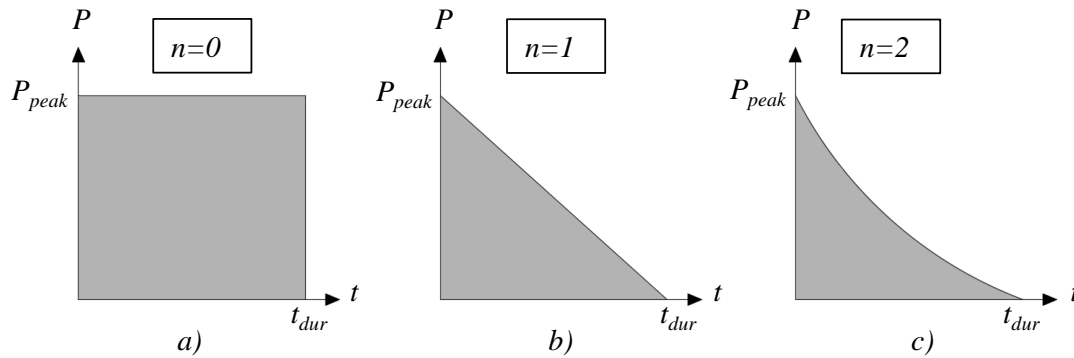
Figure 4.2   *Illustration of pressure-time relations based on equation (4.3) for a) $n = 0$, b) $n = 1$ and c) $n \geq 2$.*

Ekström (2016) only consideres the special case where $n = 1$, giving a linear pressure-time gradient seen in Figure 4.2b. Since the analysis is based on a one-dimensional finite element model, a force is applied rather than a pressure. By using a reference area A in the structure the applied force is determined using equation (4.4).

$$F(t) = A \cdot P(t) \qquad (4.4)$$

The material characteristics of concrete is approximated as a linear elastic material until the tensile capacity is reached. Hence, the non-linear behaviour of concrete compression is not considered in Ekström's analysis; i.e. plastic strains or damage propagation is not allowed to take place in compression. The characteristics of the strain softening branch is by Ektröm (2016) considered to be linear for all material models. Further, the concrete is modelled using a smeared crack approach to describe crack localisation. A crack band width, over which inelastic strains distribute, is therefore pre-defined. Ekström suggests that the crack band width is equal to three times the maximum aggregate size used in the concrete. The concept of the crack band width will be further elaborated on in Section 4.9. The overall characteristics

and input used in Ekström's analysis is summarized in Table 4.1, which will be the reference model to which other configurations will be compared to in the parametric study.

Table 4.1   Geometry, load and material parameters for reference model.

Parameter	Value	Unit
Concrete thickness, L	300	[mm]
Tensile strength, f_{ct}	2	[MPa]
Young's moduls, E	30	[GPa]
Density, ρ	2350	[kg/m^3]
Maximum aggregate size	16	[mm]
Area, A	1	[mm^2]
Fracture energy, G_f	132	[N/m]
Equivalent TNT charge	1500	[kg]
Distance to structure, r	5	[m]
Peak pressure, P_{peak}	50.74	[MPa]
Load duration, t_{dur}	1.31	[ms]
Number of elements N	100	[-]
Crack band width	48	[mm]

4.2.1   Material models

As treated in Section 2.3.3, there are different approaches to treat concrete in tension. Therefore, Ekström investigates the structural response using three different material models; a plasticity model, a damage model and a damage-plasticity model which are illustrated in Figure 4.3. For stress states below the tensile capacity in the plasticity model, see Figure 4.3a, the response remains elastic during unloading/loading based on the Young's modulus. In the damage model, see Figure 4.3b, the stiffness during unloading/loading for strains $\varepsilon > 0$ is based on the magnitude of the inelastic strains in relation to the ultimate strain, also considered as damage. For strains $\varepsilon \leq 0$ the response remains undamaged. The damage-plasticity model, see Figure 4.3c, is a combination of the plasticity and the damage model.
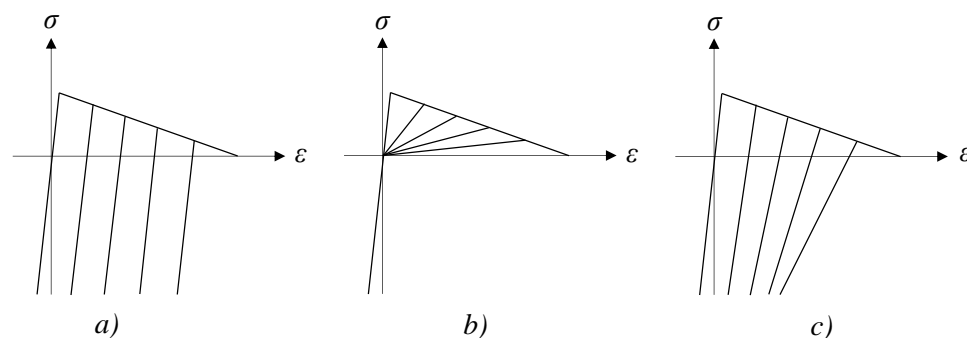

Figure 4.3   Constitutive models for concrete in tension a) plasticity, b) damage and c) damage plasticity.

4.3 Numerical approach

The structural model described in Section 4.2 is analysed using an explicit nonlinear dynamic model. All calculations are carried out using MATLAB®. The principle of the numerical iteration is that for a certain state of displacement u_n, velocity $\dot{u}_n$ and acceleration $\ddot{u}_n$ the displacement is determined at a later time, hence the explicit evaluation method. The updated displacement u_{n+1} is determined based on the current state and the time interval h, see equation (4.5)

$$u_{n+1} = u_n + h \cdot \dot{u}_n + \frac{h^2}{2} \cdot \ddot{u}_n \tag{4.5}$$

Based on the difference between the updated displacement u_{n+1} and the previous displacement u_n, a strain increment $\Delta\varepsilon_{n+1}$ is determined using equation (4.6).

$$\Delta\varepsilon_{n+1} = \frac{u_{n+1} - u_n}{L} \tag{4.6}$$

Using the strain increment $\Delta\varepsilon_{n+1}$ and the previous strain ε_n the element stress is determined. Knowing the stress, an internal force q_{n+1} vector is established using equation (4.7).

$$q_{n+1} = q_n + \Delta q_{n+1}\left(\varepsilon_n, \Delta\varepsilon_{n+1}\right) \tag{4.7}$$

Knowing both the internal force vector and the displacements, the velocity and acceleration vector is solved by combining equation (4.8) and (4.9).

$$M \cdot \ddot{u}_{n+1} + C \cdot \dot{u}_{n+1} + q_{n+1} = F_{n+1} \tag{4.8}$$

$$\dot{u}_{n+1} = \dot{u}_n + \frac{h}{2} \cdot \left(\ddot{u}_n + \ddot{u}_{n+1}\right) \tag{4.9}$$

The mass matrix M in equation (4.8) is for bar elements determined using equation (4.10).

$$M_i = \frac{\rho_i \cdot A_i \cdot L_i}{6} \cdot \begin{pmatrix} 2 & 1 \\ 1 & 2 \end{pmatrix} \tag{4.10}$$

The overall damping C of the system is proportional to the stiffness matrix K_i, shown in equation (4.11), where the constant a is based on the highest response frequency ω_{max} and the damping ratio ξ, see equation (4.12).

$$C_i = a \cdot K_i \tag{4.11}$$

$$a = \frac{2 \cdot \xi}{\omega_{max}} \tag{4.12}$$

The damping ratio ξ used by Ekström is $\xi = 1.4$ (140 %) for the plasticity model and $\xi = 1.0$ (100 %) for the damage- and damage-plasticity model. A scheme of the numerical routine is summarized in Figure 4.4.
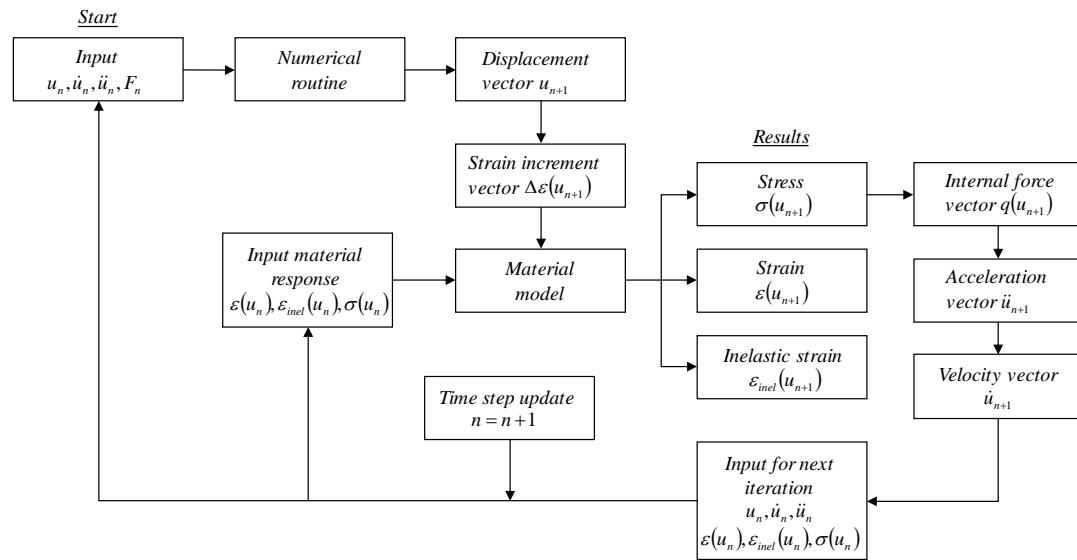
Figure 4.4   Scheme of numerical routine. Based on Ekström (2016).

4.4   Representation of a shock wave in numerical analysis

4.4.1   Overview

The idealized shock wave and pressure time relation *P(t)* described in Figure 4.2 is how one analytically can consider the shape and magnitude of the pressure at any certain time. However, using the numerical approach described in Section 4.3 results in a discrepancy between the analytical and numerical representation of the pressure-time relation. To emphasize this discrepancy, analytical and numerical shock wave profiles are compared in Figure 4.5 at three different locations in the structure, and Table 4.2 summarizes the numerical input. Figure 4.5 illustrates the analytical shock wave profile as a dashed line and the numerical shock wave profile as a solid line. Important in this comparison is to observe that the shock wave propagation is studied for a linear elastic case, with no influence of material strength. For the purpose of illustration, compressive stresses are defined as $\sigma > 0$ and tensile stresses are, consequently, defined as $\sigma < 0$.

Table 4.2   Numerical input for comparing shock wave profiles.

P_{peak} [MPa]	t_{dur} [ms]	N	ξ	h [ms]
50.74	1.31	100	1.0	$2.52 \cdot 10^{-4}$
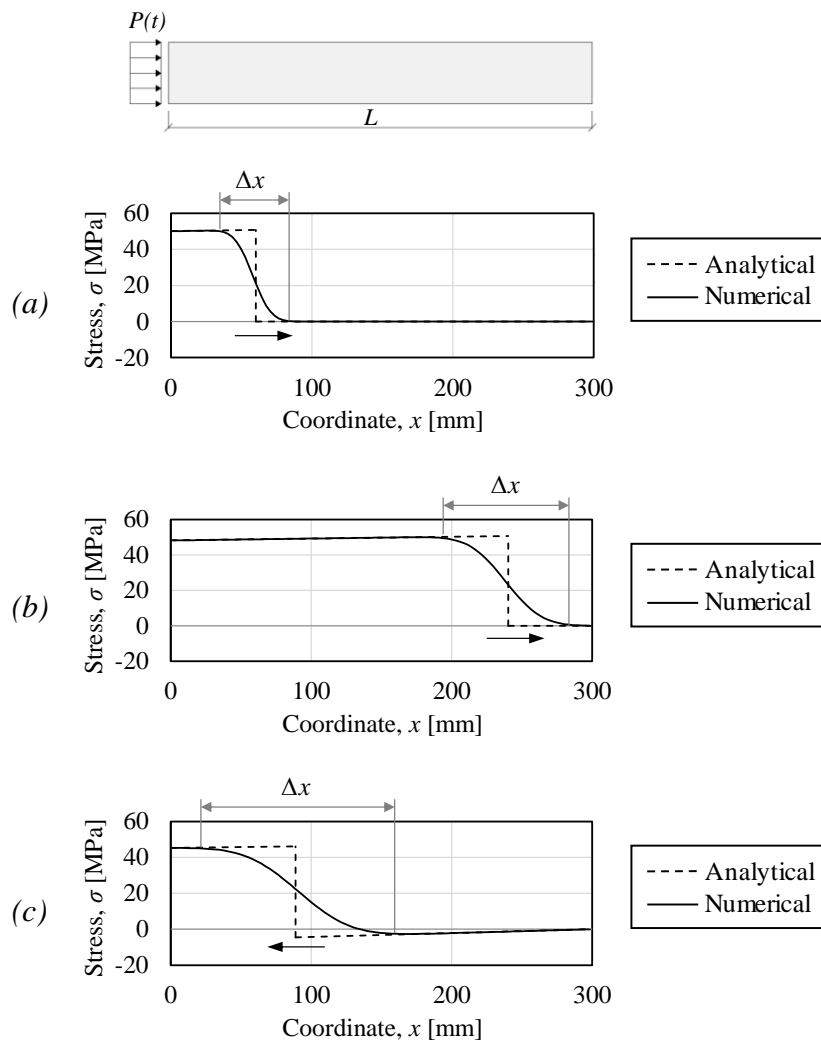
Figure 4.5   *Comparison between analytical (dashed) and numerical (solid) representation of shock wave profile at coordinates (a) 60 mm, (b) 240 mm and (c) 300+210 mm (after reflection).*

This misrepresentation of the shock wave profile in the numerical analysis compared to the analytical is obvious by studying Figure 4.5. The stress difference on each side of the wave front is equalized over a certain distance, Δx, in the numerical approach, which is inaccurate with how one considers the shock wave analytically.

This section will study how the numerical representation of the shock wave profile is influence by the time interval h, damping ratio ξ and number of elements N.

4.4.2   Influence of time interval

The time interval over which the numerical routine updates the displacement u_n, velocity $\dot{u}_n$ and acceleration $\ddot{u}_n$ might influence the accuracy in the numerical representation of the shock wave. Ekström defines the time interval h as

$$h = 0.3 \cdot dt \tag{4.13}$$

where *dt* is the critical time step, i.e. the time it takes for the stress wave to propagate through one element. Figure 4.6 shows how the numerical representation of the shock wave is influenced when reducing the time interval.

Figure 4.6   Comparison of shock wave profiles for time interval (1) h = 0.01dt and (2) h = 0.1dt at coordinates (a) x = 60 mm, (b) x = 240 mm and (c) x=300+210 mm.

The comparison shows that the influence of the time interval is negligible. No improvement in the difference between the analytical and numerical representation of the shock wave is observed.

4.4.3 Influence of damping ratio

The damping of the system can, in a simplified way, be considered to determine the overall energy loss in the system for each time step, why it is possible that this can influence the representation of the shock wave. As seen in Figure 4.7(a), the stress intensity has decreased already at coordinate $x = 60$ mm which could mean that the damping of the system is too high. The influence of the damping ratio ξ is studied by comparing the shock wave for different magnitudes of ξ. The first studied case, illustrated in Figure 4.7, is a comparison between the reference damping ratio $\xi = 1.0$ and $\xi = 0.05$.
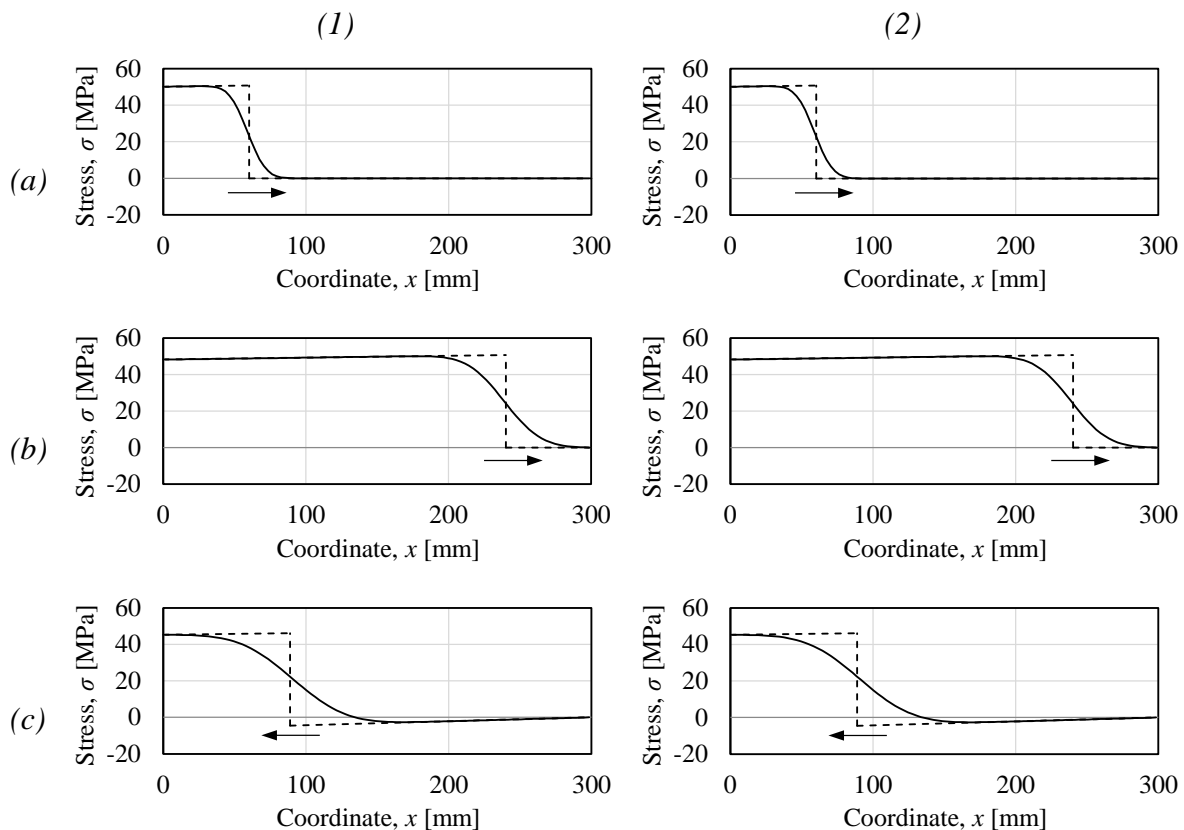
Figure 4.7   Comparison of shock wave profiles for damping ratio (1) ξ = 1.0 and (2) ξ = 0.05 at coordinates (a) x = 60 mm, (b) x = 240 mm and (c) x=300+210 mm.

The conclusion from Figure 4.7 is that the distance, over which the stress difference is equalized, decreases with decreasing damping ratio ξ. However, there is still a certain discrepancy in the numerical and analytical representation. The most obvious of which is the oscillation in stress seen in Figure 4.7(2), which results in net tensile stresses as the wave propagates in compression. Hence, if the damping ratio is too low, inelastic strains can develop in tension as the shock wave propagates in compression.

By this reasoning, a damping ratio in the system of ξ = 0.05 is too low to accurately describe the behavior of the shock wave. Therefore, higher values of ξ must be considered. Figure 4.8 illustrates the different behavior for damping ratios ξ = 0.2 and ξ = 0.5. At damping ratio ξ = 0.2 the numerical approach still becomes unstable, see Figure 4.8(1), while for damping ratio ξ = 0.5 it appears to be more or less stable. However, if this model is studied more in detail, tensile stresses still arises as the wave propagates in compression. Therefore, the conclusion is that a damping ratio must be greater than ξ = 0.5 if the original mesh density is used. If, however, such a damping ratio is used the distance over which the stress difference equalizes becomes similar to the one shown in Figure 4.8(1), i.e. the original damping ratio. This is also mentioned in Ekström (2016) and is the reason why such a large damping ratio as 100-140 % where used in his analyses.
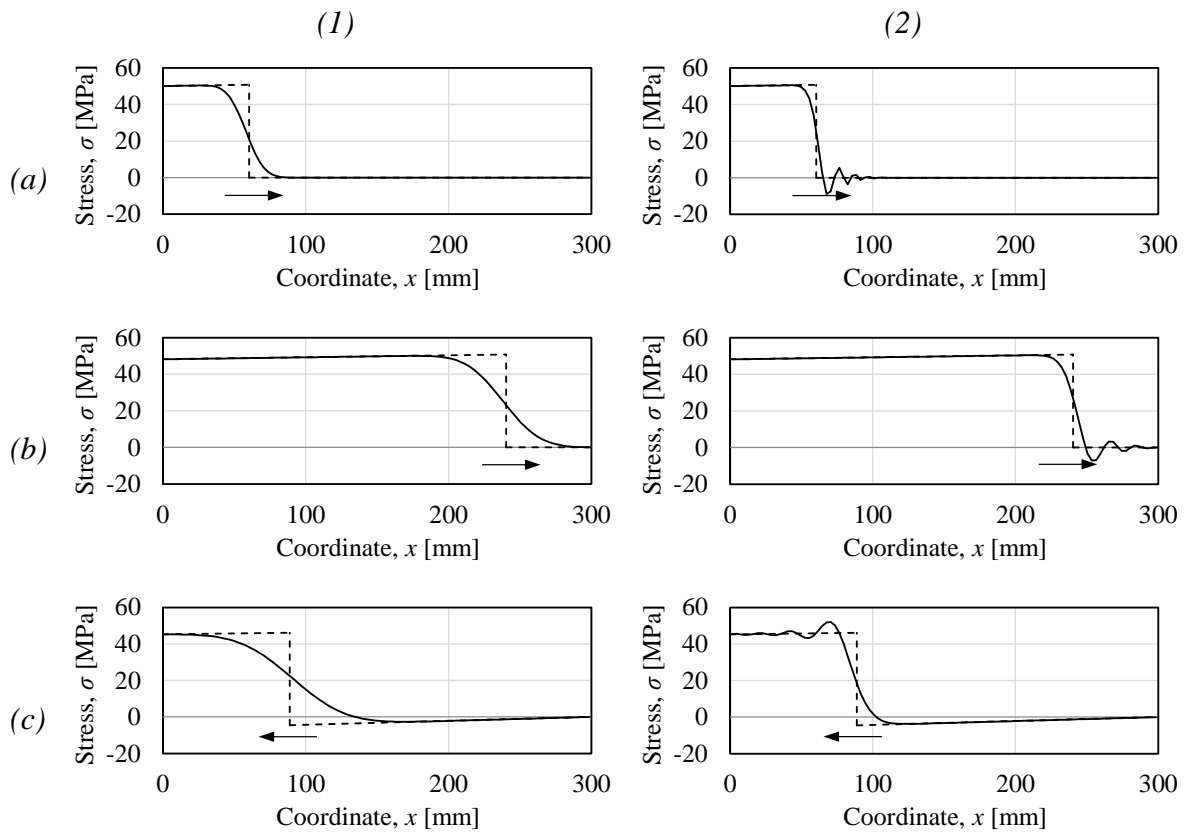
Figure 4.8   Comparison of shock wave profiles for damping ratio (1) ξ = 0.2 and (2) ξ = 0.5 at coordinates (a) x = 60 mm, (b) x = 240 mm and (c) x = 300+210 mm.

For the purpose of illustration, higher damping ratios than the reference damping $\xi = 1$ is also considered to highlight the behavior. Therefore, damping ratios $\xi = 3$ and $\xi = 5$ are compared and illustrated in Figure 4.9. The conclusion of this figure is that the distance over which the stress difference neutralizes increases as the damping ratio increases, and becomes too inaccurate for higher damping ratios.
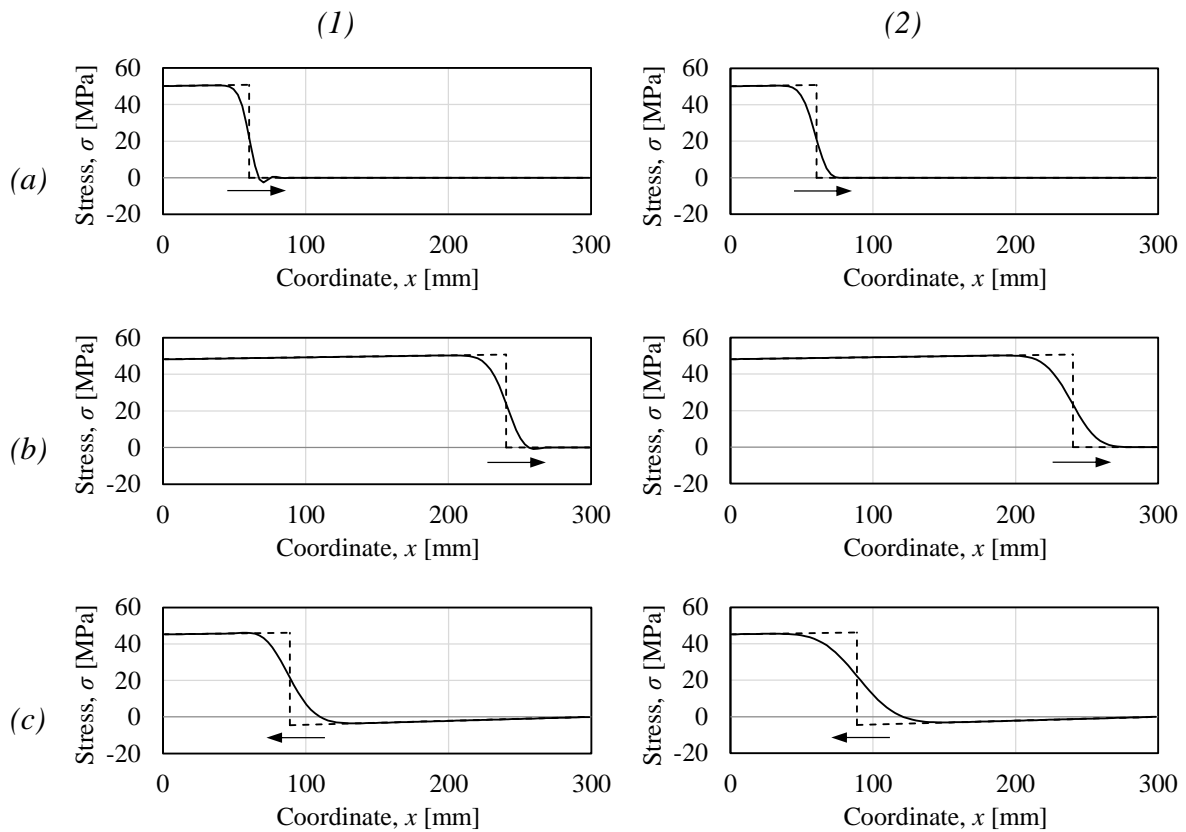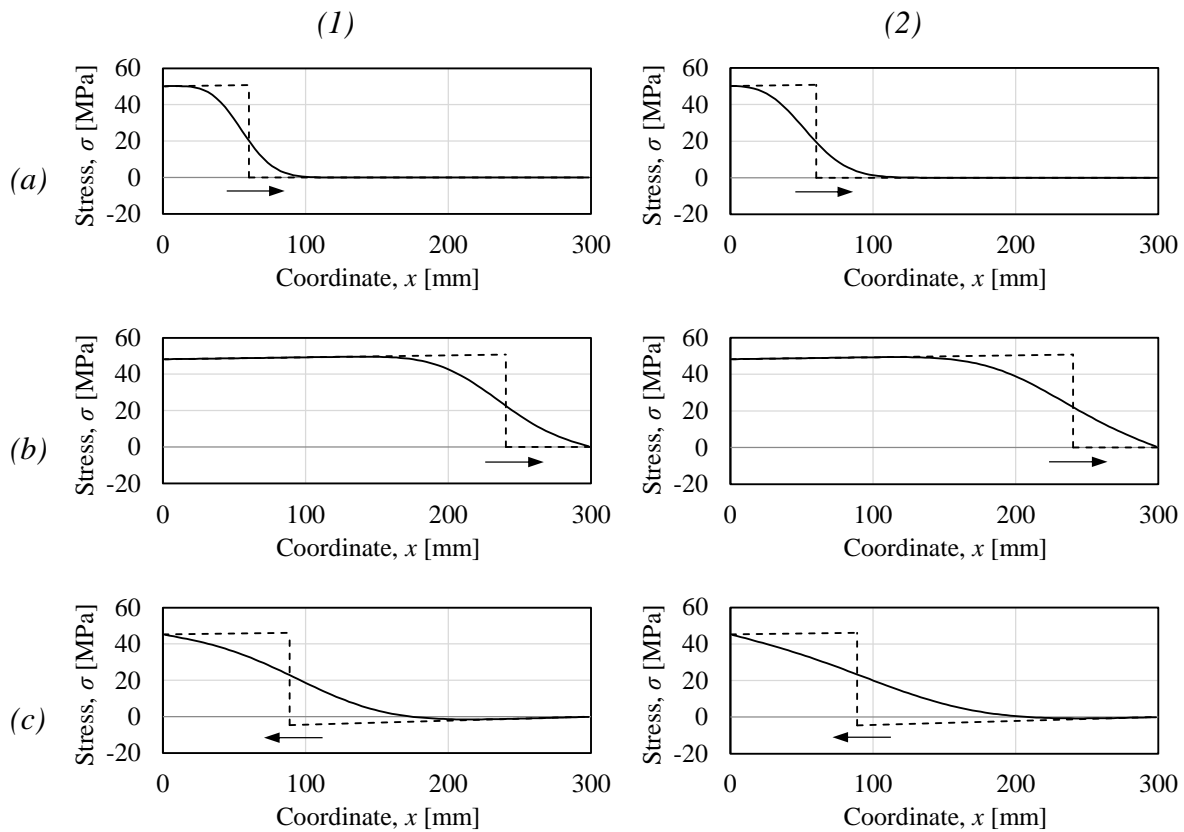
Figure 4.9 *Comparison of shock wave profiles for damping ratio (1) ξ = 3 and (2) ξ = 5 at coordinates (a) x = 60 mm, (b) x = 240 mm and (c) x = 300+210 mm.*

To summarize, the influence of the damping ratio is highly important when describing the propagation of a shock wave. Considering the distance that it takes for the compression wave to reach peak pressure, lower damping ratios are favorable as shown in Figure 4.7(2). However, lower damping ratios results in oscillation which can cause tensile stresses when the wave propagates in compression. Therefore, the damping ratio must be of such magnitude that these oscillations do not take place. This is why the conclusion is that the damping ratio cannot alone adjust for the discrepancy seen in the numerical and analytical approach.

4.4.4 Influence of mesh density

The number of elements N used in the analysis is also a possible factor that might adjust for the discrepancy seen in Figure 4.5. Therefore, the number of elements is compared with the same principle as the damping ratio ξ. The number of elements in the reference model is set to $N = 100$, i.e. the same number of elements used in Ekström's analysis, and will be compared with $N = 50$ and $N = 800$.

The first comparison is between $N = 100$ and $N = 50$ elements, shown in Figure 4.10. The conclusion of this illustration is that if fewer elements are used, see Figure 4.10(2), the larger distance it takes for the stress wave to equalize the stress difference. This also leads to that the actual stress intensity of the shock wave decreases, i.e. the shock wave will become less able to fully represent the peak pressure P_{peak} given as input in the analysis.

Figure 4.10   Comparison of shock wave profiles for (1) 100 elements and (2) 50 elements at coordinates (a) x = 60mm, (b) x = 240 mm and (c) x = 300+210 mm.

For this reason, it is important to consider to opposite case where the number of elements *N* increases. This comparison is illustrated in Figure 4.11, which shows that by increasing the number of elements, the numerical shock wave profile is more accurately depicted compared with the analytical. As seen in Figure 4.11(2a), the stress intensity when using *N* = 800 elements is very similar to the analytical solution. This observation suggests that the numerical approach converges towards the analytical approach as the number of elements increases. However, one can still observe the loss in stress intensity when comparing Figure 4.11(2) at the three different coordinates in the structure. This suggests that the number of elements *N*, like for the damping ratio *ξ*, cannot alone adjust for the difference between numerical and analytical representation.
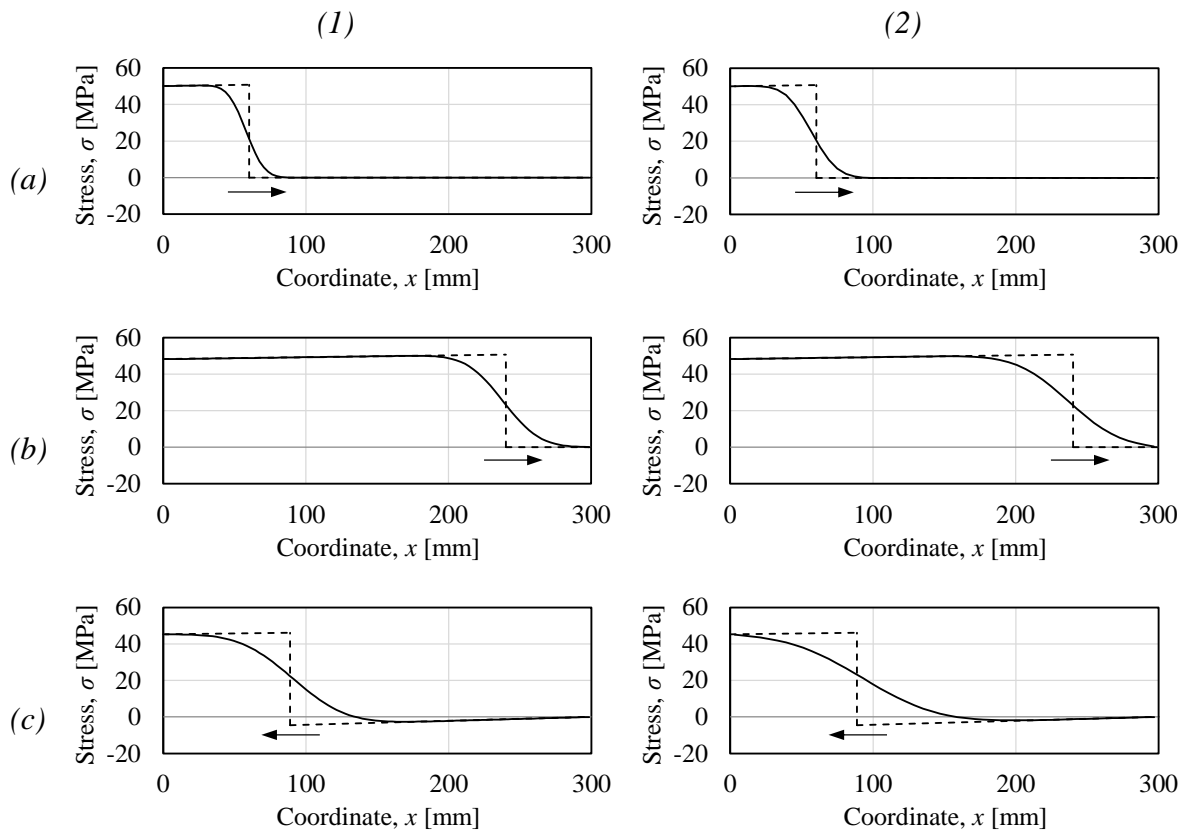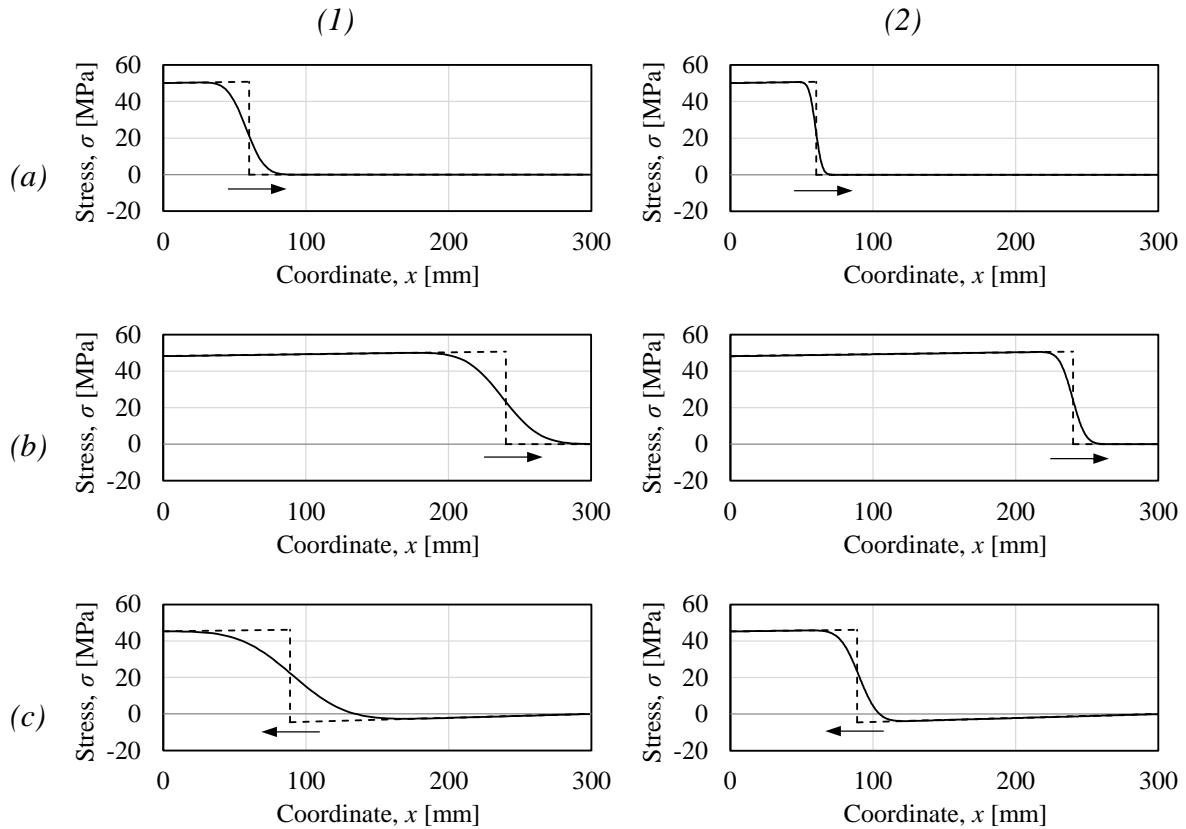
Figure 4.11   Comparison of shock wave profiles for (1) 100 elements and (2) 800 elements at coordinates (a) x = 60mm, (b) x = 240 mm and (c) x = 300+210 mm.

4.4.5   Combined influence of damping and mesh density

Even though the shock wave representation was improved substantially by increasing the number of elements, see Section 4.4.4, there is still some difference between the analytical solution and the numerical. Therefore, this section aims to combine the influence of the damping ratio ξ and number of elements N to determine whether the solution becomes more accurate. The strategy is to see whether using a low damping ratio ξ and high number of elements N could improve the shock wave representation even further. The input for these comparisons are summarized in Table 4.3.

Table 4.3   Input for comparing the combined influence of damping ratio and number of elements.

P_{peak} [MPa]	t_{dur} [ms]	ξ [-]	N [-]
50.74	1.31	0.05	800
50.74	1.31	0.1	800
50.74	1.31	0.1	2000
50.74	1.31	0.2	2000

The first comparison if performed using damping ratio $\xi = 0.05$ and $\xi = 0.1$ for $N = 800$ elements. As illustrated in Figure 4.12, there is a substantial reduction of the stress oscillation for lower damping ratios. Further, the difference between the analytical peak stress and the numerical decreases even more. For the configurations

studied in Figure 4.12 the numerical shock wave profile is very similar to the analytical one. There is still, however, small oscillations in the stress profile causing tensile stresses as the wave propagates in compression.
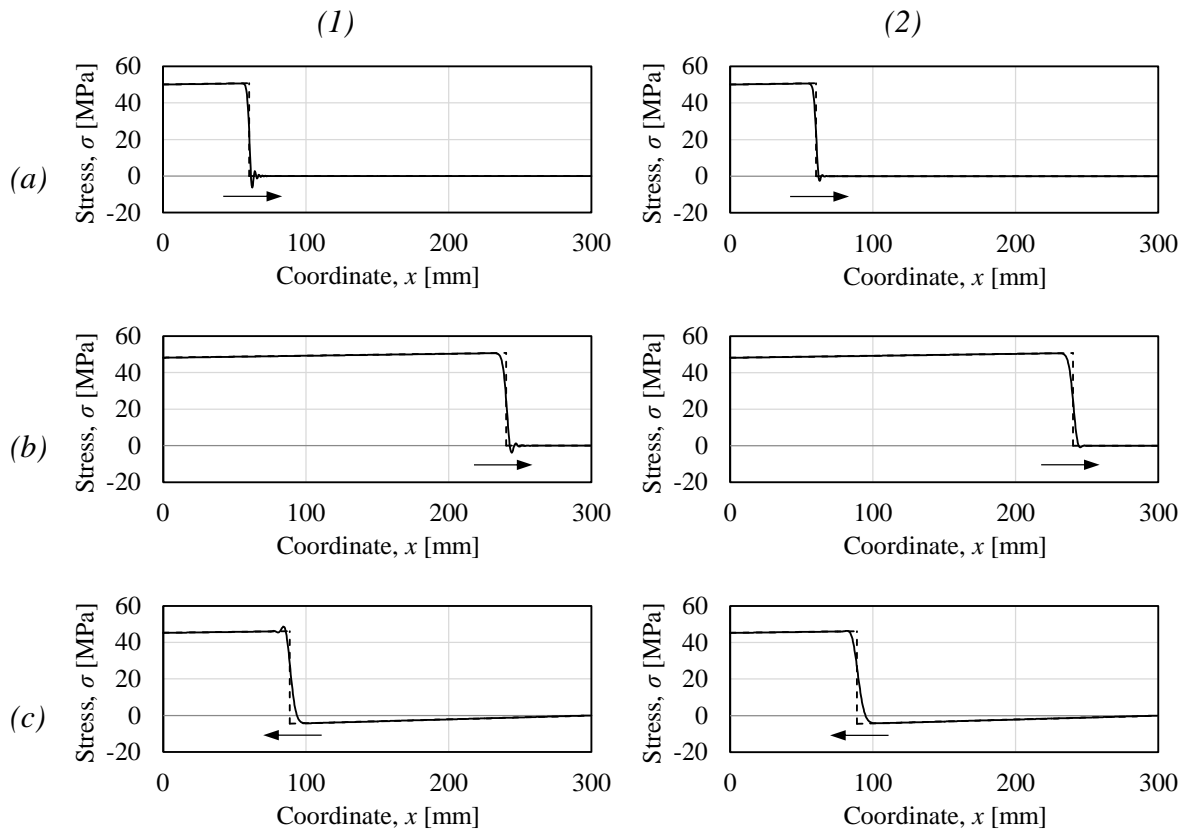
Figure 4.12   *Comparison of shock wave profiles for damping ratio (1) ξ = 0.05 and (2) ξ = 0.1 using N = 800 elements at coordinates (a) x = 60mm, (b) x = 240 mm and (c) x = 300+210 mm.*

Figure 4.12 further suggests that increasing the number of elements could improve the model even more for low damping ratios. This effect becomes clear when the same comparison is performed for $N = 2000$ elements. This comparison is given in Figure 4.13 and shows that the shock wave is represented even more accurate when using $N = 2000$ elements.
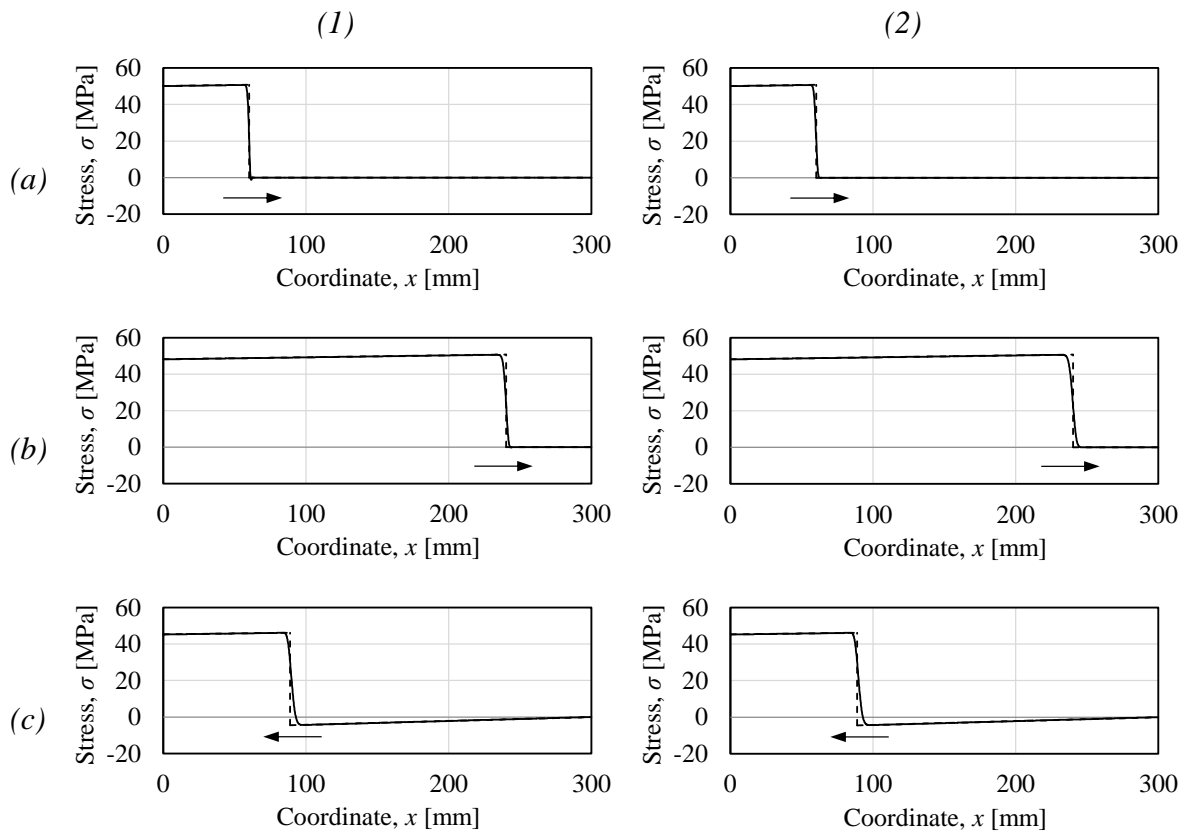
Figure 4.13   Comparison of shock wave profiles for damping ratio (1) ξ = 0.1 and (2) ξ = 0.2 using N = 2000 elements at coordinates (a) x = 60mm, (b) x = 240 mm and (c) x = 300+210 mm.

The conclusion of this section is that the magnitude of the damping ratio ξ and the number of elements N are highly important parameters that will influence how the model numerically represent the shock wave.

4.4.6 Shock wave representation for increased pressure time gradient

In addition to comparisons of shock wave representation when changing the time interval, damping ratio and mesh density, the gradient of the pressure time relation is also of interest. Since variation in load duration, i.e. pressure time gradient, is of interest in the parametric study in Section 4.6, this section aims to highlight how the numerical model represents a shock wave with shorter load duration.

The comparison is made between the original load duration, 1.31 ms, and when the load duration is decreased substantially to 0.04 ms, see Figure 4.14. From this, it can be concluded that the stress intensity in Figure 4.14(2) cannot be considered to fully represent the peak pressure P_{peak}, which is used as input in the analysis.
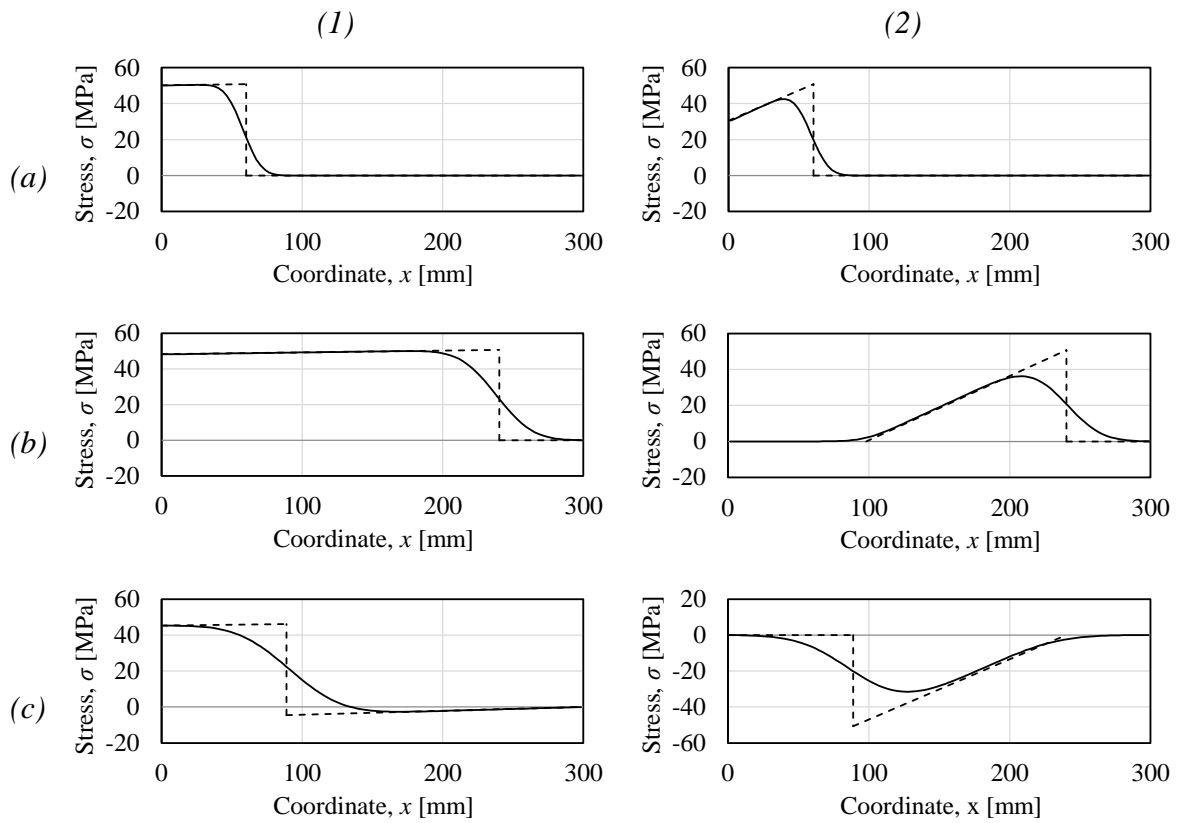
Figure 4.14   Comparison   of   shock   wave   profiles   for   load   durations (1) $t_{dur} = 1.31$ ms and (2) $t_{dur} = 0.04$ ms at coordinates (a) x = 60mm, (b) x = 240 mm and (c) x = 300+210 mm.

4.5 Development of inelastic strains

Since the studied shock wave propagation in Section 4.4 was performed for a linear elastic material in both compression and tension, no damage in the material could be observed. However, as the wave propagates in tension, crack initiation will occur and cause inelastic strains as the tensile stress reaches the tensile strength. This can be illustrated by showing how inelastic strains are distributed over the structural element as well as the corresponding material response for a certain element. These graphs are principally shown in Figure 4.15. Also shown in Figure 4.15(1) is two lines describing the ultimate inelastic strain ε_u (dashed-dot horizontal line) and the coordinate at which the conventional theory by McVay (1988) predicts spalling (dashed vertical line).
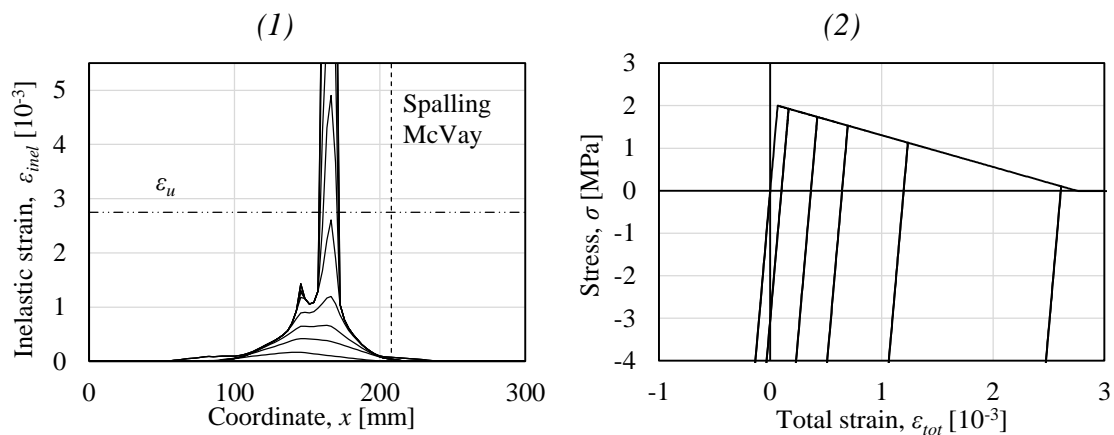
Figure 4.15   Illustration of how (1) inelastic strains and (2) the corresponding material response is used to evaluate spalling.

Another important aspect of how to describe the development of inelastic strain is to determine how to define the position of the shock wave front. In further illustrations, one load cycle is defined as every time the shock wave front reaches the opposite free edge after propagating in tension. This principle is illustrated in Figure 4.16.
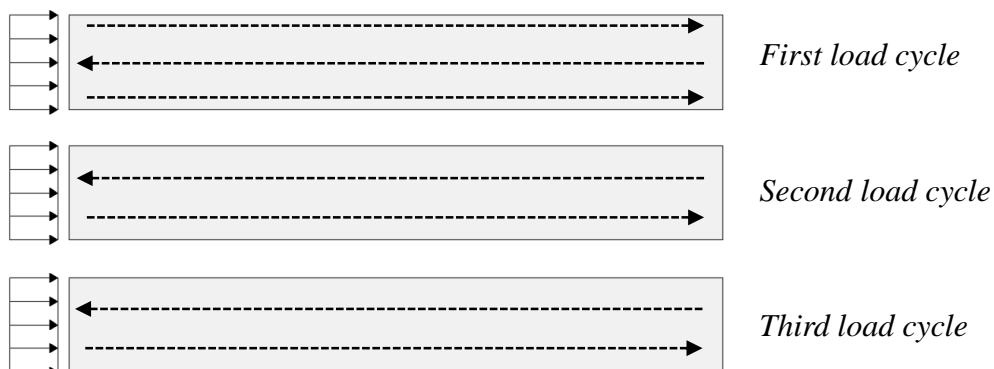
Figure 4.16   Definition of the position of the shock wave for different load cycles.

Using this principle, it is possible to study the structural response, in terms of the development of inelastic strains, for different load cycles. This is shown in Figure 4.17 where inelastic strains and the corresponding material response is shown after different number of load cycles, when a plasticity model is used.
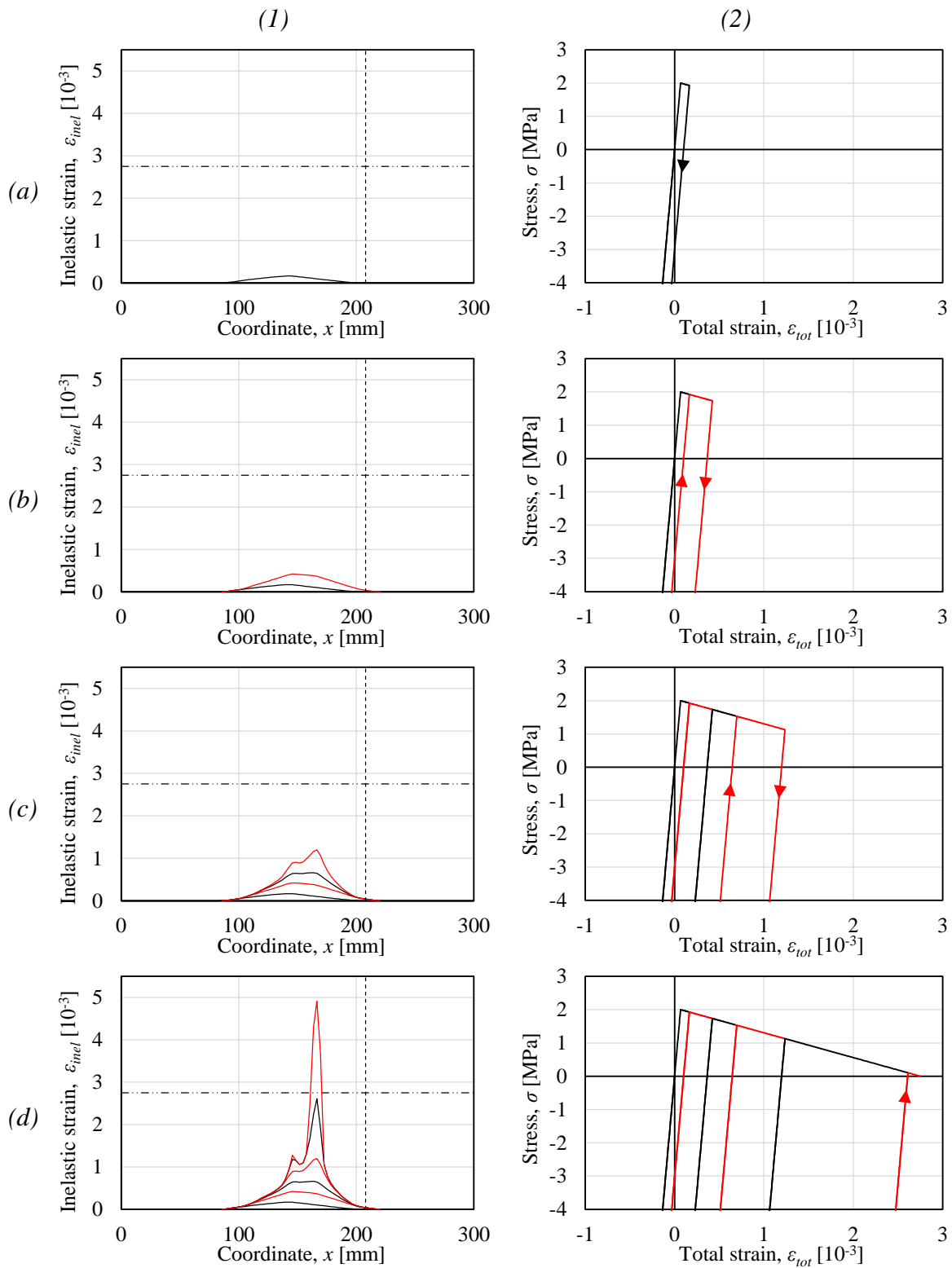
Figure 4.17 (1) Development of inelastic strains and (2) corresponding material response after (a) one load cycle, (b) two load cycles, (c) four load cycles and (d) six load cycles for a plasticity model.

4.5.1 Presented results

The results presented in Ekström's licentiate thesis consist of distribution of inelastic strains and corresponding material response for the three different material models described in Section 4.2.1. These results are presented in Figure 4.18 and supports Ekström's claim that spalling does not necessarily occur at the same location as predicted by McVay (1988). Further, it confirms that the development of inelastic strains, i.e. the spalling process, does not occur instantaneously but rather during cyclic loading/unloading. Therefore, the structural response during cyclic loading/unloading is an important aspect when evaluating spalling. In addition to Figure 4.18, Table 4.4 summarizes the position of crack initiation and spalling crack for the different material models as well as the position of the spalling crack predicted by McVay (1988).
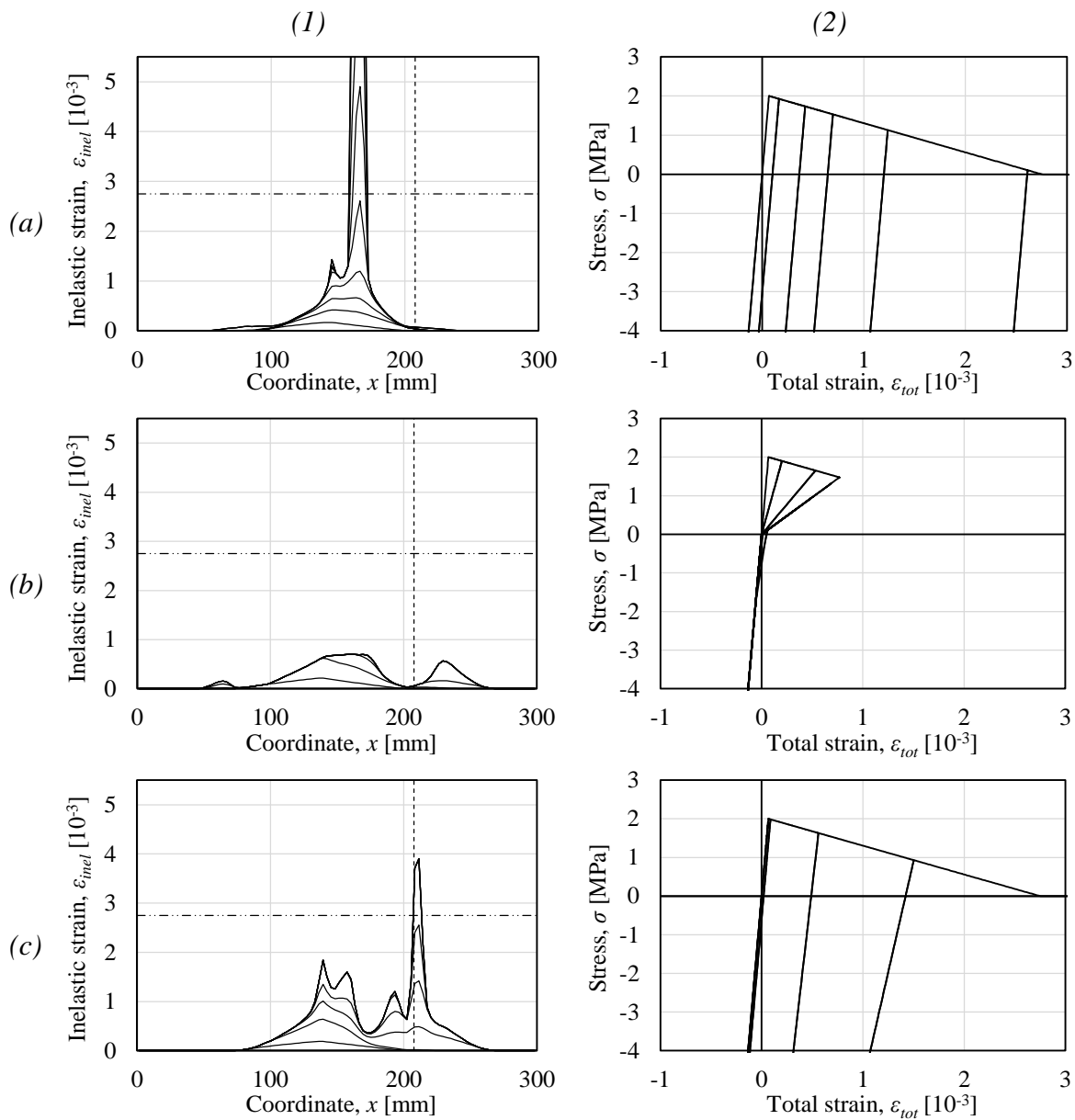
Figure 4.18   Spalling evaluation presented by Ekström for material model (a) plasticity, (b) damage and (c) damage-plasticity.

Table 4.4 *Position of crack initiation and spalling crack (defined from the right side of the structure) for different material models, based on Ekström (2016).*

Method	Crack initiation [mm]	Spalling crack [mm]
McVay (1988)	92	92
Plasticity	97	140
Damage	97	-
Damage-plasticity	97	92

The reason why crack initiation analytically predicted by McVay, is different from the resulting crack initiation in the numerical analysis is due to the discrepancy in shock wave representation discussed in Section 4.4. Since the analytical peak pressure is greater than the numerical peak pressure, crack initiation will appear earlier in McVay (1988), i.e. the spalling depth $S_{d,i}$ will decrease as P_{peak} increases in equation (4.14).

$$S_{d,i} = \frac{c \cdot t_{dur} \cdot f_t}{2 \cdot P_{Peak}} = 92 \text{ mm} \tag{4.14}$$

It will be shown later, in Section 4.6.6, that crack initiation will converge towards the result predicted by McVay, the more accurately the numerical shock wave resembles the analytical one.

Another comment regarding the result presented in Figure 4.18(b), i.e. for the damage model, is that the distribution of inelastic strains differs somewhat from the result presented by Ekström (2016). The reason for this is that Ekström includes the elastic part of the strain in the graphs for inelastic strains. The consequence of this is that inelastic strains are predicted all the way out to the far right in the structure. To illustrate this difference, Ekström's result and the modified results are illustrated and compared in Figure 4.19.

Figure 4.19 *Comparison between distribution of inelastic strains using a damage model for (1) including elastic strains (Ekström, 2016) and (2) excluding elastic strains.*

4.6 Parametric study

4.6.1 Input parameters

The chosen material model that represent the response under cyclic loading described in Section 4.2.1 is important in terms of the development of inelastic strains. However, variations in geometry, material properties and load intensity in these models will have an influence on the structural response as well. In order to evaluate the e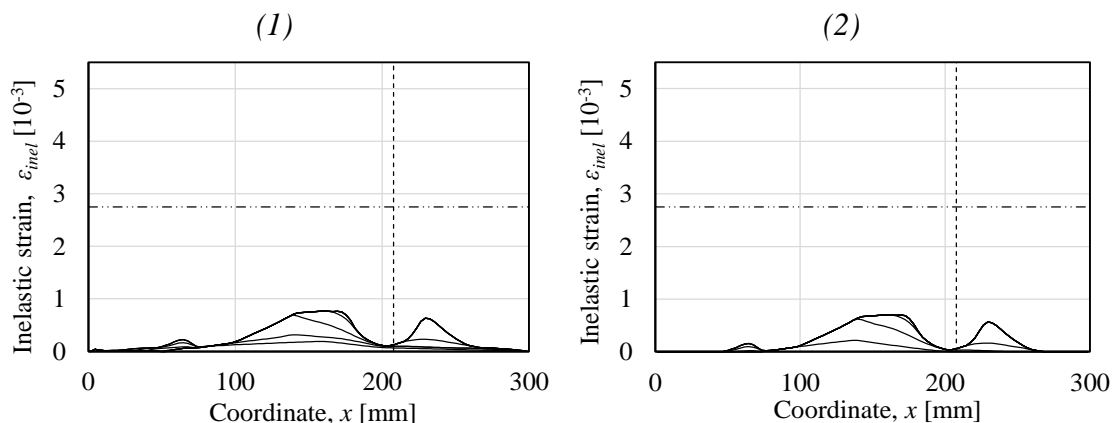xtent of the influences of different input parameters as well as the accuracy of the model presented by Ekström, a parametric study is performed and presented in the following sections.

A model based on the input parameters summarized in Table 4.1 will be used as a reference model and are compared to the results of each parametric variation. The parameters included in the study and the specific variations are presented in Table 4.5, where the reference values are underlined. The different parameters are intended to be analysed individually, with the other parameters set to the reference model.

Table 4.5 Variation of the input values included in parametric study. Reference values used in basic analysis are underlined.

Parameter	Variations	Value
Load duration, t_{dur}	[0.05, 0.1, 0.5, <u>1.0</u>, 1.5] $\cdot t_{dur}$	$t_{dur} = 1.31$ ms
Concrete thickness, L	[0.5, <u>1.0</u>, 1.5, 2] $\cdot L$	$L = 300$ mm
Peak pressure, P_{peak}	[0.4, <u>1.0</u>, 1.4] $\cdot P_{peak}$	$P_{peak} = 50.74$ MPa
Tensile strength, f_{ct}	[0.5, <u>1.0</u>, 2, 3] $\cdot f_{ct}$	$f_{ct} = 2$ MPa
Number of elements N	[0.5, <u>1.0</u>, 2, 4, 8] $\cdot N$	$N = 100$
Damping, ξ	[0.1, 0.3, 0.7, <u>1.0</u> (<u>1.4</u>) , 3.0] $\cdot \xi$	$\xi = 1.0$

Results are presented mainly for the plasticity model, since the tendency of each individual parametric variation is mostly the same for the three material models. However, if a difference can be observed, this will be emphasised and discussed.

The determination of the crack band width, over which the representation of cracks is smeared out over, is a critical process. The numerical response is accurate only if the resulting cracked region in the analysis is equal to the assumed crack band width, and should be evaluated after each analysis. This process is excluded in this parametric study and instead further treated in Section 4.9 together with the concept of fracture energy.

4.6.2 Load duration

4.6.2.1 Plasticity model

As stated in Section 4.2, the analysed pressure wave is represented by pressure as a function of time, *P(t)*. The time over which the pressure wave acts on the structure is defined as the load duration, t_{dur}. The load durations analysed in the parametric study are presented in Table 4.6.

Table 4.6   Variations of load duration, t_{dur} analysed in the parametric study.

Parameter	Value [ms]	Def.
t_{dur}	1.31	Long
$0.05 \cdot t_{dur}$	0.0655	Short
$0.1 \cdot t_{dur}$	0.131	Short
$0.5 \cdot t_{dur}$	0.655	Long
$1.5 \cdot t_{dur}$	1.965	Long

A pressure wave can be distinguished between short and long load duration, as discussed in Section 2.2.4. However, the main difference between the two cases is for a pressure wave with a short load duration, or consequently a large pressure-time gradient, $\partial p/\partial t$, the net tensile stress wave will increase at a higher rate than for a longer load duration. Therefore, the spalling depth predicted by McVay (1988) using equation (4.15), increase with the load duration, as can be seen in Figure 4.20(b).

$$S_{d,i} = \frac{c \cdot f_t}{2 \cdot \left| \dfrac{\partial p}{\partial t} \right|} \qquad (4.15)$$

Further, a higher pressure-time gradient allows the inelastic strains to develop during a longer time before unloading as the pressure wave propagates in tension. For load durations defined as short using the methodology presented in Section 2.2.4 ($t_{dur} < 2$ L/c) the pressure wave is not long enough to unload the structure in tension at all. A consequence of this is that the number of load cycles required to reach a fully developed crack decrease for short load durations, as can be observed in Figure 4.20(b), where a crack is fully developed during the first load cycle. However, for longer load durations, the pressure-time gradient will decrease. Therefore the predicted location $S_{d,i}$ for the crack initiation in equation (4.15) will increase as well as the number of load cycles required to reach a fully open crack. This can also be observed in Figure 4.20(c).
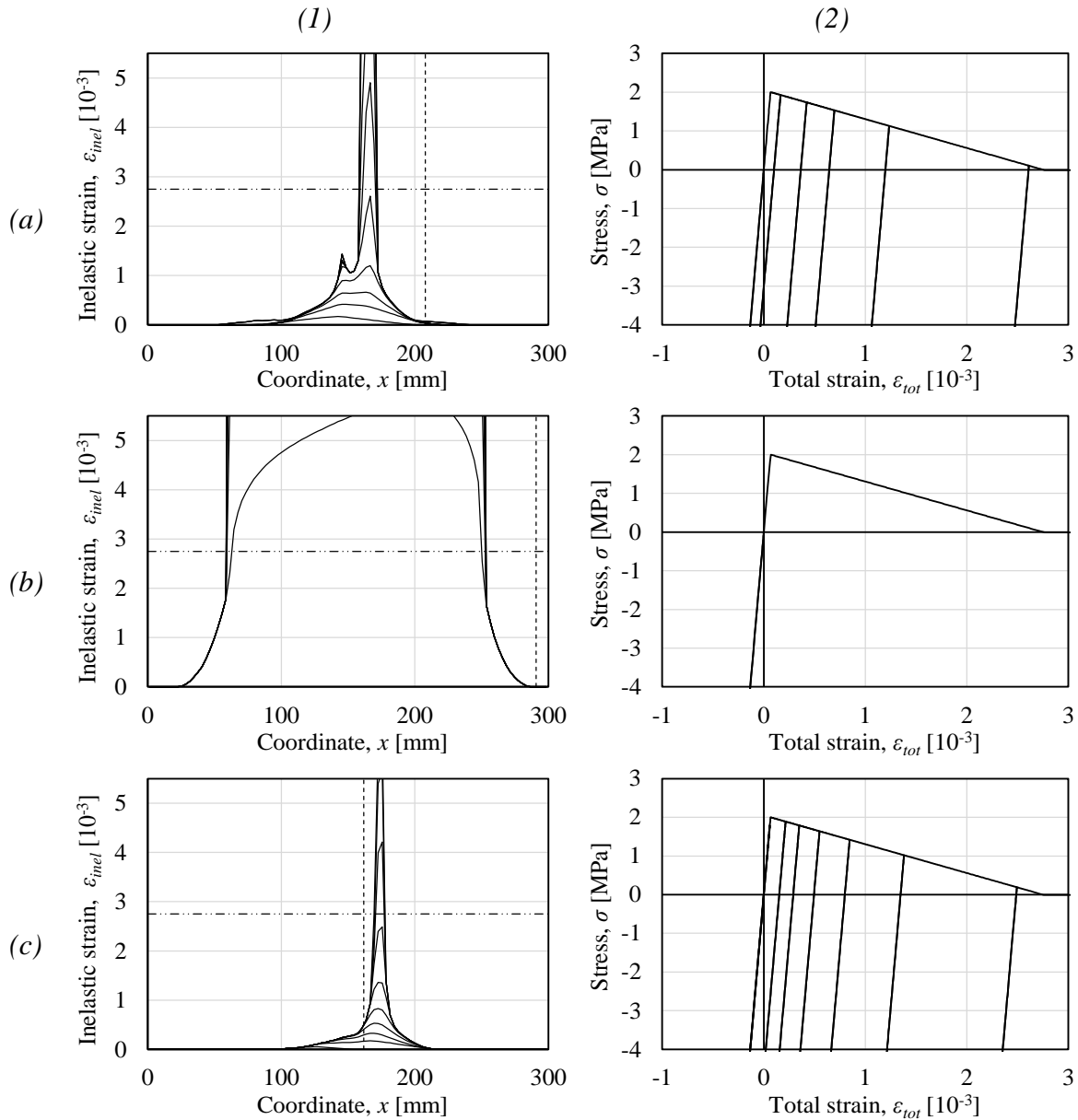
Figure 4.20   *(1) Distribution of inelastic strains and (2) corresponding material response for load duration (a) t_{dur} = 1.31 ms, (b) t_{dur} = 0.131 ms, (c) t_{dur} = 1.965 ms.*

4.6.2.2   Damage and damage-plasticity models

The results from the damage and damage-plasticity models show a similar response as the plasticity model in Section 4.6.2.1. The most obvious similarity is the response for short load durations i.e. t_{dur} = 0.131 ms, where the results of the three models are virtually identical, as can be seen in Figure 4.21. This is considered reasonable, since the difference between the models is the behaviour during unloading. In accordance with Section 4.6.2, there will not be any unloading in the structure due to the short load duration and therefore no difference between the material models is observed.

For longer load durations, the same tendencies that are observed for the plasticity model, is seen for the other two models as well; i.e. the number of load cycles to reach a fully developed crack increase with increasing load duration. All results relating to load duration for the three material models can be found in Appendix B1 and C1.
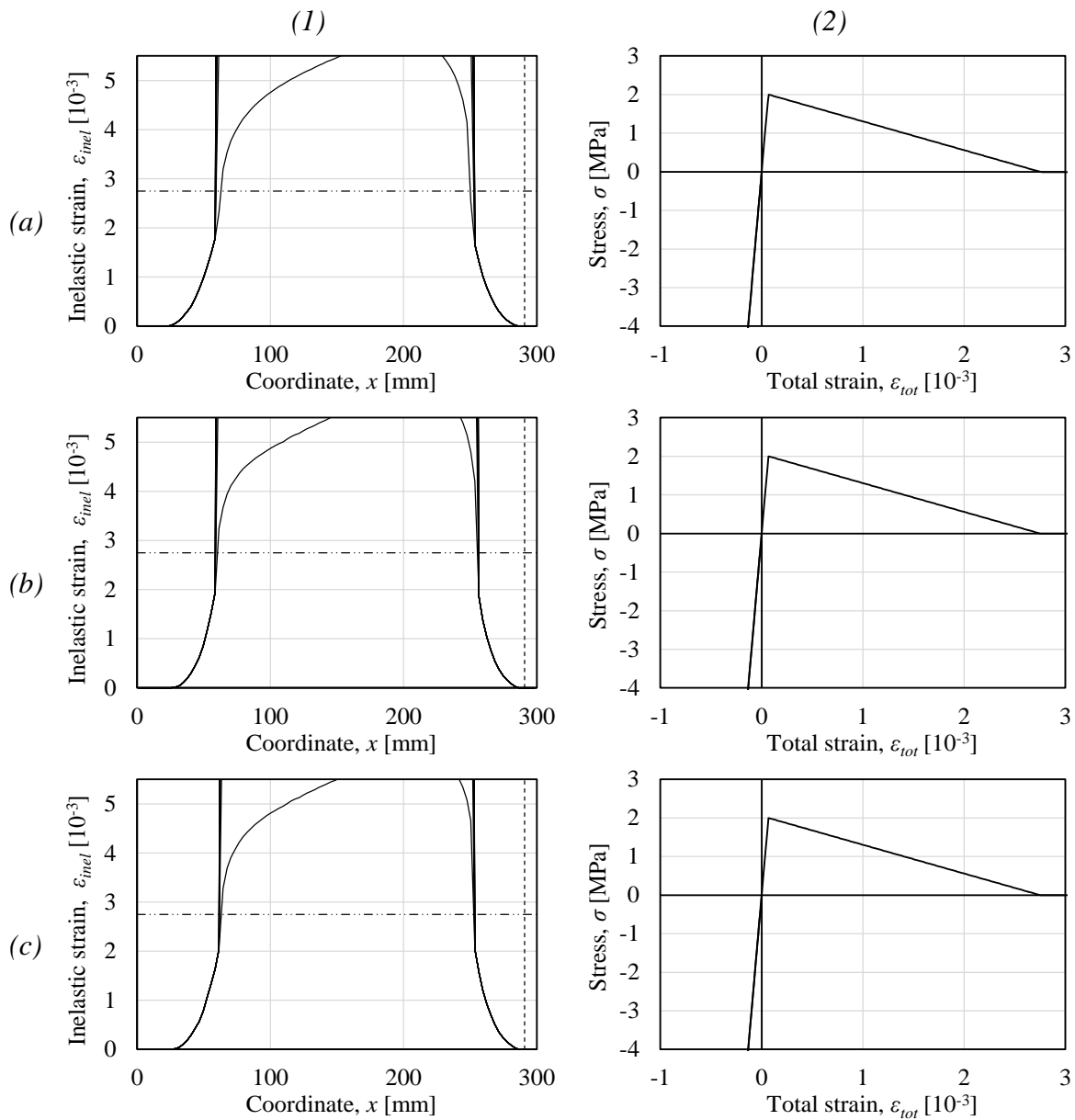
Figure 4.21 *(1) Distribution of inelastic strains and (2) corresponding material response for load duration t_{dur} =0.131 ms for (a) plasticity model, (b) damage model and (c) damage-plasticity model.*

4.6.3 Concrete thickness

The concrete thickness L represents the thickness of the analysed concrete element, expressed in millimetres. The input thickness in the reference model presented by Ekström is 300 mm, and further variations is presented in Table 4.7.

Table 4.7   Variations of concrete thickness, L included in the parametric study.

Parameter	Value [mm]
L	300
0.5L	150
1.5L	450
2L	600

Any variation of concrete thickness in the analysis, in fact corresponds to a change in the representation of the shock wave. For example, if the concrete thickness is doubled, the conceptual response is identical to that of the original thickness and half the load duration, see Figure 4.22. Consequently, the crack initiation position will vary in accordance with the reasoning in Section 4.6.2, which implies that the spalling depth will increase with increased load duration, while in relation to the thickness, it will remain constant.
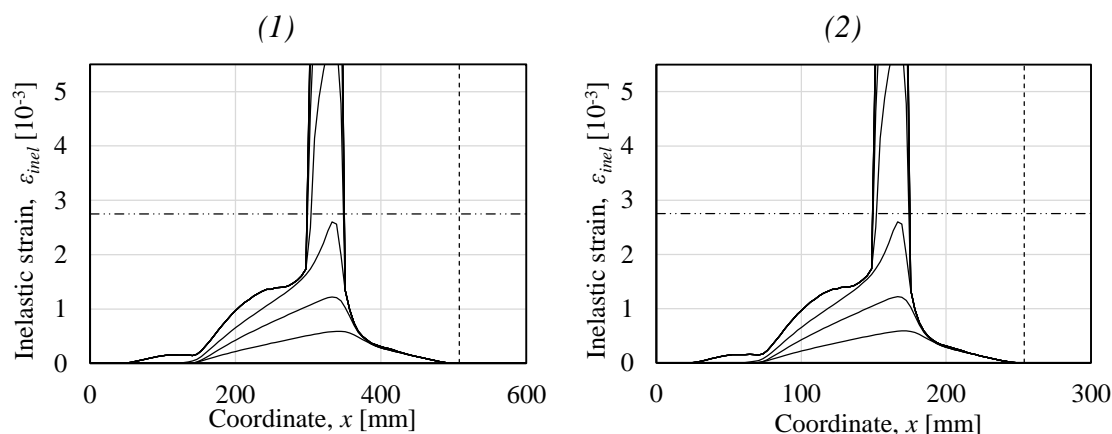
Figure 4.22   Comparison between distribution of inelastic strains for (1) L = 600 mm, t_{dur} = 1.31 ms and (2) L = 300 mm, t_{dur} = 0.655 ms.

However, the process of adjusting the assumed fracture zone to correspond to the one achieved in the analysis will differ from that in the reference model, since the crack is smeared out over a distance twice as long when L = 600 mm.

The conclusion is that it is not the concrete thickness alone that determine the response, but rather the shape of the pressure wave in relation to the thickness. This tendency can also be seen for the other material models as well as the additional variations presented in Table 4.7. These results, though, are presented in Appendix B2 and C2.

4.6.4   Peak pressure

4.6.4.1   Plasticity model

The peak pressure, P_{peak} is the initial value in the force vector F_n for the first iteration in the numerical routine, which in turn is used to determine the initial acceleration $ü_n$. Since the analysis is based on a one dimensional finite element model, the pressure used as input is transformed to a force in accordance with equation (4.4) in Section 4.2.

The reference value of 50.74 MPa used in the model presented by Ekström corresponds to a hemispheric explosion of 1500 kg TNT from a distance of 5 m and is

calculated using the software presented in ConWep (1992). Further variations of the peak pressure analysed in the parametric study are derived in the same way based on different explosion magnitudes and ranges, see Table 4.8.

Table 4.8   *Peak pressures, P_{peak} analysed with corresponding charge weights and distances.*

Charge weight [kg]	Distance [m]	Load duration [ms]	Peak pressure [MPa]
1500	5	1.31	50.74
2500	5.5	1.31	70
900	7	1.31	20

As previously stated in Section 4.5.1, any variation of the peak pressure will have an influence on the predicted position of the first spalling crack. An increase in pressure-time gradient in equation (4.15) will result in a higher gradient of the net tensile wave, and therefore a decrease in the spalling depth. This position is predicted based on the gradient of the first tensile wave.

For cases with low peak pressure, the gradient of the first net tensile wave is not high enough to reach the tensile strength before unloading. Thus, the predicted spalling position is considered to be inaccurate. Instead, the first crack is initiated further to the right, see Figure 4.23(b). This is because the gradient of the net tensile wave in the following load cycles will increase, i.e. the crack is initiated in the second load cycle, not the first. However, as the peak pressure increases, resulting in a crack initiation during the first load cycle, the predicted spalling position is considered more accurate, see Figure 4.23(c).

Figure 4.23 *(1) Distribution of inelastic strains and (2) corresponding material response for peak stress (a) $P_{peak} = 50.74$ MPa, (b) $P_{peak} = 20$ MPa and (c) $P_{peak} = 70$ MPa.*

4.6.4.2 Damage and damage-plasticity models

It seems, when analysing the results presented in Figure 4.23, that the spalling crack is developed in about the same position for the different peak pressures. This position is determined by which element that can develop inelastic strains over the longest time, during the first load cycles. The same tendency can be observed during the initial load cycles for the damage and damage-plasticity model as well. However, the unstable state of the pressure wave after the first load cycles in these models, can cause a fully developed crack to form at a different position. For the damage-plasticity model, this is illustrated in Figure 4.24(c). The same result are presented for the damage model in Appendix xx.
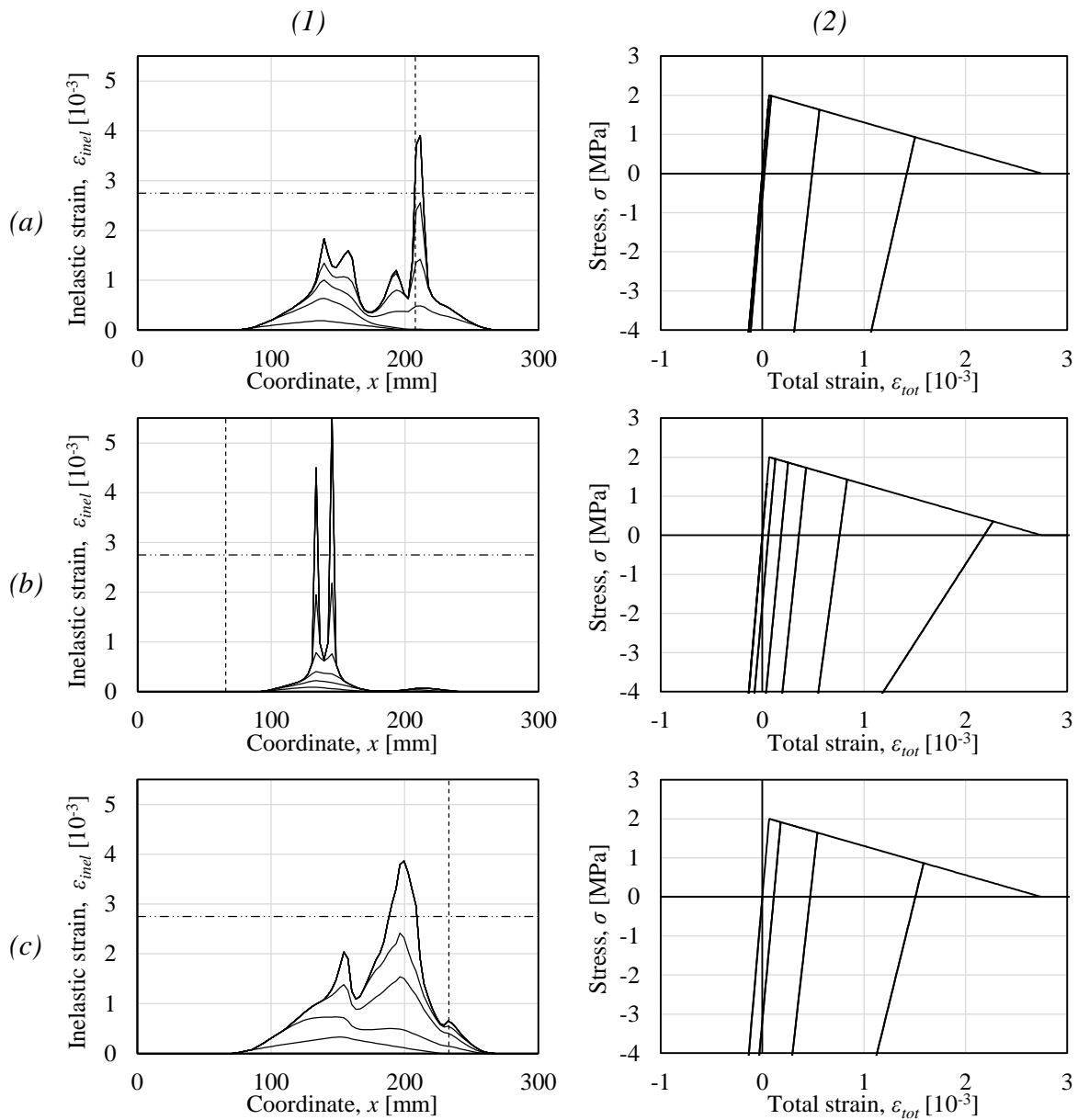
Figure 4.24 *(1) Distribution of inelastic strains and (2) corresponding material response for damage-plasticity model with peak stress (a) P_{peak} =50.74 MPa, (b) P_{peak} =20 MPa and (c) P_{peak} =70 MPa.*

4.6.5 Tensile strength

4.6.5.1 Plasticity model

Since the concrete tensile strength, f_{ct} is a material property, any variation of this parameter will have an influence on the softening response of the cracked concrete. In this parametric study, the input values are changed one at a time. When reducing the tensile strength alone, the fracture energy remains constant only if the ultimate crack opening increases. The consequence of this is that a lower tensile strength, with preserved fracture energy, will yield a more ductile material and increase the number of load cycles required to develop a fully open crack, illustrated in Figure 4.25(b). Accordingly, a higher tensile strength yields a more brittle material, causing a spalling crack after fewer load cycles, see Figure 4.25(c). In reality a concrete with a lower tensile strength can, in fact, yield a more ductile material response. However, the

fracture energy also decrease with decreasing tensile strength, although the fracture energy does not decrease with the same rate.
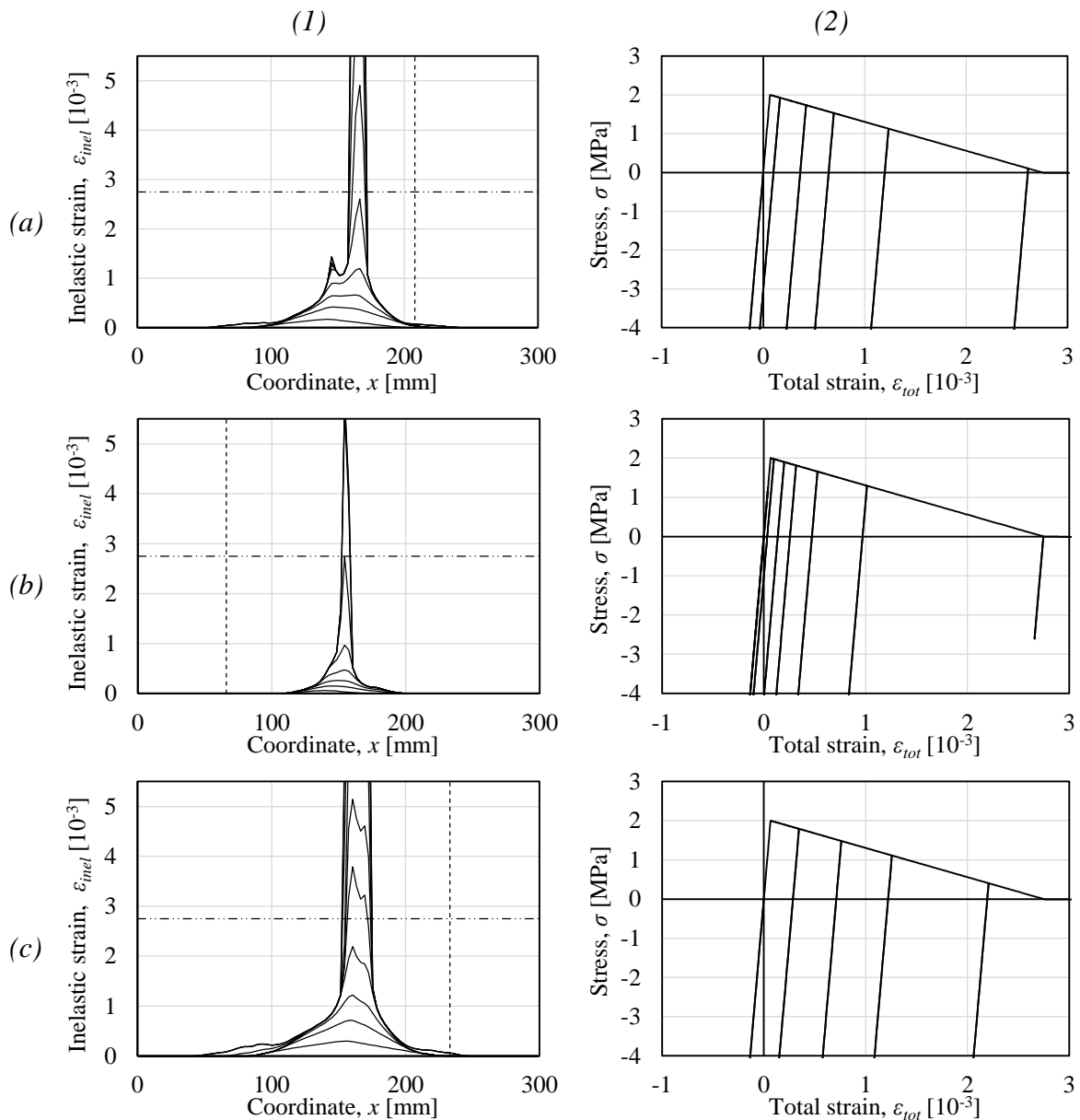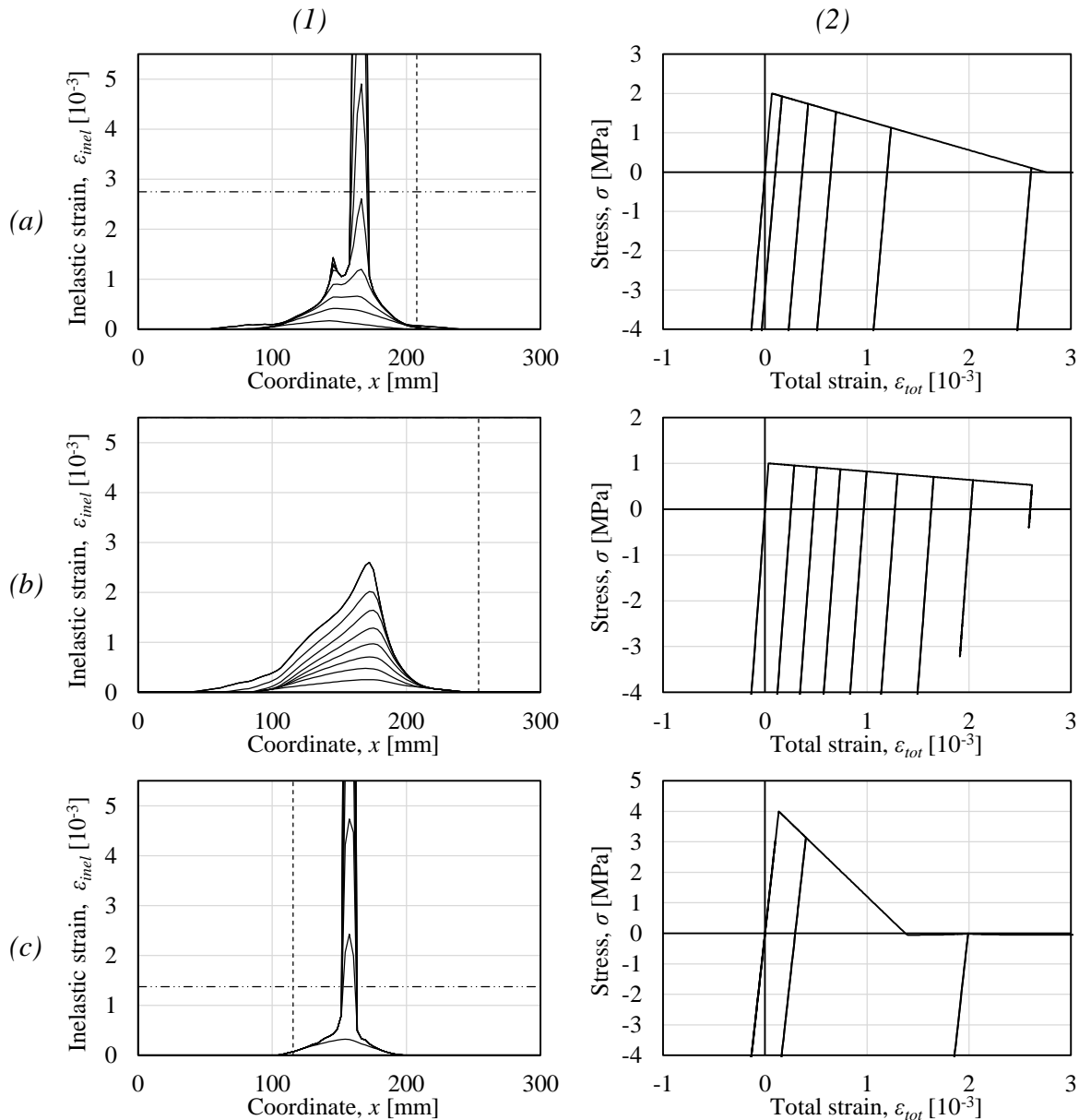

Figure 4.25 *(1) Distribution of inelastic strains and (2) corresponding material response for tensile strength (a) f_{ct} = 2 MPa, (b) f_{ct} = 1 MPa, and (c) f_{ct} = 4 MPa.*

4.6.5.2 Damage and damage-plasticity models

The same tendency, with more ductile material response as the tensile stress is reduced, can be seen for the damage and damage-plasticity models as well. This is expected, since the envelope curve in the stress-strain relation is the same for all three material models. However, there is a strain localisation decrease in the damage and damage-plasticity model due to instability in the pressure wave after the initial load cycle. The results of these models are presented in Appendix B4 and C4.

4.6.6　Number of elements

It was shown in Section 4.4.4 that the number of elements N used in the analyses influence the representation of the pressure wave. A denser mesh, i.e. a higher number of elements, more accurately represents the analytically presumed pressure wave. Therefore, the predicted spalling crack initiation according to McVay (1988), coincide well with the one achieved from the numerical analysis for a large number of elements, as can be seen in Table 4.9.

Table 4.9   *Comparison of crack initiation positions for increasing number of elements, N and predicted initiation by McVay (1988).*

Number of elements, N [-]	Crack initiation [mm]	McVay [mm]
50	99	92
100	97	92
200	96	92
400	94	92
800	93	92

An increase in the number of elements also cause a fully open crack to develop after fewer load cycles. Also, the distribution of strain localisation decrease with higher mesh density to the point where the strain will localise in one element, as can be seen in Figure 4.26(c) for $N = 400$. The fracture zone is kept at the reference value of 48 mm throughout the parametric study, and it could be argued that this is not reasonable when the inelastic strain related to the crack opening localize in one or a few elements only. In order for this fracture zone to be correct, the zone with inelastic strains has to be 48 mm. This concept is further discussed and compared in Section 4.9.
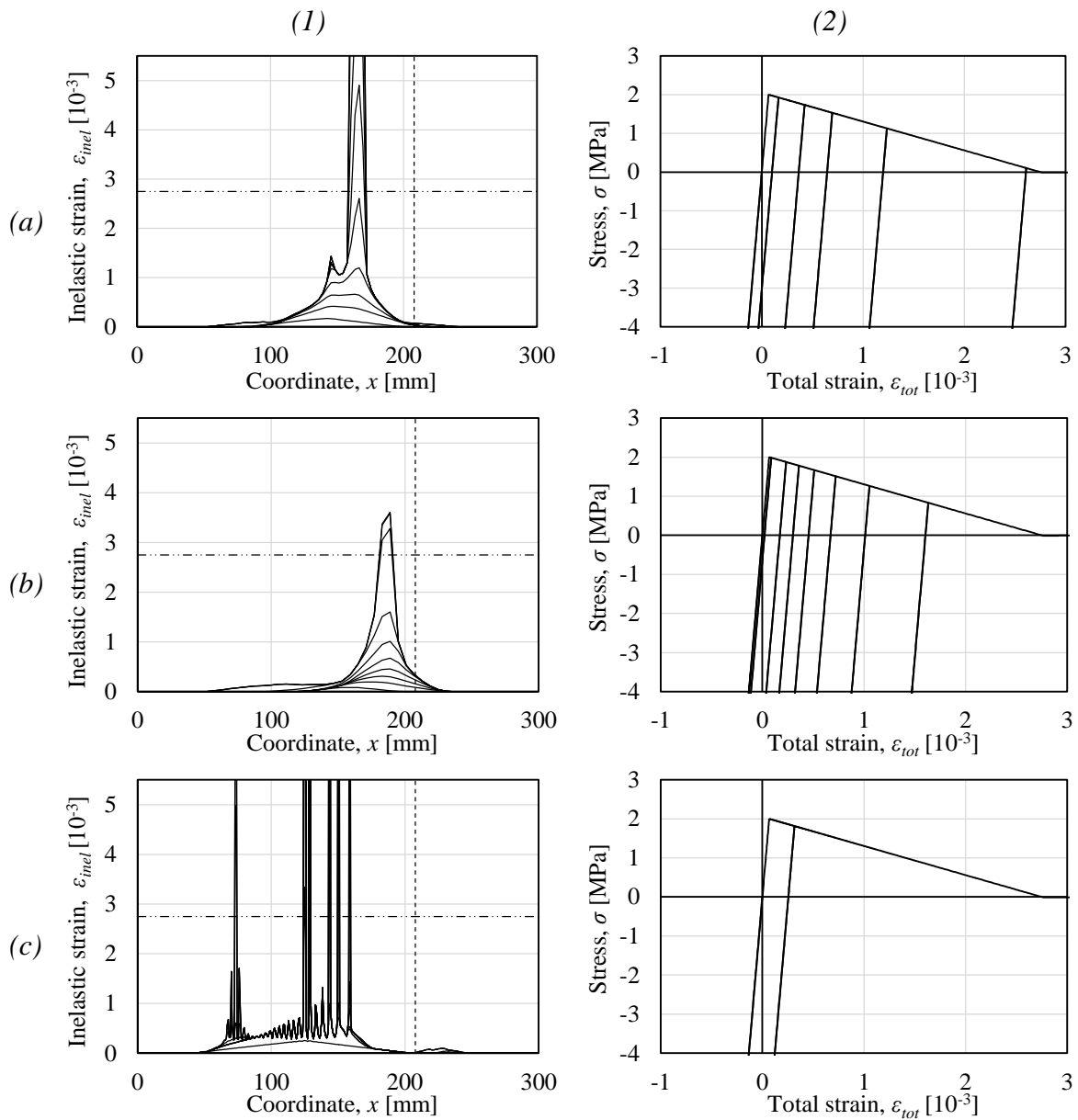
Figure 4.26   *(1) Distribution of inelastic strains and (2) corresponding material response for number of elements (a) N=100, (b) N=50 and (c) N=400.*

To conclude, although a higher mesh density converges to the presumed pressure wave, a problem with instability in the numerical analysis can be observed for increased number of elements if the fracture zone is kept constant. All results for the damage and damage-plasticity models, relating to number of elements can be found in Appendix B5 and C5.

4.6.7   Damping ratio

4.6.7.1   Plasticity model

The damping ratio, ξ is in the analysis used to determine the overall damping, C of the system using equations (4.11) and (4.12). The overall damping, C is then considered when the total energy loss of the system is determined for each time step. The reference values for the damping ratio are $\xi = \underline{1.4}$ for the plasticity model and $\xi = \underline{1.0}$

for damage and damage-plasticity models. The variations of the damping ratio considered in the parametric study are $\xi = [0.1, 0.3, 0.7, \underline{1.0} (\underline{1.4}), 3.0]$

As discussed in Section 4.4.3, a high damping ratio increase the discrepancy between the analytical and theoretical pressure waves. However, if the damping ratio is too low ($\xi < \sim 0.5$), oscillations occur in the pressure wave. These oscillations may result in tensile stresses in the structure as the pressure wave propagates in compression, as can be seen in Figure 4.7(2). If this is the case, the structure will be damaged in tension as the wave propagates in compression, which is theoretically unrealistic and the overall response becomes unstable. This is illustrated in Figure 4.27(b) where the cracked zone extends to the far left side in the structure.

For a damping ratio $\xi = 3.0$, the resulting response is presented in Figure 4.27(c). The increase in number of load cycles required to reach a fully developed crack can be explained by the discrepancy in the pressure wave i.e. the structure is unloaded earlier. Further, the time in which inelastic strain can develop decreases with increasing damping ratio, causing the crack to be barely fully opened.
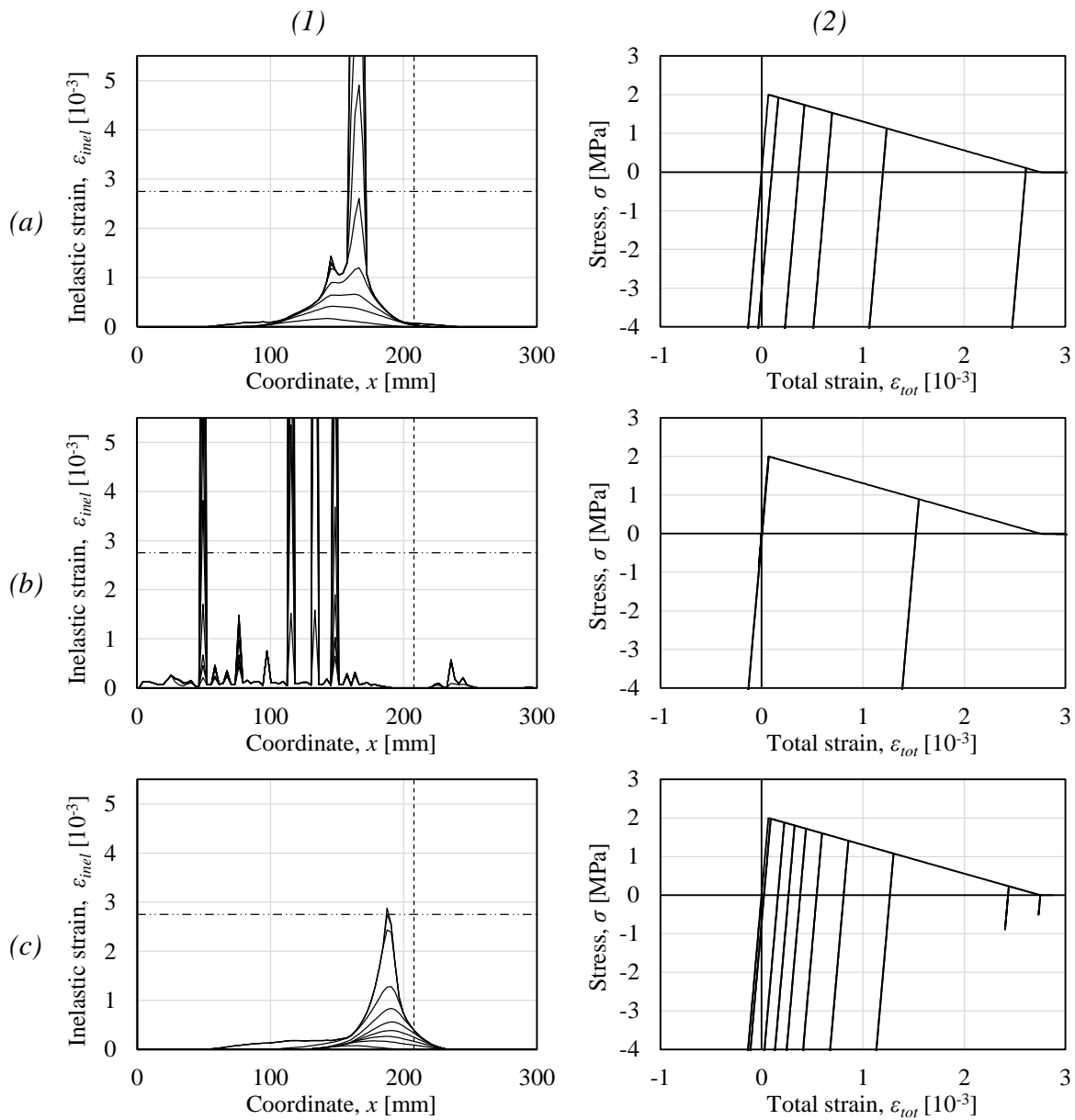
Figure 4.27 *(1) Distribution of inelastic strains and (2) corresponding material response for damping ratio (a) ξ = 1.4, (b) ξ = 0.1 and (c) ξ = 3.0.*

4.6.7.2 Damage and damage-plasticity models

For low damping ratios, the same unstable response can be observed for damage and damage-plasticity models. However, the damage-plasticity model shows an unstable behaviour even with the reference damping ratio value $\xi = 1.0$, forming a second crack at coordinate $x \approx 210$ mm, see Figure 4.28(a). In order to keep the pressure wave stable throughout the analysis, a high damping ratio is required ($\xi > \sim 2.0$). A conclusion from this is that the pressure wave in the damage-plasticity model is more inclined to be unstable than the plasticity model. All results relating to damping ratio for the three material models can be found in Appendix B6 and C6.
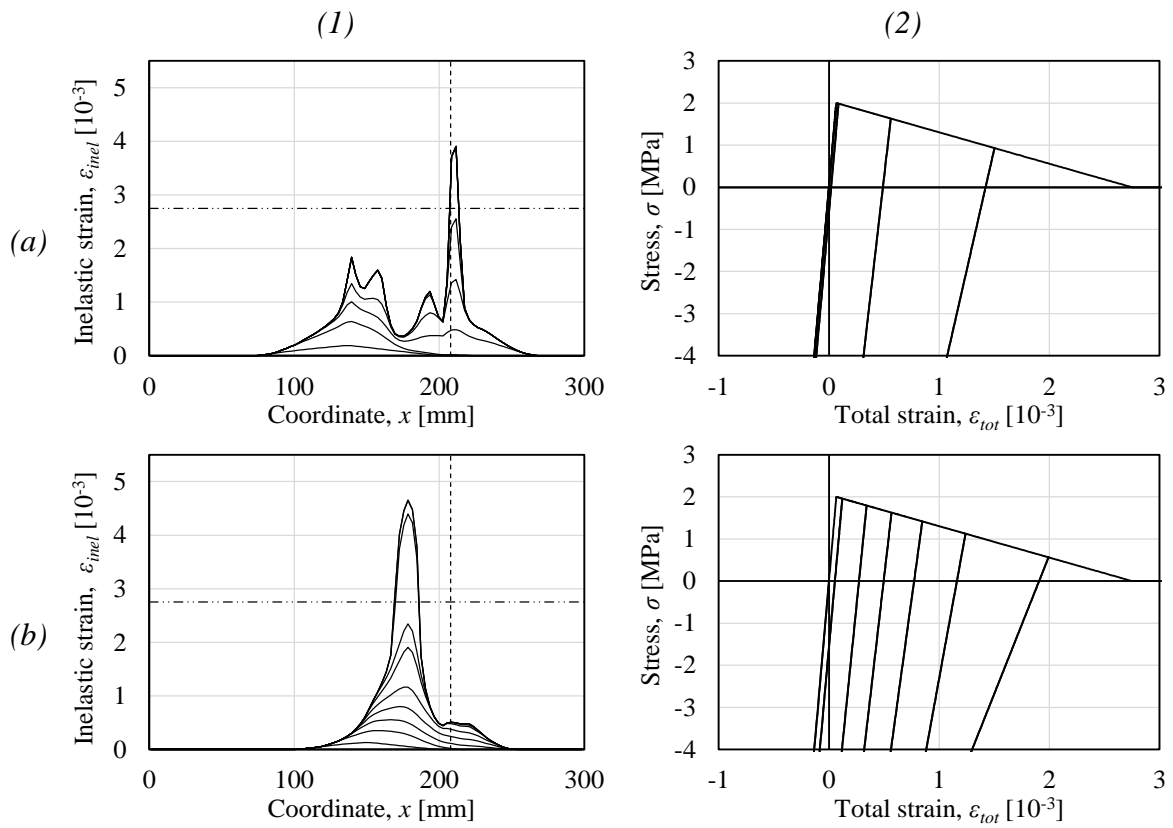
Figure 4.28 *(1) Distribution of inelastic strains and (2) corresponding material response for damage-plasticity model with damping ratio (a) ξ = 1.0 and (b) ξ = 2.0.*

4.7 Non-linear strain softening

4.7.1 Material response

The post peak behavior of concrete in tension has until this point been studied for a material with a linear strain softening curve. In reality, however, a more correct strain softening of concrete in tension is better described by a bi-linear or exponential decrease. For this reason, it is important to study and compare the structural behavior when including such response as well.

There are different approaches on how to consider bi-linear and non-linear strain softening in material models. One approach is to consistently use the same magnitude of the ultimate crack opening w_u throughout the different strain softening relations. However, this will lead to a large discrepancy in fracture energy G_f resulting in difficulties comparing the structural response.

Another approach is to consistently use the same fracture energy G_f for all different strain softening relations, resulting in different values of the ultimate crack opening w_u and, thus, ultimate strain ε_u, see Figure 4.29. For the comparison in this section, the fracture energy is set to the same magnitude as used in the analysis by Ekström, i.e. $G_f = 132$ N/m. This fracture energy is then kept constant also when using the bi-linear and exponential strain softening curves.

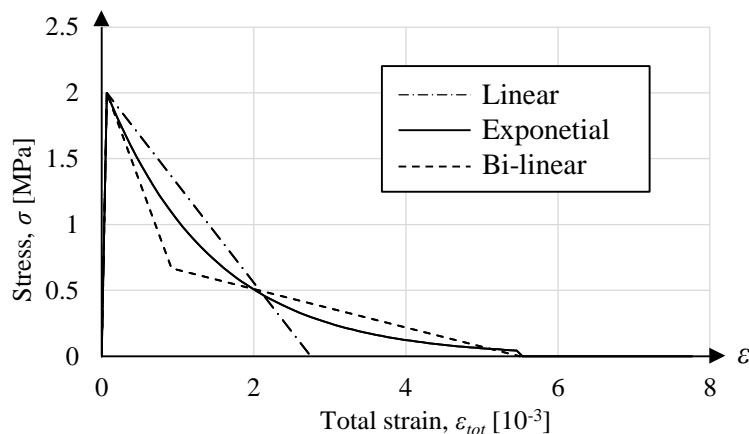*Figure 4.29   Illustration of linear, bi-linear and exponential strain softening using the same fracture energy G_f.*

Based on Johansson (2000), a reasonable bi-linear strain softening relation to consider for concrete in tension is given in Figure 4.30. By adjusting the value of the ultimate crack opening w_u, it is possible to achieve a strain softening which corresponds to fracture energy $G_f = 132$ N/m.

$$f_{ct} = 2\,\text{MPa}$$

$$f_{ct,1} = \frac{f_{ct}}{3}$$

$$w_u = 0.26\,\text{mm}$$

$$w_1 = \frac{w_u}{6}$$
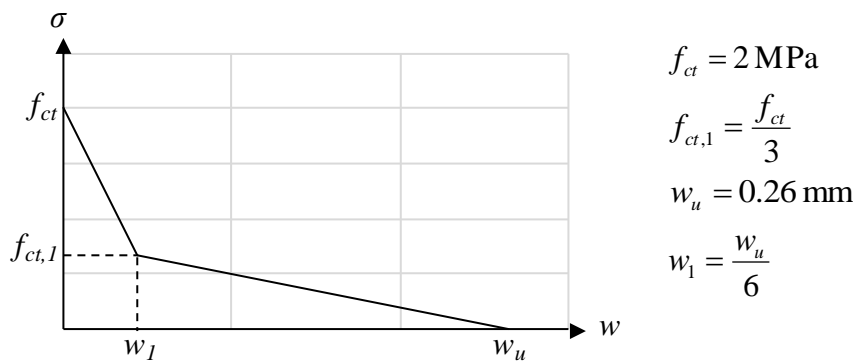
Figure 4.30   Illustration of bi-linear σ-w relation with corresponding input to achieve G$_f$ = 132 N/m.

Regarding the exponential strain softening, it can be described using equation (4.16) as stress-crack opening relation,

$$\sigma(w) = f_{ct} \cdot e^{-A \cdot w} \tag{4.16}$$

where *A* is a constant describing the shape of the curve. By adjusting the ultimate crack opening w_u and the coefficient *A*, it is possible to achieve the same fracture energy over different $\sigma(w)$ relations, see Figure 4.31.

$$f_{ct} = 2\,\text{MPa}$$

$$A = 677\,\text{mm}^{-1}$$

$$w_u = 0.26\,\text{mm}$$
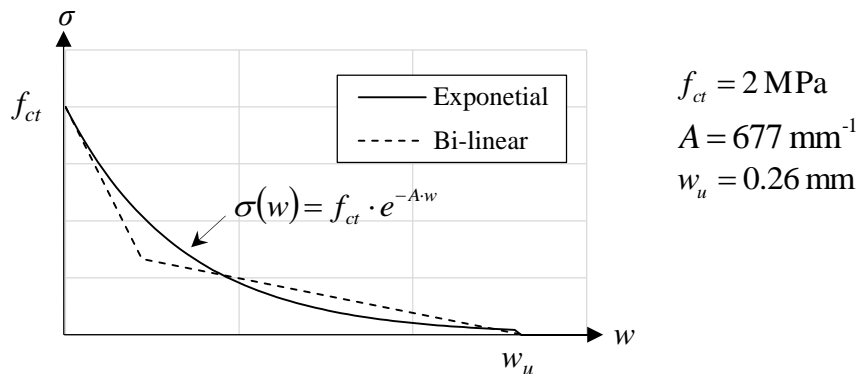
Figure 4.31   Conceptual illustration of exponential σ-w relation with corresponding coefficient A, and ultimate crack opening w$_u$ to maintain constant fracture energy.

From both the bi-linear and the exponential strain softening curve it becomes clear that the magnitude of the ultimate crack opening w_u, and thus the ultimate strain ε_u, increases as the strain softening becomes non-linear. Also seen in Figure 4.31 is that the exponential curve is chosen to resemble the bi-linear curve as good as possible, and that the ultimate crack opening w_u is set to the same as for the bi-linear relation in Figure 4.30.

4.7.2 Plasticity model

By implementing both the bi-linear and the exponential strain softening curves for the plasticity model, the structural response is found to be very similar to the response for the linear strain softening curve. This is illustrated in Figure 4.32, where the conclusion is that the spalling crack appears at about the same location for all three different strain softening curves. Further, for both bi-linear and the exponential strain softening, the number of load cycles it takes for the strain to localize decreases.

Figure 4.32 *(1) Distribution of inelastic strains and (2) corresponding material response for a plasticity model using (a) linear, (b) bi-linear and (c) exponential strain softening.*

Further, Table 4.10 summarizes the structural response for a plasticity model with different strain softening curves.

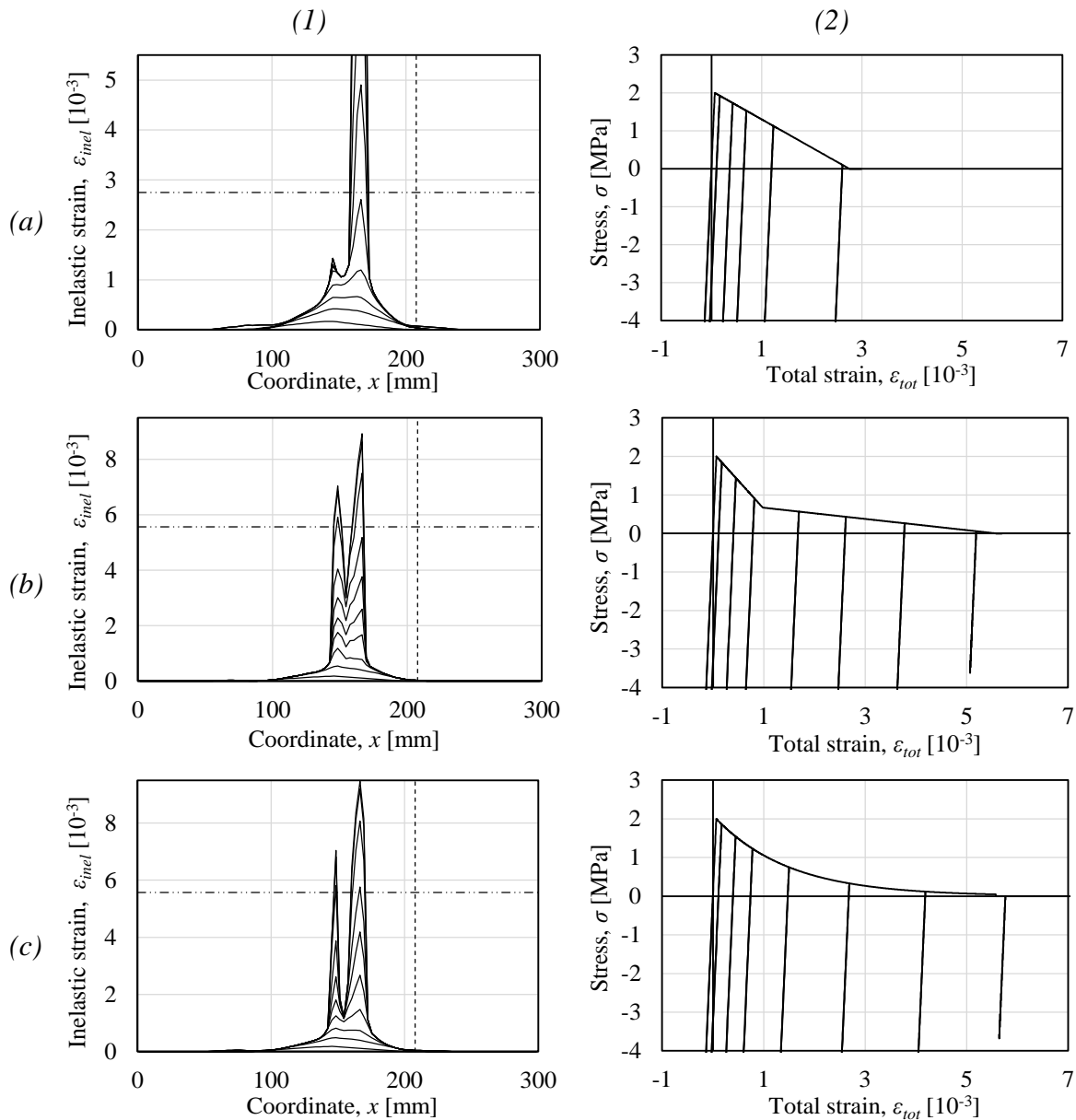*Table 4.10   Crack initiation and final spalling crack, defined from the right side for a plasticity model considering different strain softening relations.*

Strain softening	Crack initiation [mm]	Spalling crack [mm]
Linear	97	140
Bi-linear	97	140
Exponential	97	140

4.7.3   Damage model

The structural response when implementing bi-linear and exponential strain for a damage model is, like for the plasticity model, very similar to using a linear strain softening curve. Neither the bi-linear nor the exponential strain softening curve yield a structural response much different from the one when using a linear strain softening curve. None of the model predicts a fully developed spalling crack, which is shown in Figure 4.33. As for the plasticity model, Table 4.11 summarizes the location of crack initiation and spalling crack for a damage model.

Table 4.11   Crack initiation and final spalling crack, defined from the right side for a damage model considering different strain softening relations.

Strain softening	Crack initiation [mm]	Spalling crack [mm]
Linear	97	No spalling crack
Bi-linear	97	No spalling crack
Exponential	97	No spalling crack

Figure 4.33   *(1) Distribution of inelastic strains and (2) corresponding material response for a damage model using (a) linear, (b) bi-linear and (c) exponential strain softening.*

4.7.4   Damage-plasticity model

An important observation from both Section 4.7.2 and 4.7.3 is that a bi-linear strain softening curve approximates an exponential very well, i.e. there is no noticeable difference in the structural response when using a bi-linear instead of an exponential relation. For this reason, the damage-plasticity model with linear strain softening is only compared to a model with bi-linear strain softening. The results of this comparison is shown in Figure 4.34, and shows that the location of the final spalling crack is different between the two different models. The reason for this seems to be that using a bi-linear strain softening, instead of a linear, results in earlier crack localisation.
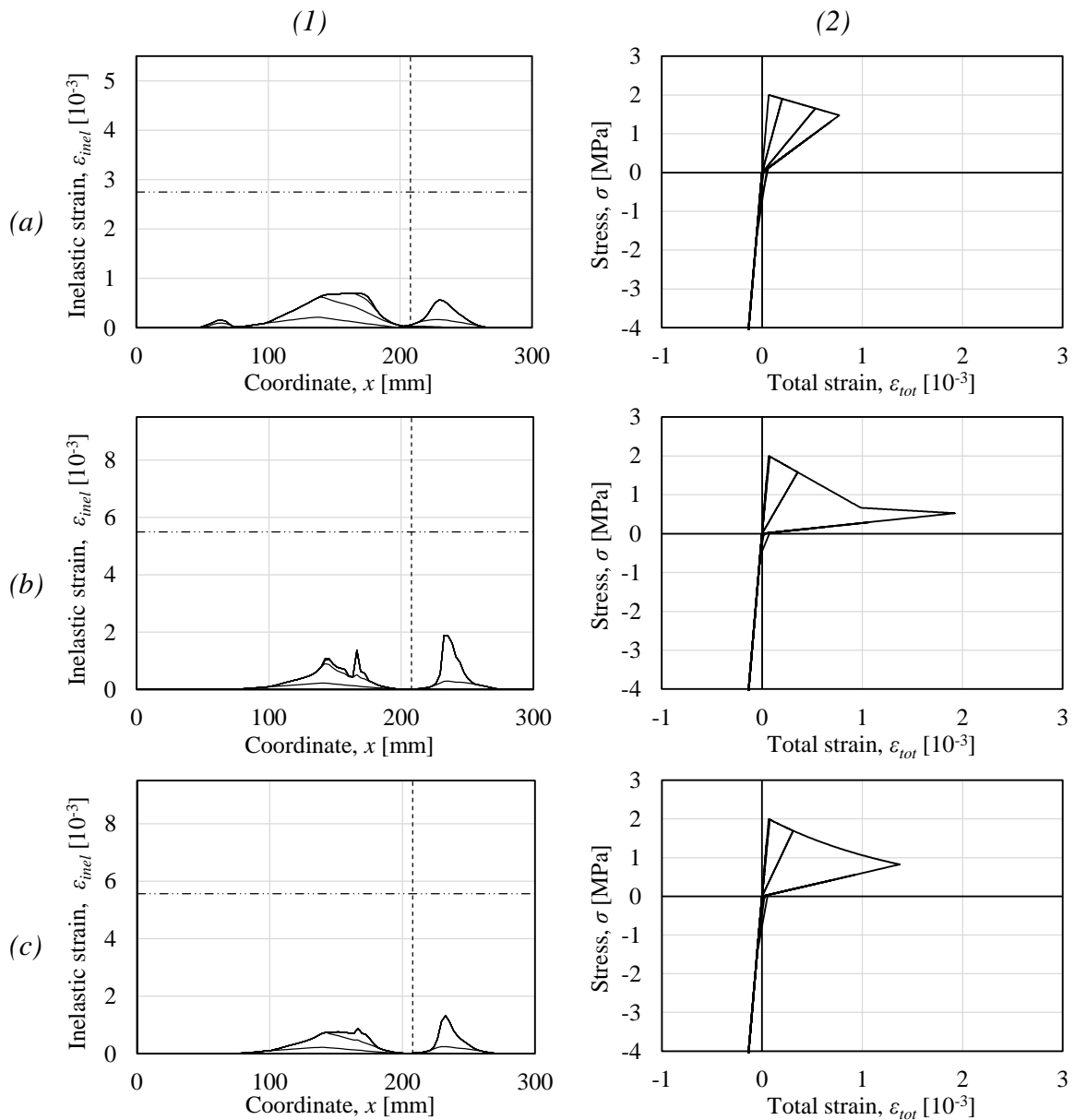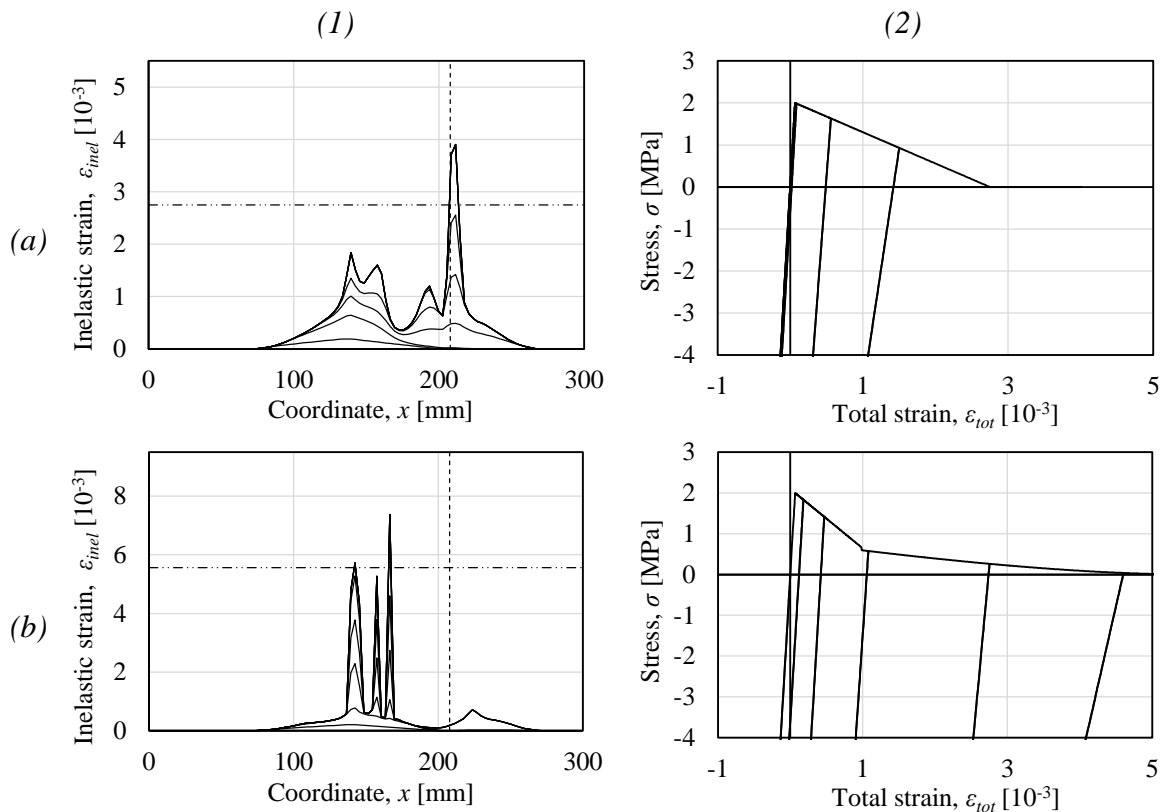
Figure 4.34 (1) Distribution of inelastic strains and (2) corresponding material response for a damage-plasticity model using (a) linear and (b) bi-linear strain softening.

Further, Table 4.12 summarizes crack initiation and final spalling crack for the two different strain softening relations.

Table 4.12 Crack initiation and final spalling crack, defined from the right side for a damage-plasticity model considering different strain softening relations.

Strain softening	Crack initiation [mm]	Spalling crack [mm]
Linear	97	90
Bi-linear	97	140

4.8   Non-linear pressure-time relation

All results presented until this section has considered a pressure wave with linear pressure decrease, which in analogy with Section 2.1.1 is a simplification since the pressure wave in reality has an exponential decrease. Therefore, this section aims to investigate the structural response when the load is non-linear. The effect on this is studied with three different configurations of pressure-time relation and crack softening, illustrated in Figure 4.35.
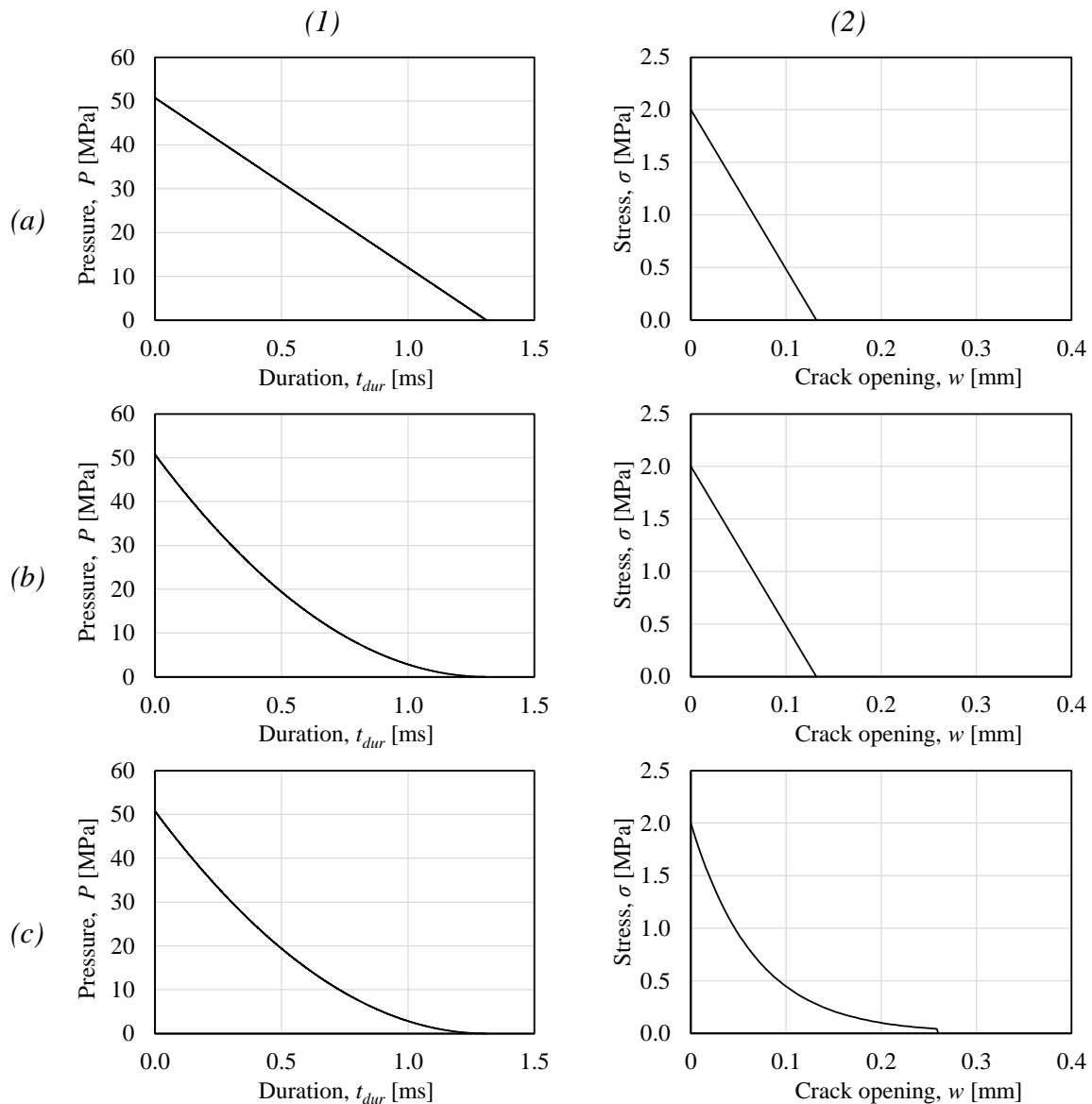
Figure 4.35 (1) Pressure-time relation and (2) crack softening for different configurations used to study the effect of non-linear pressure wave decrease.

The reason why the configuration shown in Figure 4.35(a) is included is because it will be used to study the influence and compare the structural response when a non-linear pressure-time relation is included in the analysis. To illustrate the results of such analysis, a plasticity model is used for which the results are illustrated in Figure 4.36. The conclusion of these results is that including a non-linear pressure time gradient only will influence the location of crack initiation as well as the number load cycles needed before the ultimate strain is reached. According to this comparison, though, non-linear pressure time gradient will not influence the location of the spalling crack significantly.
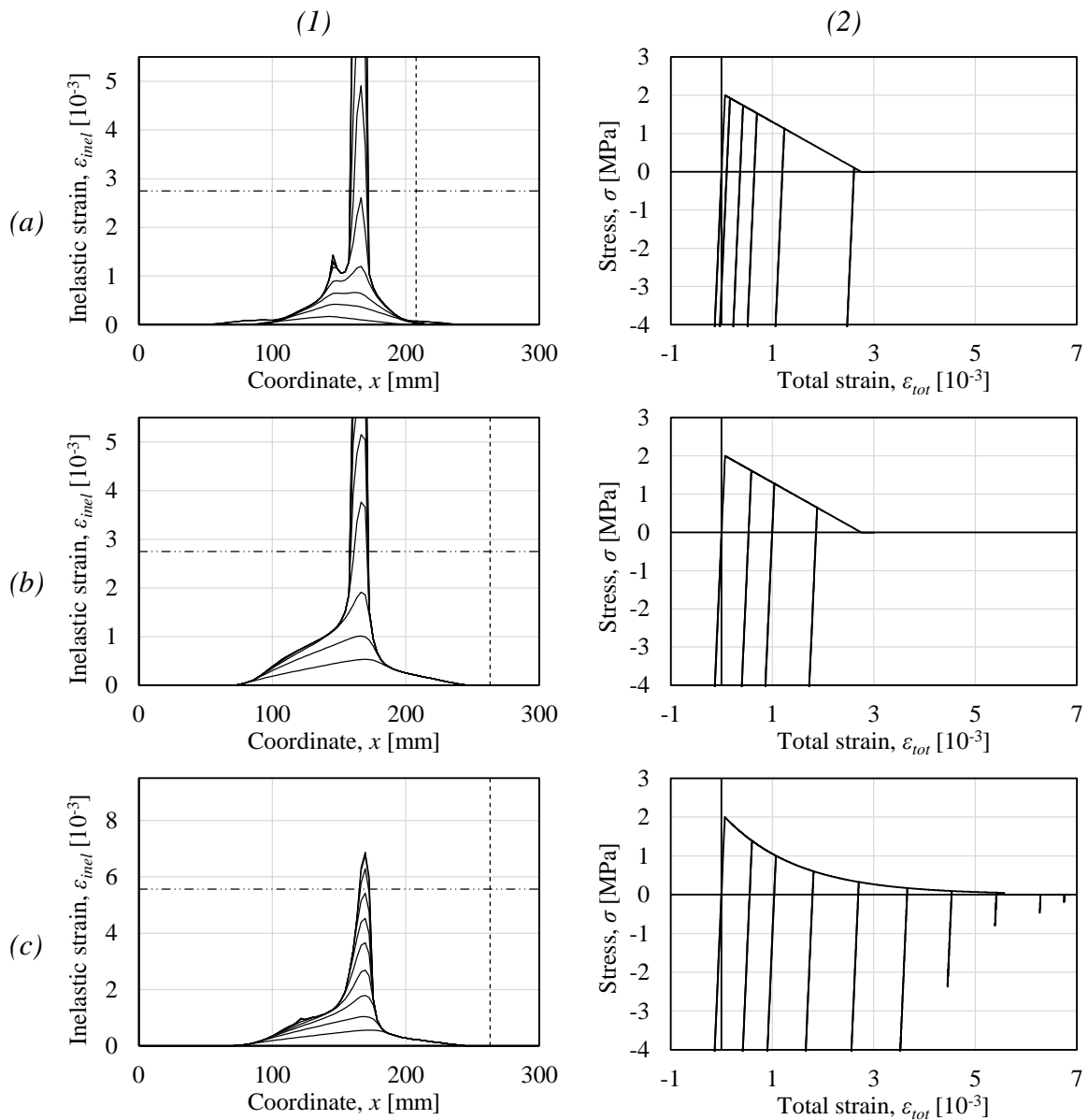
Figure 4.36 *(1) Distribution of inelastic strains and (2) corresponding material response for (a) linear crack softening and linear pressure time relation, (b) linear crack softening and non-linear pressure time relation and (c) non-linear crack softening and non-linear pressure time relation.*

Further, as mentioned in Section 4.7, when using exponential crack softening it is important to determine the ultimate strain beforehand, since it becomes infinite without such limitations. This is why the ultimate strain in Figure 4.36(c) becomes larger compared with the ultimate strain when using linear strain softening. A summary of the results from this analysis is given in Table 4.13.

Table 4.13   Crack initiation and final spalling crack for different configurations of pressure time relation and crack softening. Comparison with analytically predicted crack initiation according to McVay.

Pressure-time	Crack softening	Crack initiation [mm]	Spalling crack [mm]
Linear	Linear	97 (McVay 92)	140
Non-linear	Linear	52 (McVay 37)	140
Non-linear	Non-linear	52 (McVay 37)	140

It is reasonable that the location of crack initiation changes as the pressure time gradient changes. Since a non-linear pressure time gradient is higher, compared with a linear, at the blast wave front it will reach the tensile strength earlier after reflection. However, the interesting observation in this section is that the location of the final spalling crack does not change.

4.9   Fracture zone and fracture energy

The parametric study presented in Section 4.6 is performed without consideration to the resulting fracture zone and fracture energy, i.e. in all results presented the fracture zone and fracture energy is kept at the values used by Ekström. However, since the post peak behavior of concrete in tension is a function of crack opening w, rather than strain ε, it becomes a much more complicated subject to treat in the analysis. For this reason, this section aims to describe the principle of how the fracture zone and the fracture energy will influence the structural response in the analysis.

The results presented in this thesis are all based on distribution of inelastic strains in the structure. These strains are, however, in reality crack openings distributed over a certain distance, also known as the crack band width or fracture zone. The magnitude of this distance is determined beforehand together with the fracture energy, which means that the response in the fracture zone is assumed before the results are known. Hence, the assumption is that the fracture energy G_f is to dissipate over a distance l_{frac}. Therefore, the results need to be compared with the assumption in order for the results to be considered as reliable. If the distribution of inelastic strains exceeds the crack band width the model would represent more than one crack, alternatively the crack is more ductile than assumed. In contrary, if the distribution of inelastic strains is lower than the anticipated crack band width, the model would represent a more brittle material than assumed.

To further describe this concept, the result from the plasticity model presented in Section 4.6.2 is used. Figure 4.37 illustrates the discrepancy in the fracture zone l_{frac} for different values of inelastic strains ε_{inel}. Further, Figure 4.37 shows that for small strain values the fracture zone is larger than assumed, and smaller than assumed for larger strain values. This is illustrated by studying the strain distribution zone after one load cycle versus after six load cycles, compare $l_{frac,1}$ and $l_{frac,2}$. The consequence of this is that it becomes difficult to determine whether the assumed fracture zone is correct.
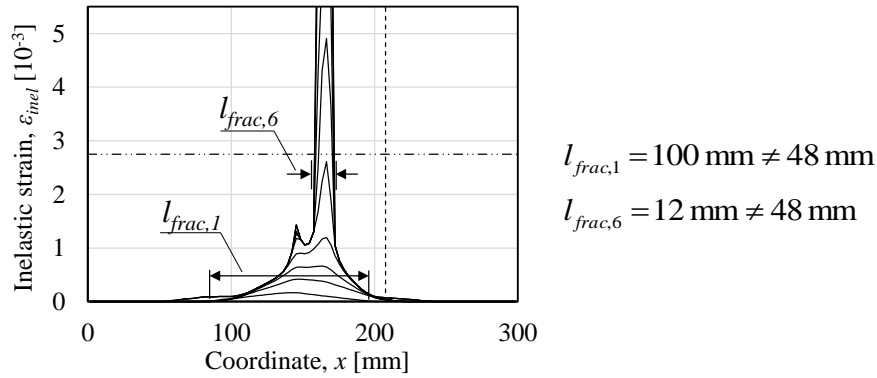
Figure 4.37   Illustration of the inconsistency in fracture zone l_{frac} for varying values of inelastic strains ε_{inel}.

A possible approach to determine whether the assumed fracture energy G_f corresponds to the actual dissipated energy in the analysis is to convert the distribution of inelastic strains to dissipated energy. This approach would be simple if the fracture zone is constant, since the fracture energy then would correspond to the area under the graph in Figure 4.37. However, with varying length l_{frac} of the fracture zone this principle becomes more complicated. The strategy is therefore to subdivide the distribution of inelastic strains in to segments with varying fracture zone, and based on the strain increment and current fracture zone determine the dissipated energy. By doing this for every strain value until the ultimate strain is reached, the total energy is determined. This principle is illustrated in Figure 4.38, which shows a subdivision with i different intervals.
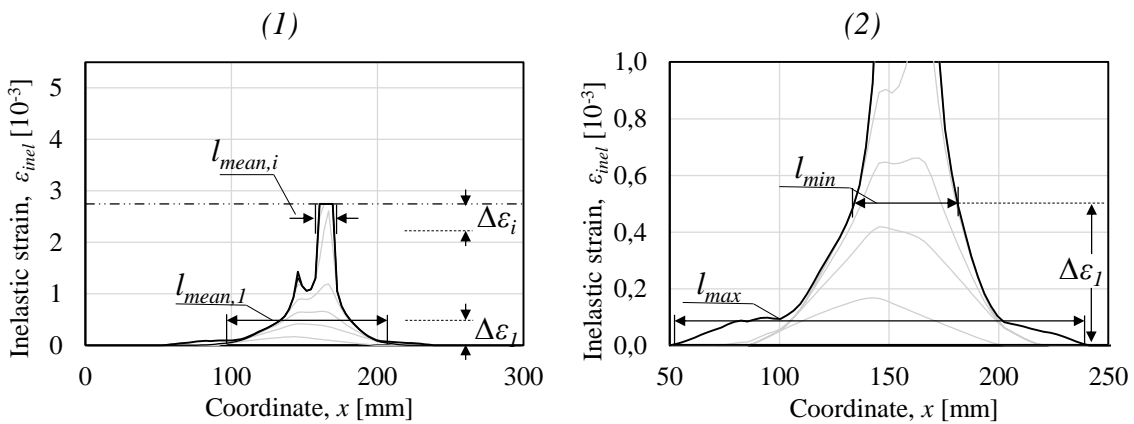

Figure 4.38   (1) Conceptual illustration of subdividing inelastic strains to determine dissipated energy and (2) magnified view to illustrate how to determine l_{mean} for each subdivision.

For each subdivision, the increase in crack opening w is determined with equation (4.17).

$$\Delta w = l_{mean} \cdot \Delta \varepsilon \tag{4.17}$$

where

$$l_{mean} = \frac{l_{max} + l_{min}}{2} \tag{4.18}$$

Since the energy corresponds to the area under the σ-w graph, the mean stress for each subdivision needs to be determined as well. For each strain increment, this stress value is determined using the constitutive model for concrete in tension, see Figure 4.39.
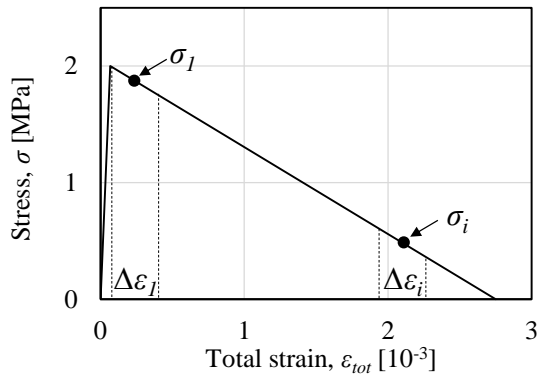

Figure 4.39   Illustration of how mean stress values are determined for each strain interval.

Knowing both the mean stress value and the increase in crack opening, the total dissipated energy is determined in accordance with equation (4.19).

$$G_{f,calc} = \sum_{i=1}^{n} \sigma_i \cdot \Delta w_i \tag{4.19}$$

If there is a large discrepancy in the calculated fracture energy and the fracture energy given as input in the analysis, it is reasonable to make adjustments in the numerical input to reflect the results more accurately. Further, since the inelastic strains distribute over different crack band widths for different strain values there will be a discrepancy in the assumed and the calculated stress-crack opening relation.

This method on how to compare the numerical input with the results can be used to make adjustments in the numerical input. For example, consider a case where the calculated fracture energy exceeds the anticipated. Based on the anticipated fracture energy and the calculated, it is possible to define a factor α_{error} which defines the fraction between the anticipated fracture energy and the calculated, see equation (4.20). This factor can then be used to adjust the fracture zone iteratively. Such an iteration is summarized in Table 4.14 for the results presented by Ekström for a plasticity model.

$$\alpha_{error} = \frac{G_{f,calc}}{G_{f,input}} \tag{4.20}$$

Table 4.14   *Numerical iteration to determine and compare the calculated fracture energy with the anticipated, and adjustments of the fracture zone.*

Iteration	$G_{f,input}$	$G_{f,calc}$	α_{error}	$l_{frac,input}$	$l_{frac,mod} = \alpha_{error} \cdot l_{frac,input}$
1	132.0	122.2	0.926	48.00	44.44
2	132.0	128.4	0.973	44.44	43.22
3	132.0	130.9	0.991	43.22	42.87
4	132.0	131.7	0.997	42.87	42.77

As seen in Table 4.14, the calculated fracture energy $G_{f,calc}$ converges towards the anticipated as iterative adjustments are made to the fracture zone. For this specific case, where Ekström assumes a fracture zone of 48 mm there is no substantial change in the fracture zone as adjustments are made. However, the principle of this is important to highlight. Further, the structural response when applying adjustments on the fracture zone are seen in Figure 4.40, to which the conclusion is that the structural response is more or less the same. The only noticeable difference is that the magnitude of the ultimate strain increases as the fracture zone decreases, i.e. the model reflects a more ductile material.
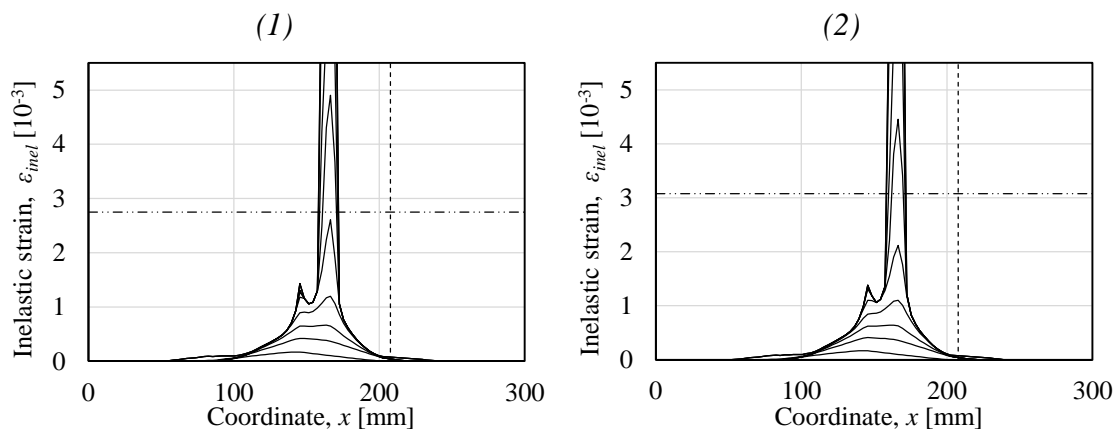
Figure 4.40   *Distribution of inelastic strains for (1) fracture zone by Ekström and (2) adjusted fracture zone.*

Further observations regarding the fracture zone and fracture energy is that when inelastic strains distribute over inconsistent crack band widths, there is a substantial discrepancy in the anticipated σ-w relation and the calculated σ-w relation. By using the last iteration presented in Table 4.14 and illustrate how the stress relates to the crack opening, one may compare the assumed σ-w relation with the numerical. This comparison is shown in Figure 4.41, where the dashed line corresponds to the assumed σ-w relation and the solid line corresponds to the calculated σ-w relation based on the results.

Figure 4.41   Comparison between predicted σ-w relation (dashed line) and calculated σ-w relation (solid line). Illustration of where the actual crack band width is larger and smaller than assumed.

4.9.1   Examples of fracture zone adjustments

4.9.1.1   Overview

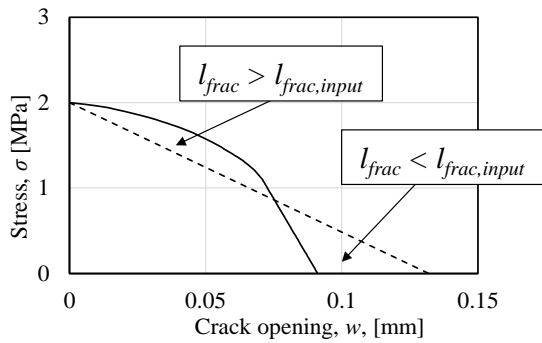Although the example presented in Section 4.9 only resulted in minor adjustments in the fracture zone, i.e. from 48 mm to 43 mm, the principle of how to evaluate and study the fracture energy and fracture zone is of importance. By once again studying the results presented in the parametric study in Section 4.6, it becomes obvious that adjustments in fracture zone is required in almost every presented result. Therefore, the proposal in this thesis is that such adjustments are needed in order for the model to be reliable. This section will present two examples which confirms the theory that adjustments of the fracture zone might have large influence on the structural response. These examples are taken from Section 4.6.2, where a plasticity model is considered for different load durations. The first example is when the load is short with a duration of $t_{dur} = 0.131$ ms and the second example is when the load is long with duration $t_{dur} = 1.965$ ms.

4.9.1.2   Short load duration, fracture zone adjustment

When the load duration is decreased to a tenth of the original value, the structural response changes drastically. This is described in Section 4.6.2, but also illustrated in Figure 4.42 where the conclusion is that the assumption of a fracture zone of 48 mm becomes inaccurate, see Figure 4.42(2).
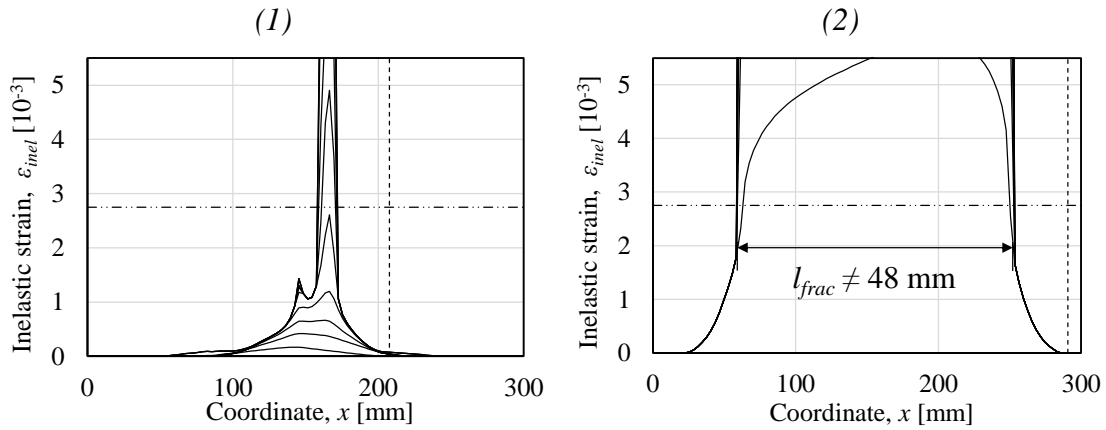
Figure 4.42   Comparison between structural response in terms of distribution of inelastic strains for load duration (1) t_{dur} = 1.31 ms and (2) t_{dur} = 0.131 ms.

For this reason, iteratively adjustments of the fracture zone is needed when the load duration is decreased to t_{dur} = 0.131 ms. Using the principle presented in Section 4.9, the iterative process is summarized in Table 4.15.

Table 4.15   Numerical iteration to determine and compare the calculated fracture energy with the anticipated, and adjustments of the fracture zone.

Iteration	$G_{f,input}$	$G_{f,calc}$	α_{error}	$l_{frac,input}$	$l_{frac,\mathrm{mod}} = \alpha_{error} \cdot l_{frac,input}$
1	132.0	596.9	4.520	48.00	217.1
2	132.0	147.1	1.110	217.1	241.9
3	132.0	132.7	1.004	241.9	243.1
4	132.0	132.0	1.000	243.1	243.1

Further, Table 4.15 shows that the adjustment in fracture zone converges rather fast towards approximately l_{frac} = 243 mm which corresponds well to the distribution of inelastic strains seen in Figure 4.42(2). Changing the fracture zone corresponding to the forth iteration in Table 4.15 results in a distribution of inelastic strains seen in Figure 4.43(2). Although the overall structural response does not change that much, the ultimate strain, i.e. the strain level indicating fully opened crack, decreases drastically as the fracture zone increases.
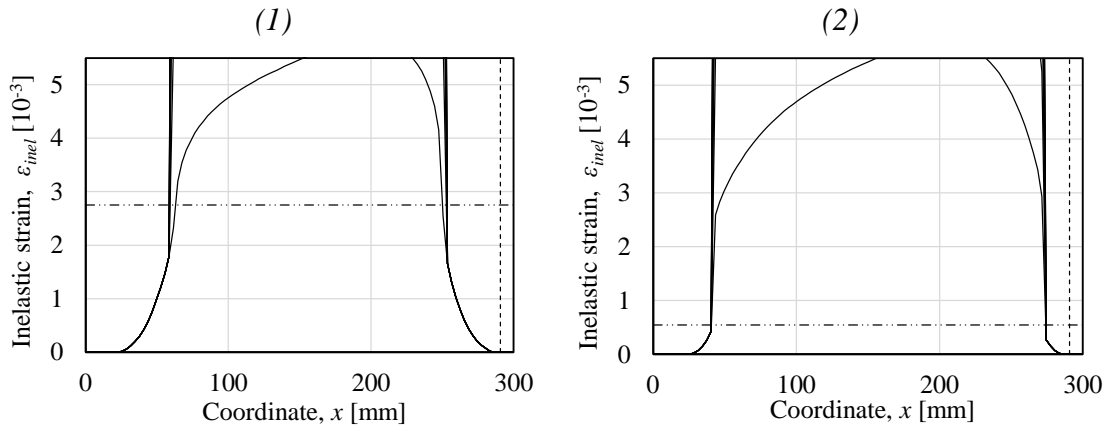
Figure 4.43   Distribution of inelastic strains for load duration t_{dur}=0.131 ms for (1) fracture zone by Ekström and (2) adjusted fracture zone.

In addition to comparing the structural response in terms of distribution of inelastic strains, the predicted σ-w relation can be compared with the numerical σ-w relation in analogy with Figure 4.41. Since the fracture zone is more consistent over different strain values, compared with the case shown in Figure 4.42(1), the expectation is that the anticipated σ-w relation and the calculated σ-w relation will resemble each other quite well. This is also confirmed by studying Figure 4.44.
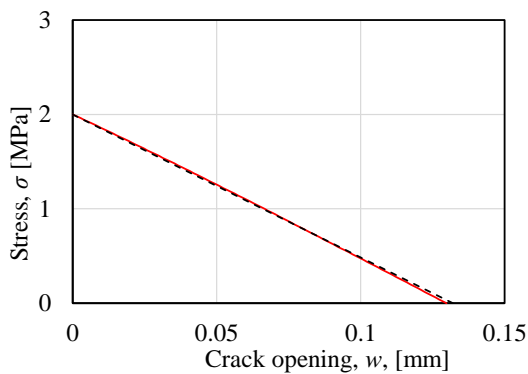
Figure 4.44   Comparison between predicted σ-w relation (dashed line) and calculated σ-w relation (solid red line).

4.9.1.3   Long load duration, fracture zone adjustment

Although there is no drastic change in structural response in terms of inelastic strains when increasing the load duration from t_{dur} = 1.31 ms to t_{dur} = 1.965 ms, the principle of how to adjust the fracture zone is explained for such a case as well. Without adjustments to the fracture zone, the structural response is illustrated in Figure 4.45 for the different load durations.
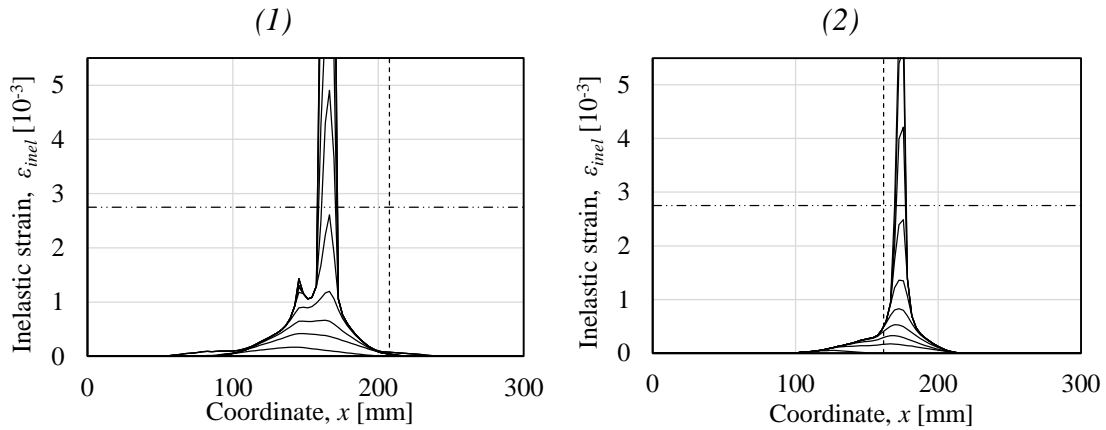
Figure 4.45   Comparison between structural response in terms of distribution of inelastic strains for load duration (1) t_{dur} = 1.31 ms and (2) t_{dur} = 1.965 ms.

Since the distribution of inelastic strains is over a smaller region, the prediction is that the fracture zone should be chosen smaller than 48 mm. The iterative adjustment of the fracture zone is summarized in Table 4.16.

Table 4.16   Numerical iteration to determine and compare the calculated fracture energy with the anticipated, and adjustments of the fracture zone.

Iteration	$G_{f,input}$	$G_{f,calc}$	α_{error}	$l_{frac,input}$	$l_{frac,mod} = \alpha_{error} \cdot l_{frac,input}$
1	132.0	71.20	0.539	48.00	25.90
2	132.0	109.6	0.830	25.90	21.51
3	132.0	113.3	0.858	21.51	18.45
4	132.0	114.8	0.869	18.45	16.05

As seen by Table 4.16, the iterations does not converge after four iterations. The reason for this can be seen by studying the structural response in terms of inelastic strains when the adjustment is made. Upon adjusting the fracture zone in accordance with the iterations in Table 4.16, the magnitude of the ultimate strain increases in such way that no spalling crack is expected. This is illustrated in Figure 4.46 where the distribution of inelastic strains are compared without and with adjustments of the fracture zone.
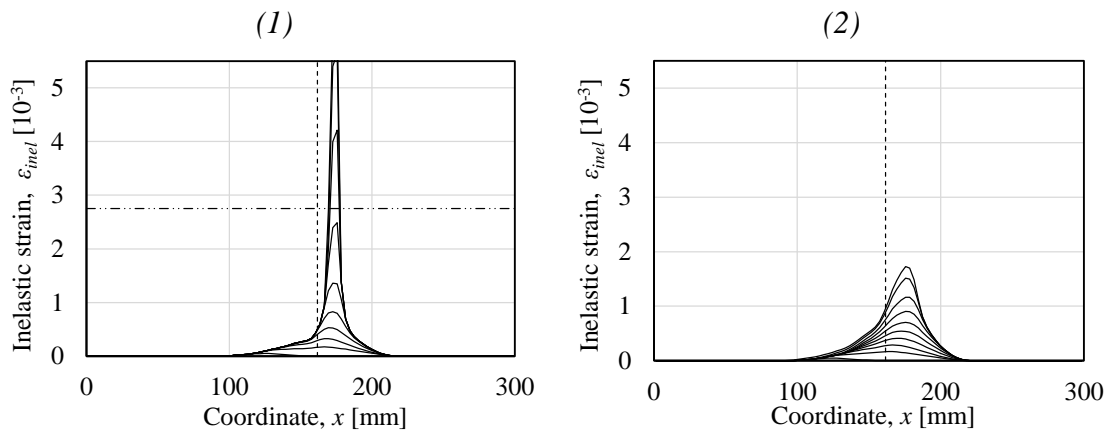
Figure 4.46 Distribution of inelastic strains for load duration t_{dur} = 1.965 ms for (1) fracture zone by Ekström and (2) adjusted fracture zone.

An additional illustration that shows that no spalling crack is expected after adjusting the length of the fracture zone is to study the σ-w relation and compare it with the assumed σ-w relation. This is illustrated in Figure 4.47 which shows a large discrepancy in predicted and calculated behaviour.
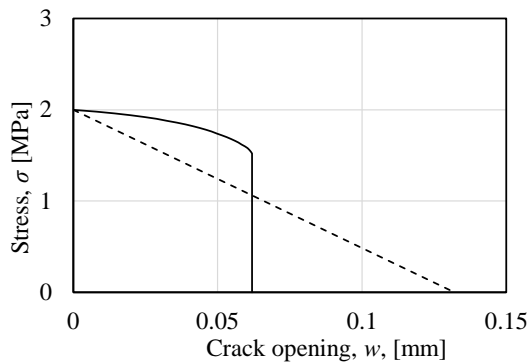

Figure 4.47 Comparison between predicted σ-w relation (dashed line) and calculated σ-w relation (solid line).

The different behaviour after changing the fracture zone highlights the importance of this aspect. If one were to study the results without adjusting the fracture zone, see Figure 4.46(1), a spalling crack is expected. However, by adjusting the fracture zone one would conclude that no spalling crack takes place.

4.10 Observations on how inelastic strains develop

4.10.1 Overview

The results in the parametric study in Section 4.6 are all based on how inelastic strains distribute within a structure. The principle of how these strains develop during cyclic loading/unloading was presented in Section 4.5. This principle is in agreement with how Ekström reason that the spalling procedure takes place, i.e. a fully developed spalling crack is not developed instantaneously nor in the location of crack initiation. This section aims to further describe this procedure based on observations made during the parametric study.

These observations are centred around the structural response after one load cycle, i.e. for the time of crack initiation and corresponding distribution of inelastic strains. The

model used to explain these observations is the reference plasticity model. The distribution of inelastic strains after one load cycle for this model is illustrated in Figure 4.48. The key discussion regarding this strain distribution is mainly based on two observations;

- Why do inelastic strains not develop all the way to the far left in the structure after the first load cycle?
- What is the main reason that strains develop successively a certain distance from the coordinate of crack initiation?

These two questions can also be described with the illustrations in Figure 4.48, where it can be concluded that inelastic strains are distributed approximately between coordinates $x \approx 85$ mm and $x \approx 200$ mm, and is mostly developed at coordinate $x \approx 145$ mm.
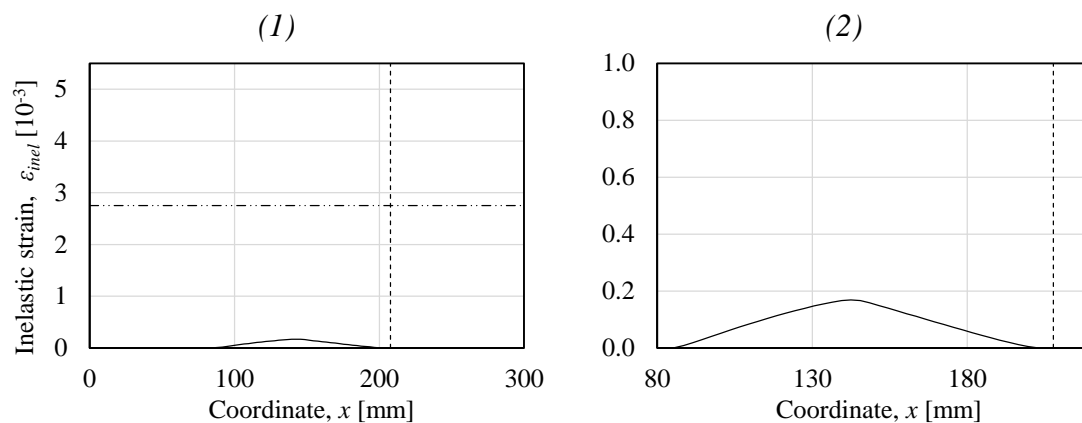

Figure 4.48   *(1) Distribtuion of inelastic strains after one load cycle for the reference model presented by Ekström (Plasticity) and (2) magnified view.*

4.10.2 Lack of inelastic strains at left side of the structure

The reason that inelastic strains are not developed all the way to the far left in the structure is ascribed to the discrepancy in shock wave representation treated in Section 4.4. This discrepancy leads to compressive unloading earlier than theoretically expected. To illustrate that this actually is the case, it is possible to compare the results when using more elements, i.e. use a more accurate depiction of the shock wave. Such a comparison is illustrated in Figure 4.49, where it is seen that the inelastic strains after one load cycle distribute differently when increasing the number of elements.

One may, theoretically, assume that the shock wave alternates between tension and compression over an infinitesimal distance. If this was the case it is reasonable to assume that the inelastic strains after one load cycle would develop all the way to the far left in the structure, i.e. the compressive unloading does not occur earlier than expected. If this follows the principle in Figure 4.49, it might be possible to predict how inelastic strains will distribute for an idealized shock. The red solid line in Figure 4.49 illustrates a conceptual distribution of inelastic strains for an idealized shock wave, i.e. using infinite number of elements for example. However, using to many elements yield other complications in the structural response as discussed in Section 4.6.6, why such results cannot be extracted to confirm this concept.
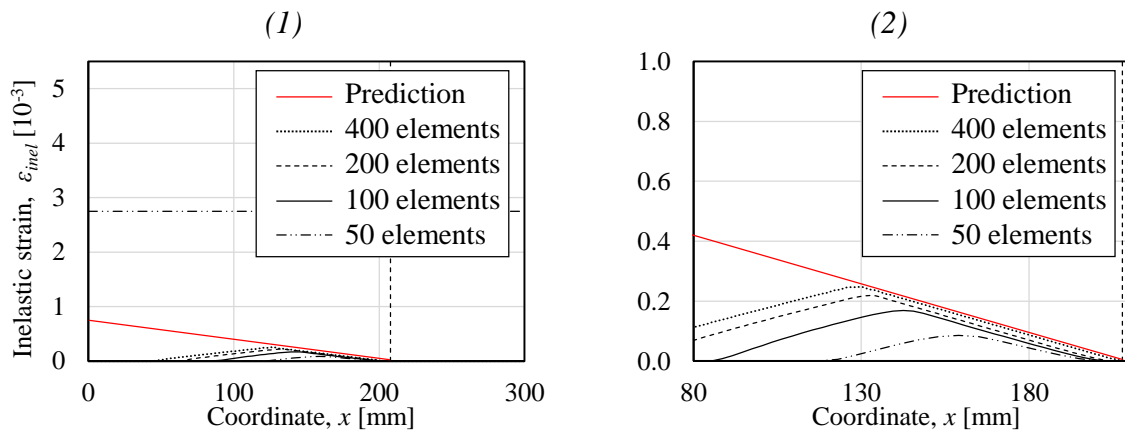
Figure 4.49 *(1) Comparison of inelastic strain distribution after one load cycle using N = 50, N = 100, N = 200 and N = 400 elements and (2) magnified view. A conceptual distribution of inelastic strains is also predicted (red solid line) for an idealized shock wave.*

The reason why a conceptual distribution of inelastic strains is illustrated in Figure 4.49 is to highlight the difference in structural response that an idealized shock wave might cause. Since the strain distribution after one load cycle will govern how strains localize during the following load cycles, it might be possible that spalling is expected somewhere else in the structure.

4.10.3 Successively development of inelastic strains

The other observation regarding how strains develop is that they are developed successively after crack initiation. This can be illustrated by studying how inelastic strains develop after crack initiation. As seen in Figure 4.50(2), the magnitude of the inelastic strain, $\varepsilon_{inel,x}$, successively increases after crack initiation.

Figure 4.50 *(1) Distribution of inelastic strains after one load cycle and (2) magnified view that illustrates that the magnitude of the inelastic strains, $\varepsilon_{inel,x}$, successively increases after crack initiation*

This observation, i.e. that the magnitude of the inelastic strain successively increases after crack initiation, is the most fundamental within the hypothesis by Ekström. This is the main reason that a spalling crack is expected elsewhere from the location of crack initiation. A possible explanation of this structural response is that inelastic strains can only develop if there is a driving force behind it. Ekström (2016) suggests that the driving force for is the discrepancy between a linear elastic stress distribution

and a stress distribution when including limitations in tensile strength. This principle is illustrated in Figure 4.51 where $\Delta\sigma$ denotes the difference in stress between the tensile strength and a linear elastic stress distribution.
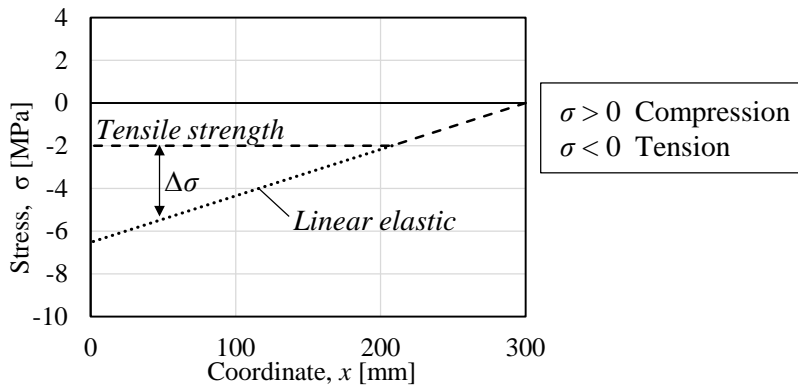
Figure 4.51   Illustration of possible driving force, $\Delta\sigma$, generating inelastic strains in the structure.

By the reasoning in Figure 4.51, one may correctly argue that the highest driving force $\Delta\sigma$ is found at the far left in the structure. Therefore, the magnitude of the inelastic strains, after one load cycle, should be highest at this location. This observation might give further support to the conceptual strain distribution illustrated in Figure 4.49.

To further highlight that the concept given in Figure 4.51 seems to be accurate is to actually compare the development of inelastic strains for different gradients of the load. Figure 4.52 shows a comparison between the strain development gradients for two different load durations. The comparison is between reference load duration $t_{dur,1} = 1.31$ ms and when increasing the load duration with 50 % to $t_{dur,2} = 1.965$ ms. The conclusion of Figure 4.52 is that the relation between the load durations and corresponding gradients are more or less the same, which gives support to this concept.

Figure 4.52   Comparison between strain development gradients for two different load durations, $t_{dur,1} = 1.31$ ms and $t_{dur,2} = 1.965$ ms.

To conclude Section 4.10, two observations are important to describe in order to understand the principle of how inelastic strains develop. They are related to the gradients on both sides of the peak value of the inelastic strain, see Figure 4.53(2).
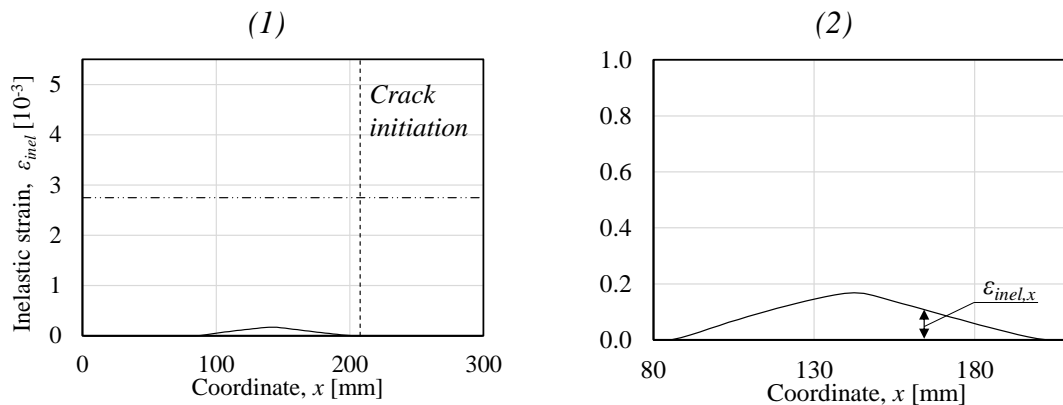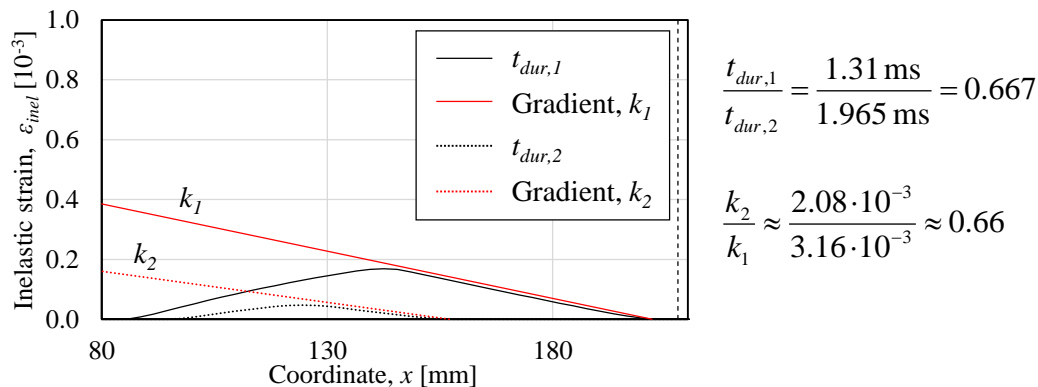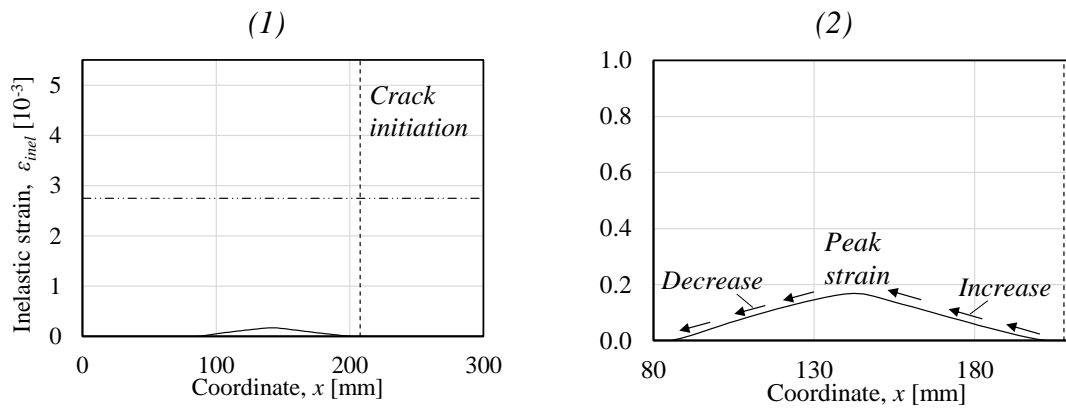
Figure 4.53 *(1) Distribution of inelastic strains after one load cycle and (2) magnified view that illustrates the gradients on both sides of the peak strain, one is increasing and one is decreasing.*

The reasons for the decrease (left side of the peak strain) and the increase (right side of the peak strain) has been explained in Section 4.10.2 and Section 4.10.3 respectively. Therefore, the two questions stated in the beginning of Section 4.10 can be answered as;

- The reason why inelastic strains do not develop to the far left in the structure after the first load cycle is because the shock wave in the numerical analysis alternates between tension and compression over a certain distance. This leads to earlier unloading than theoretically expected, which explains the lack of inelastic strains in the left part of the structure.

- The reason why strains develop successively a certain distance from the coordinate of crack initiation is because of the driving force that governs the development of inelastic strains. This driving force can be considered to be the difference in stress between tensile strength and a linear elastic model. This concept gives further support to the idea that inelastic strains should, after one load cycle, develop to the far left in the structure if a perfect shock wave front was used in the model.

5 Discussion

5.1 Overview

The results presented in Chapter 4 emphasize the complexities in evaluating spalling in concrete subjected to shock wave blast. By using a one dimensional finite element model and study the distribution of inelastic strains under non-monotonic load, the fracture location is predicted where the inelastic strain exceeds the ultimate strain. However, there are several factors that needs further elaborations and discussion, why this chapter includes detailed discussions for the most important results and observations in Chapter 4. The treated subjects in this discussion are mainly focused on the limitations in the model, the parametric study and the results presented when including non-linear strain softening and pressure time gradient.

5.2 Model limitations

The first obvious limitation in the model is the incorrect representation of a shock wave. It was shown in Section 4.4 that there is a large discrepancy in the numerical and the analytical shock wave representation. However, in reality the shock wave does not necessarily correspond to the analytically predicted, which is confirmed in Chapter 3 where experimental setups are studied. This means that even in reality there is a certain distance over which the stress wave equalizes, why the numerical representation of a shock wave unintentionally might be represented quite well. However, this is only true for a long load duration. As the load duration decreases the discrepancy between numerical and analytically predicted shock wave increases.

Further, a substantial limitation in the model is the exclusion of material properties at high strain rates. It was shown in Section 2.3.4 that concrete, at strain rates corresponding to blast loading, shows a considerable increase in strength both in tension and compression. This increase is mostly ascribed to structural effects, why this phenomenon needs to be implemented in the material model. The exclusion of high strain rate effects, together with the difficulties in shock wave representation, is the main reason why the results are not considered to be comparable with experimental results. This is a major limitation since there is no certain method of verifying and comparing the results from the numerical model. Nevertheless, the conceptual spalling response of a short load duration is similar to that obtained in experiments; i.e. that a fully open crack develops close to where it is initiated regardless of material model used.

5.3 Parametric study

The parametric study in Section 4.6 is performed in order to determine and compare the structural response when input in the numerical model changes. One of the important limitations of this parametric study is that only one parameter is varied at a time. One may suggest that a parametric study should be more extensive, including several different configurations of parameter variation, in order for the study to be more reliable. Although this is true, it would extend this thesis substantially beyond the scope of the study. This is why this part of the study is limited to one parameter variation at a time.

The first important conclusion of this section is that the material model used becomes irrelevant for short load duration, i.e. the inelastic strains exceeds the ultimate strain already after the first load cycle. Therefore, the concept that crack propagation in concrete occurs during non-monotonic loading is only true if the load duration is long enough.

The general complication found in the parametric study is how to interpret the results, in terms of distribution of inelastic strains over the concrete element. All results in the parametric study assumes a fracture zone of three times the maximum aggregate size and corresponding fracture energy 132 N/m. As showed in Section 4.9, this assumption is fairly accurate for the results presented by Ekström. However, when changing parameters this assumption becomes inaccurate, why adjustments in fracture zone are needed in almost every presented result in the parametric study. Therefore, the preliminary results presented by Ekström cannot with certainty be said to repeat themselves without such investigations. However, one important observation, which seems to hold up throughout the parametric study, is that inelastic strains develops during cyclic loading/unloading, rather than instantaneous as assumed in conventional theory described by McVay (1988).

Two parameters that influence the results substantially is the mesh density and damping ratio. It is mentioned in Section 4.4.5 that, with regard to shock wave representation, it is favorable to have as many elements as possible and as low damping ratio as possible. Under these circumstances, the numerical shock wave representation is very similar to the analytical. However, upon studying the distribution of inelastic strains for such models it becomes obvious that the results are not reliable. For instance, regarding the mesh density, increasing the number of elements eight times requires adjustment in fracture zone to give a less brittle material. The same principle applies for low damping ratios, why such configurations are not reliable without corresponding fracture zone adjustment.

The principle of how to adjust the fracture zone presented in Section 4.9 is a method developed in this thesis and has not been confirmed nor compared with current literature. However, the method has been developed during extensive discussions with supervisor Morgan Johansson. Since detailed adjustments on the fracture zone are necessary in most presented results in the parametric study, the suggestion is that such adjustments are to be implemented in the numerical routine.

There is, however, some complications in using the presented method of fracture zone adjustment, and one of which relates to how one interprets the case when more than one zone has inelastic strains exceeding the ultimate strain. One may interpret the result as that more than one spalling crack has developed, which means that fracture zone adjustments should correspond to each spalling crack zone individually. On the other hand, the numerical routine is not capable to represent the case where more than one spalling crack takes place. The reason for this is that when the first spalling crack takes place, a new free edge develops in the structure and the shock wave should, therefore, be reflected on this new free edge instead of the original free edge. This effect is not captured in the numerical model, why the results after the first spalling crack takes place should be neglected when studying the distribution of inelastic strains. It is on the other hand also possible to consider the option that several fracture zones do not correspond to several spalling cracks, but rather one spalling crack numerically smeared out over a larger region.

5.4 Non-linear strain softening and non-linear pressure time gradient

As treated in Section 4.7 and 4.8, a further development of the model presented by Ekström is when including a non-linear strain softening as well as a non-linear pressure time gradient. Regarding the implementation of non-linear strain softening for a plasticity model, the results show earlier and more distinct crack localisation, which is expected. By keeping constant fracture energy over different strain softening curves, the material ductility changes which is illustrated in the results. Regarding the exponential crack softening, which theoretically has infinite ultimate crack opening, the ultimate crack opening is set to the same value as for the bi-linear strain softening curve. By doing this, there is only negligible difference in structural response, why the conclusion is that using bi-linear strain softening is a sufficient simplification of an exponential strain softening curve.

In reality, both the strain softening curve and the pressure time gradient are non-linear, why such a case can be considered as the most accurate when comparing with reality. Since the pressure-time gradient at the time of crack initiation becomes larger when the load decreases exponentially, the results confirms the prediction that inelastic strains also develop faster. Although the development of inelastic strains occurs at different time frames for different crack softening and pressure time gradients, the important observation from this study is that the spalling crack for a plasticity model appears at about the same place for all different configurations.

The distribution of inelastic strains for a damage model also coincide when including a non-linear strain softening curve. Therefore, no spalling crack can be observed for either damage models when changing the crack softening relation. For the damage-plasticity model however, the expected spalling crack changes when the strain softening becomes bi-linear, and is in the same region where a spalling crack is expected for a pure plasticity model. For this reason, it seems as a coincidence that the spalling crack appears where Ekström suggests for a damage-plasticity model, i.e. in the same location as predicted by McVay, see Figure 4.18(c). It is important to once again highlight the complications in choosing the fracture zone, since inconsistency in the fracture zone for different strain values is present in all results in this thesis.

6 Conclusions

6.1 Overview

In addition to the discussion given in Chapter 5, this chapter aims to summarize this thesis project by presenting the most important results and conclusions. A general conclusion is that spalling in concrete subjected to shock wave blast is a highly complex subject to evaluate, which has been seen in Chapter 4. The main reason for this is that there are many simplifications and model limitations, which leads to results that are complicated to verify the reliability of.

6.2 Summary of results and observations

- The representation of a shock wave in the numerical analysis does not coincide with the analytically predicted. Therefore, crack initiation occurs at a different location than predicted using the conventional theory. This can be adjusted by increasing the number of elements and adjusting the damping ratio in the analysis, for which crack initiation converges towards the analytically predicted. However, such changes result in other complications with how inelastic strains distribute in the structure.

- For loads with short duration, the structural response in terms of distribution of inelastic strains becomes the same regardless of whether a plasticity, damage or damage-plasticity model is used. This is because the inelastic strains exceed the ultimate strain already after the first load cycle; i.e. the path used for unloading and reloading becomes irrelevant. Hence, the structural response is highly dependent on the gradient of the pressure time relation.

- The results from experiments cannot be obtained using the current model. This conclusion is mainly based on two factors. Firstly, the difficulties in achieving the same shock wave as in experiments, which will lead to a discrepancy in actual shock wave and numerical shock wave. This will certainly yield different structural response as shown in the parametric study. Secondly, and the most complicated, is the exclusion of strain rate effects in the numerical model. Based on experiments to evaluate spalling, it was shown that the material properties for concrete change drastically for strain rates corresponding to blast loading.

- Including non-linear strain softening and non-linear pressure time relation will not change the location of where a spalling crack is expected. Regarding non-linear strain softening, it will only result in earlier strain localisation which was expected. Further, a bi-linear strain softening curve is sufficient to be used since the change in structural response is negligible. Regarding a non-linear pressure time relation, the location of crack initiation changes due to the increased gradient of the pressure time relation at the time of crack initiation.

- One reason why the results from the numerical models throughout this entire thesis is questioned is because the inconsistency and difficulties in how to choose the fracture zone. For this reason, a principle method of how to adjust the fracture zone is described in Section 4.9. However, some of the complications still remains after such fracture zone adjustment. Therefore, this subject is certainly something that needs further research and development.

6.3 Further studies and improvements

Based on the conclusions stated in Section 6.2, it becomes clear that further research within this field is required. There will, however, always be a difficulty in working with numerical models that simulate blast loading, due to the complexity in verifying the results with experiments. Despite this fact, there are two major factors that need further development and research.

Firstly, implementation of strain rate effects in the numerical model to more accurately reflect the material response. This implementation is highly important for the model to be considered as accurate. A strategy for such an implementation is to, in the material model, include that the concrete strength is dependent on the strain rate. So for a specific strain rate, the concrete strength is to be multiplied with the dynamic increase factor, DIF.

Secondly, further implementation and investigations on how to treat the fracture zone. The inconsistency in crack band width over different strain values is certainly something that needs further attention and development. This thesis presents one approach on how to adjust the fracture zone iteratively, which shows that in some cases it is possible to achieve the same fracture energy and fracture zone as predicted. However, this approach needs further development and its application and reliability need to be checked.

Finally, it is important to perform further parameterisation of the numerical model when including non-linearity in both crack softening and pressure time relation, since those configurations only is treated and compared with Ekström's results. After such a parameterisation is performed, it can be valuable to develop a two dimensional model where varying material properties can be implemented for different elements. With a two dimensional model it is also possible to implement a shock wave with non-flat pressure distribution, which resembles the reality more accurately.

CHALMERS, *Civil and Environmental Engineering*, Master's Thesis BOMX02-16-26

7 Bibliography

Acosta, P.F. (2011) Overview of UFC 3-340-02 Structures to Resist the Effects of Accidental Explosions. In *Structures Congress 2011*, pp. 1454-1469.

Bažant, Z.P. (2002) Concrete fracture models: testing and practice. In *Engineering Fracture Mechanics*, Vol. 69, No. 2, pp. 165-205. New York: Pergamon Press.

Bischoff, P.H. & Perry, S.H. (1991) Compressive behaviour of concrete at high strain rates. In *Materials and Structures*, Vol. 24, No. 6, pp. 425-450.

CEB (1993) *CEB-FIP Model Code 1990, Design Code*. Thomas Telford, Lausanne, Switzerland.

Chen, W., Song, B. (2011) *Split Hopkinson (Kolsky) Bar: Design, Testing and Applications*. Boston: Springer US.

Cormie, D., Mays, G. & Smith, P. (2009) *Blast effects on buildings*, 2nd Edition, London: Thomas Telford.

Dilger, W.H., Kand,R. & Kowalczyk, R. (1984) *Ductility of Plain and Confined Concrete Under Different Strain Rates*. ACI Journal, Jan-Feb, pp. 73-81.

Ekström, J. (2016) *Spalling in concrete subjected to shock wave blast.* In *Engineering Structures.* Vol. 122, pp. 72-82.

Fortifikationsverket. (2011) Fortifikationsverkets kontruktionsregler FKR 2011. Eskilstuna: Fortifikationsverket. (Dnr 4535/2011).

Gebekken, N., Greulich, S., & Pietzsch, A. (2001) *Performance of Concrete Based Building Materials Against Blast and Impact*. Munich, Germany: University of the Federal Armed Forces.

Gylltoft, K. (1983). *Fracture mechanics models for fatigue in concrete structures*. Luleå: Luleå University of Thechnology. (PhD Thesis 1983:25D at Division of Structural Engineering).

Johansson, M. (2000). *Structural Behaviour in Concrete Frame Corners of Civil Defence Shelters: Non-linear Finite Element Analyses and Experiments*. Gothenburg: Chalmers University of Technology. (PhD Thesis at Department of Structural Engineering).

Johansson, M., & Laine, L. (2012a) *Bebyggelsens motståndsförmåga mot extrem dynamisk belastning. Del 1: Last av luftstötvåg.* Publ.no. MSB449. Karlstad: Myndigheten för samhällsskydd och beredskap.

Johansson, M., & Laine, L. (2012b). *Bebyggelsens motståndsförmåga mot extrem dynamisk belastning. Del 3: Kapacitet hos byggnader.* Publ.no. MSB451. Karlstad: Myndigheten för samhällsskydd och beredskap.

Johansson, M. (2013a) *Fasadförstärkning mot impulslast (Strengthening of facade subjected to impulse loading. In Swedish)*. Reinertsen Sverige AB, Selection of document 12100471-01/0, 2013-10-10. Göteborg.

Johansson, M. (2013b) *Kontaktdetonation (Contact detonation. In Swedish).* Reinertsen Sverige AB, Working material. Göteborg.

Leppänen, J. (2004) *Concrete Structures Subjected to Fragment Impacts.* Gothenburg: Chalmers University of Technology. (PhD Thesis 2004:04 at Department of Structural Engineering and Mechanics).

Leppänen, J (2012) *Splitterverkan.* Publ.no. MSB345. Karlstad: Myndigheten för samhällsskydd och beredskap.

Magnusson, J. (2007) *Structural Concrete Elements Subjected to Air Blast Loading*. Stockholm: Royal Institute of Technology. (Licentiate Thesis at Department of Civil and Architectural Engineering).

Malvar, L. J. & Ross, C. A. (1998) *Review of strain rate effects for concrete in tension*. ACI Materials Journal, Vol. 95, No. 6, pp. 735-739.

McVay, M. K. (1988) *Spall Damage of Concrete Structures*. Vicksburg, Mississippi: Structures Laboratory, Department of the Army, Waterways Experiment Station, Corps of Engineers.

NCTC. (2014) Bomb Threat Stand-Off Distances *Counterterrorism 2014 Calendar*. http://www.nctc.gov/site/technical/bomb_threat.html (2016-02-09)

Plos, M. (1996) *Finite Element Analysis of Reinforced Concrete Structures*. Gothenburg: Chalmers University of Technology.

Reinhardt, H.W. & Cornelissen, H.A.W. (1984) Post-peak cyclic behaviour of concrete in uniaxial tensile and alternating tensile and compressive loading. In *Cement and Concrete Research*, Vol. 14, No. 2, pp. 263-270.

Ross, C.A., Jerome, D.M., Tedesco, J.W. & Hughes, M.L. (1996) *Moisture and Strain Rate Effects on Concrete Strength*. ACI Materials Journal, Vol. 93, No. 3, pp. 293-300.

Schuler, H., Mayrhofer, C. & Thoma, K. (2006) Spall experiments for the measurement of the tensile strength and fracture energy of concrete at high strain rates. In *International Journal of Impact Engineering*, Vol. 32, No. 10, pp. 1635-1650.

Seabold, R.B. (1970*) Dynamic Shear Strength of Reinforced ConcreteBeams, Part III*. Technical Report No. R-695, U.S. Naval Civil Engineering Laboratory, Port Hueneme, USA.

Sima, J.F., Roca, P. & Molins, C. (2008) Cyclic constitutive model for concrete. In *Engineering Structures*, Vol. 30, No. 3, pp. 695-706.

Soroushian, P., Choi, K-B. & Alhamad, A. (1986) *Dynamic Constitutive Behaviour of Concrete*. ACI Journal, Mar.-Apr., pp. 251-259.

Wang, F., Wan, Y. K., Chong, O. Y., Lim, C. H., & Lim, E. T. (2008) Reinforced Concrete Slab Subjected to Close-in Explosion. *LS-DYNA Anwenderforum*, pp. 21-28. Bamberg, Germany.

Wu, H., Zhang, Q., Huang, F. & Jin, Q. (2005) Experimental and numerical investigation on the dynamic tensile strength of concrete. In *International Journal of Impact Engineering*, Vol. 32, No. 1, pp. 605-617.

Yamaguchi, M., Murakami, K., Takeda, K. & Mitsui, Y. (2011) Blast Resistance of Polyethylene Fiber Reinforced Concrete to Contact Detonation. In *Journal of Advanced Concrete Technology*, Vol. 9, No. 1, pp. 63-71.

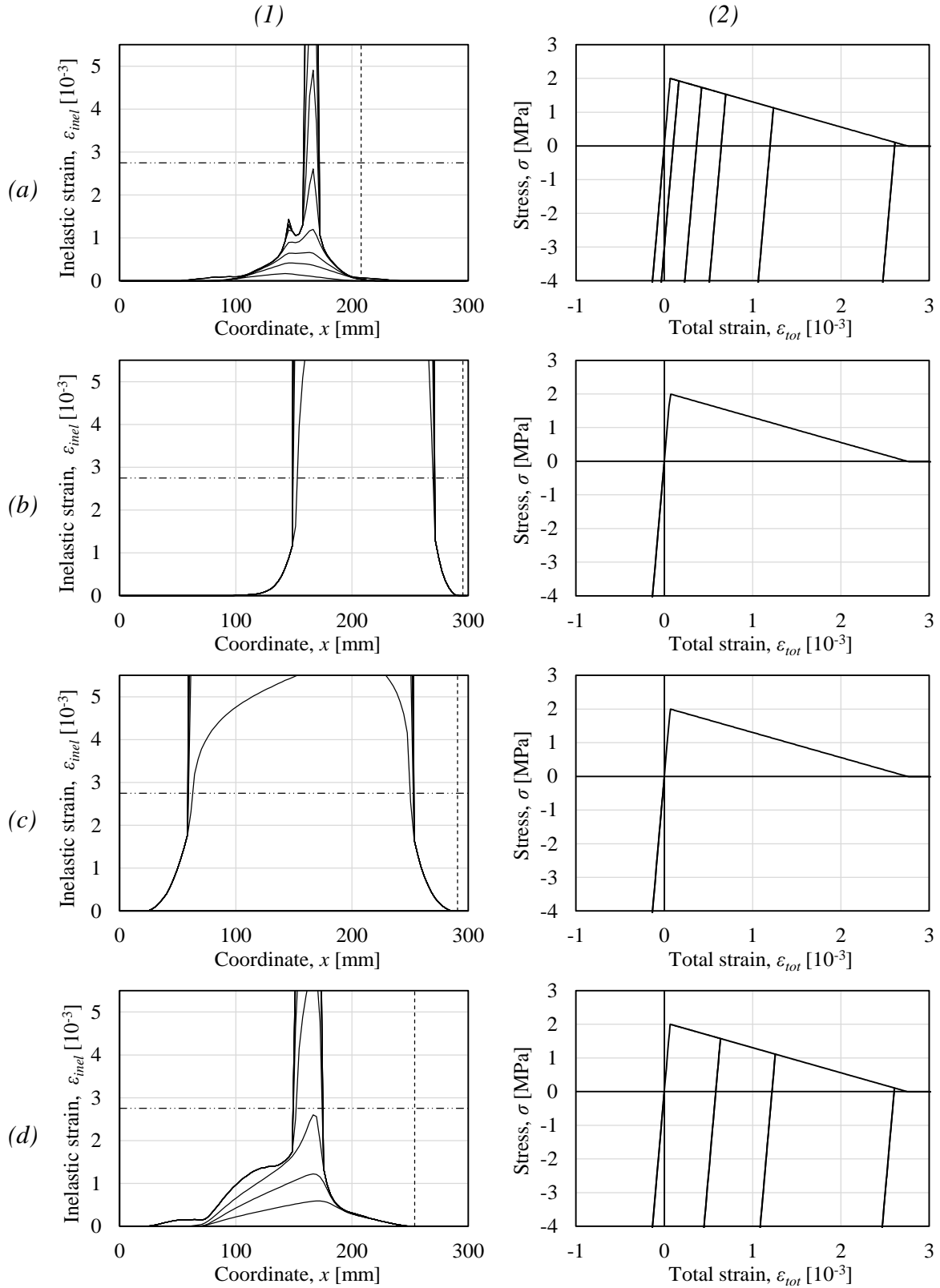# Appendix A   Results for plasticity model

A.1   Load duration

Figure A.1   (1) Distribution of inelastic strains and (2) corresponding material response for load duration (a) t_{dur} = 1.31 ms, (b) t_{dur} = 0.0655 ms, (c) t_{dur} = 0.131 ms and (d) t_{dur} = 0.655 ms.
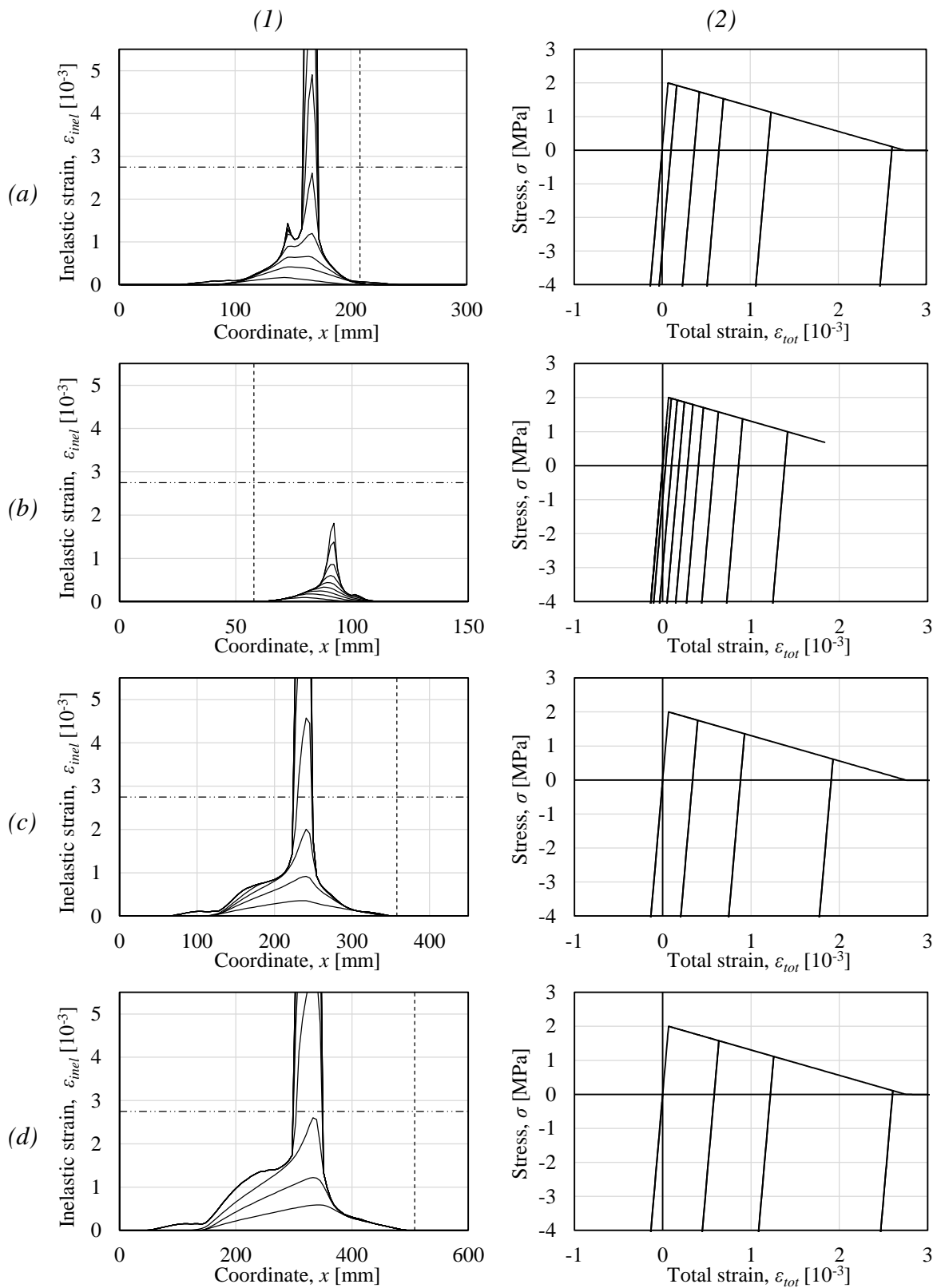
A.2   Concrete thickness

(1)   *(2)*

(a)

(b)

(c)

(d)

Figure A.2   (1) Distribution of inelastic strains and (2) corresponding material response for concrete thickness (a) L=300 mm, (b) L=150 mm, (c) L=450 mm and (d) L=600 mm.

A.3 Peak pressure
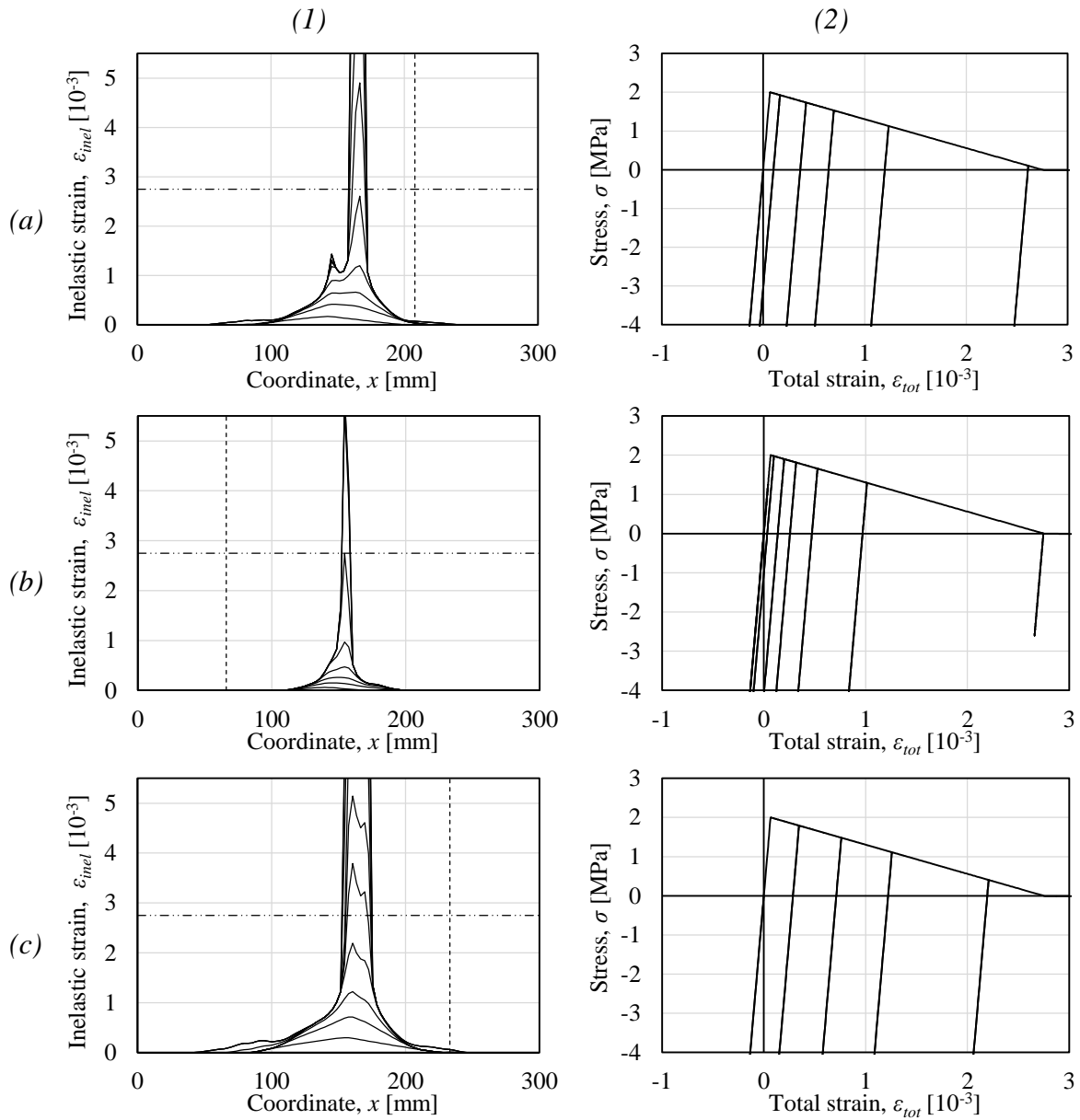
Figure A.3 *(1) Distribution of inelastic strains and (2) corresponding material response for peak pressure (a) $P_{peak} = 50.74$ MPa, (b) $P_{peak} = 20$ MPa and (c) $P_{peak} = 70$ MPa.*

A.4 Tensile strength

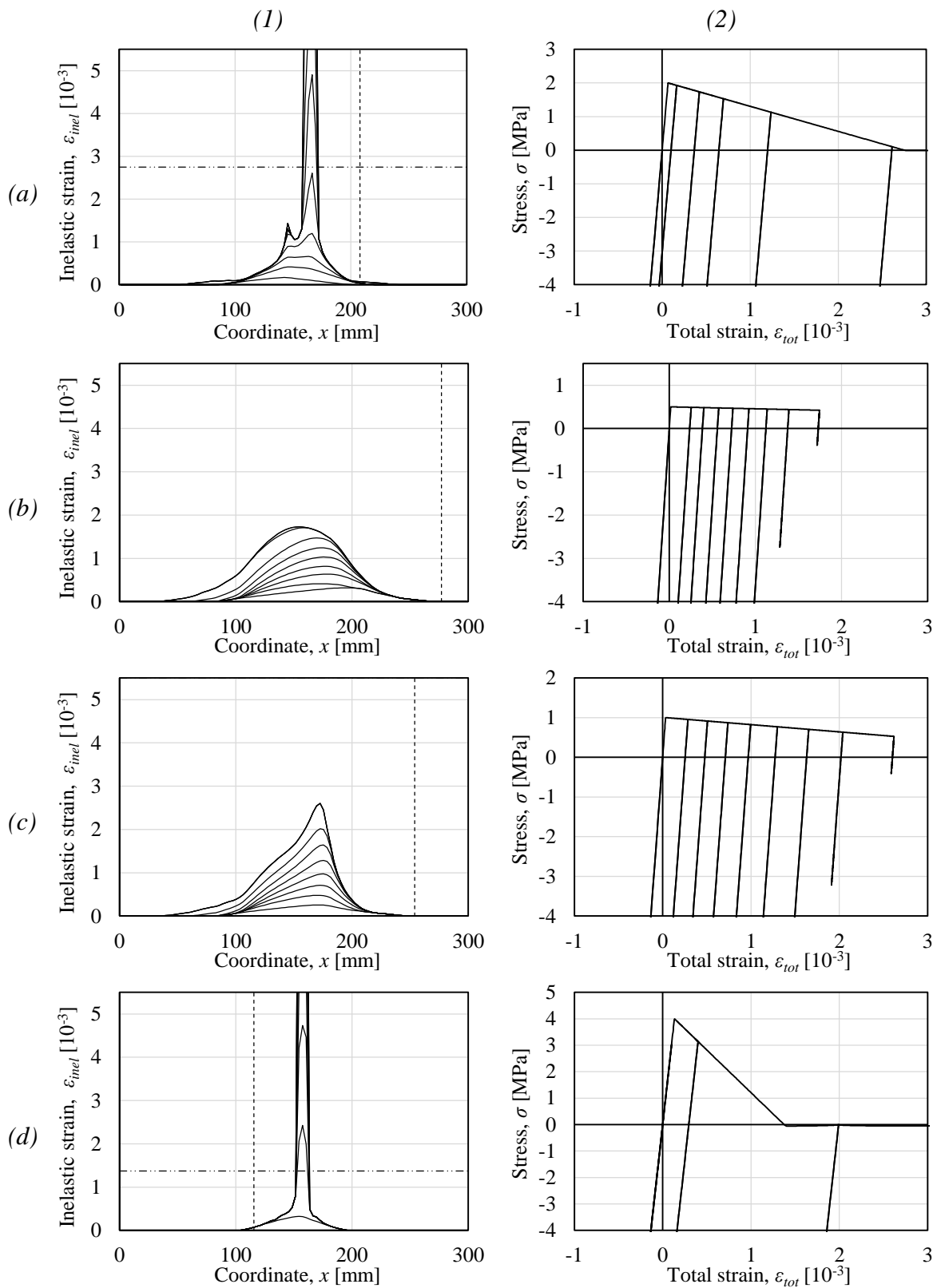*(1)*   *(2)*

(a)

(b)

(c)

(d)

Figure A.4   *(1) Distribution of inelastic strains and (2) corresponding material response for tensile strength (a) $f_{ct} = 2$ MPa, (b) $f_{ct} = 0.5$ MPa, (c) $f_{ct} = 1$ MPa and (d) $f_{ct} = 4$ MPa.*
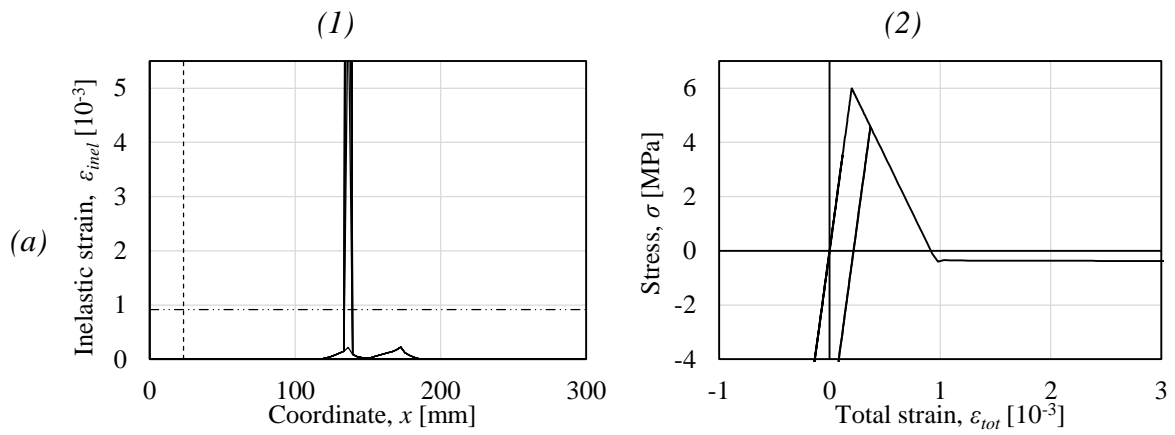
Figure A.5   *(1) Distribution of inelastic strains and (2) corresponding material response for tensile strength (a) fct = 6 MPa.*
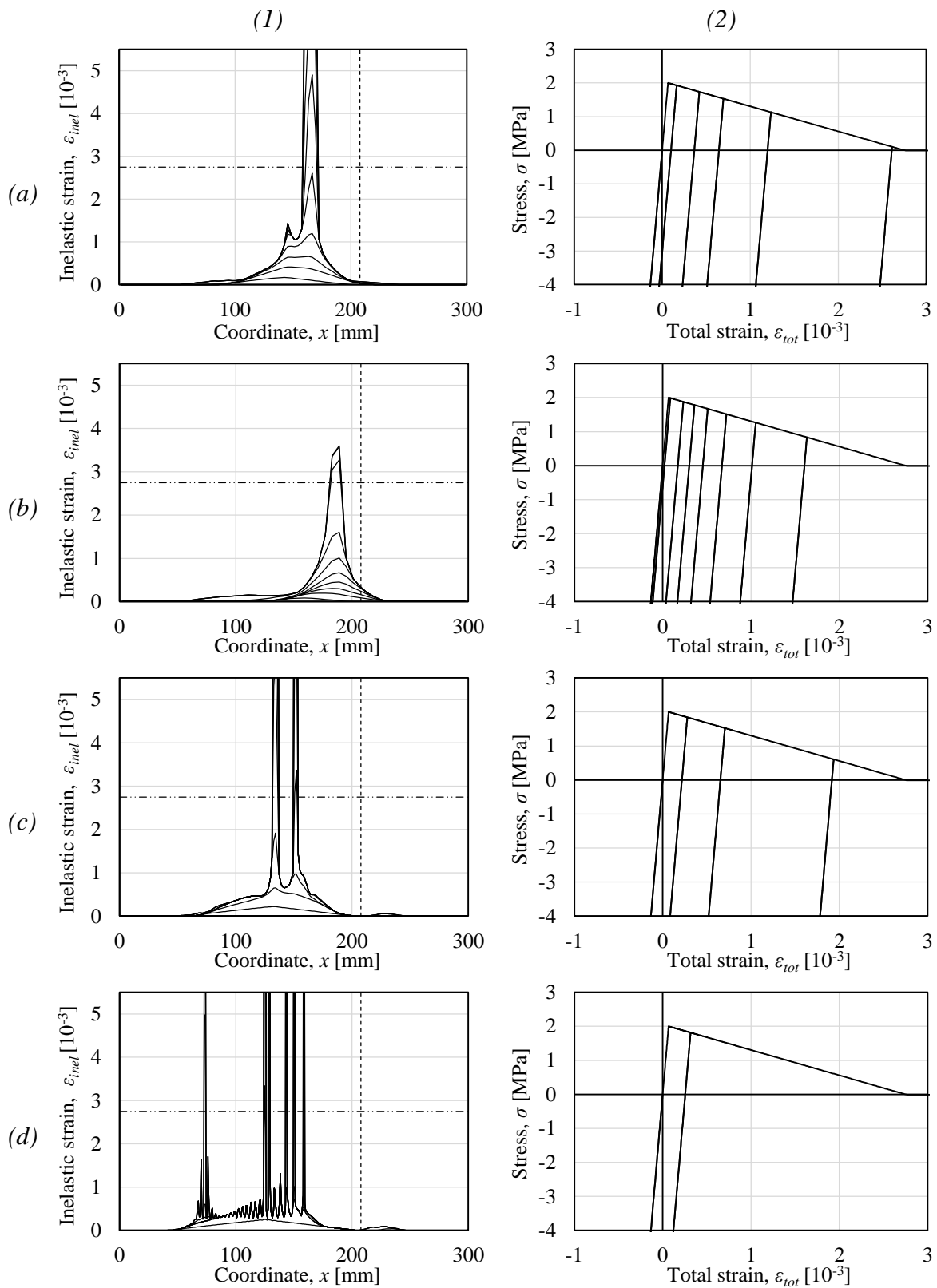
A.5 Number of elements

Figure A.6 *(1) Distribution of inelastic strains and (2) corresponding material response for number of elements (a) N = 100, (b) N = 50, (c) N = 200 and (d) N = 400.*
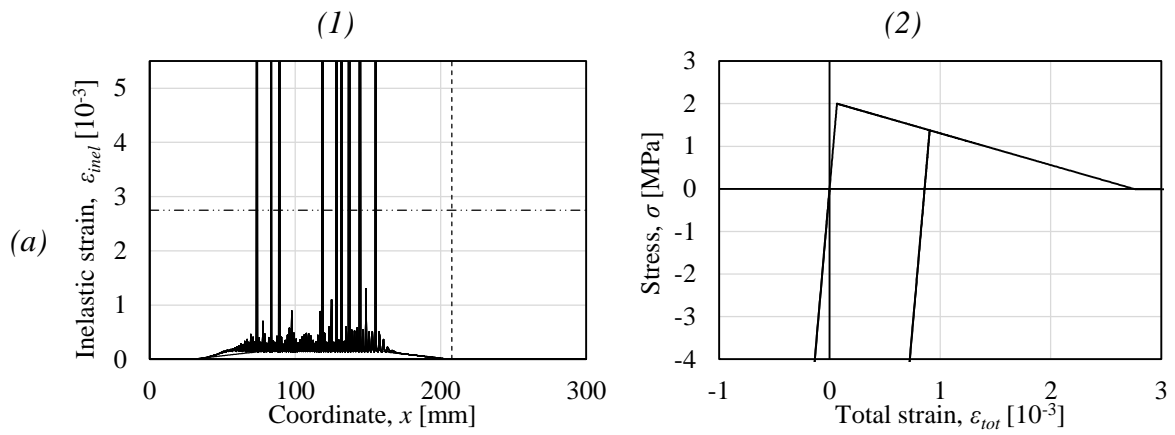
Figure A.7   (1) Distribution of inelastic strains and (2) corresponding material response for number of elements (a) N = 800.
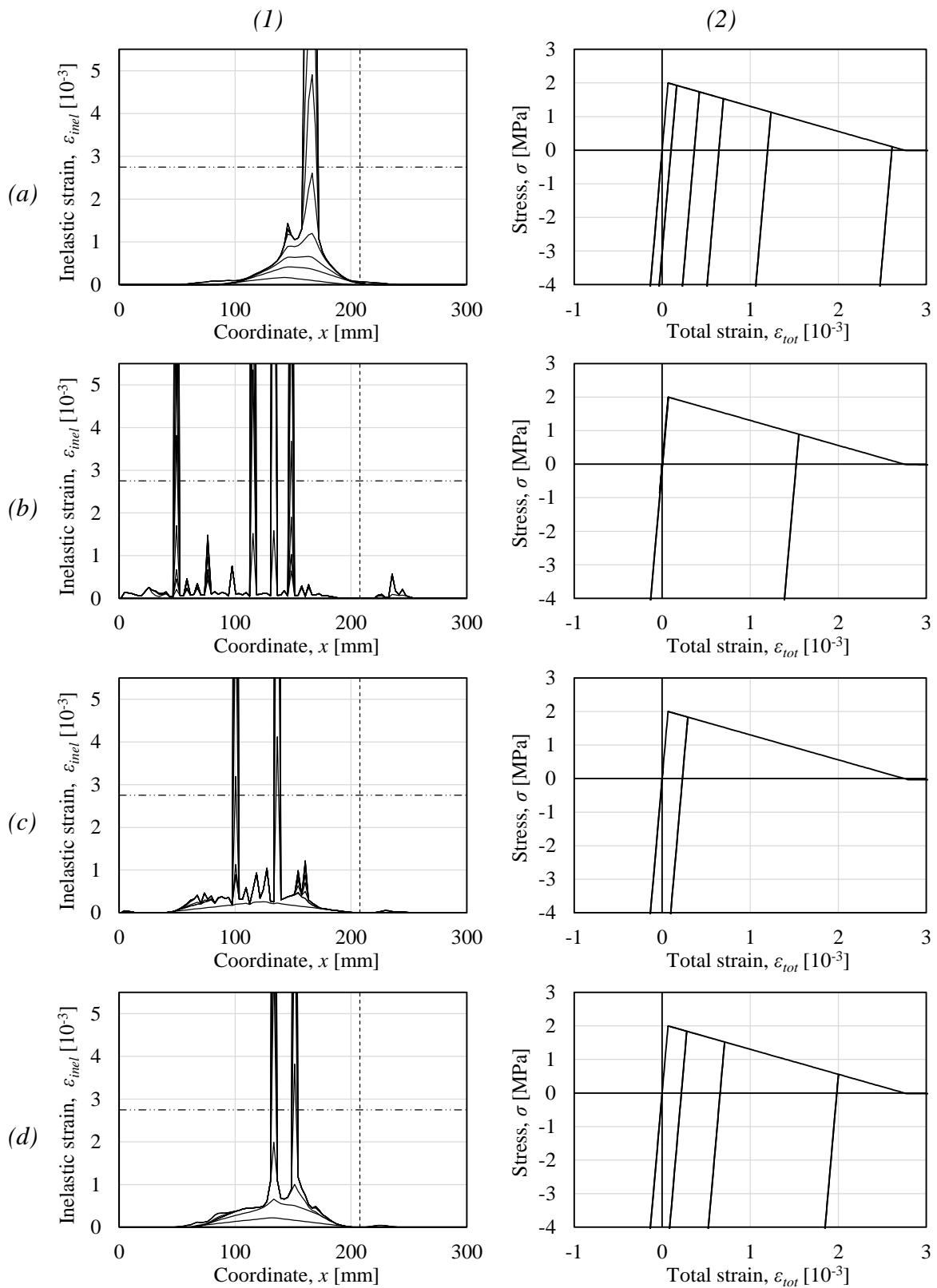
A.6 Damping ratio

Figure A.8 *(1) Distribution of inelastic strains and (2) corresponding material response for damping ratio a) ξ = 1.4, b) ξ = 0.1, c) ξ = 0.3 and d) ξ = 0.7.*
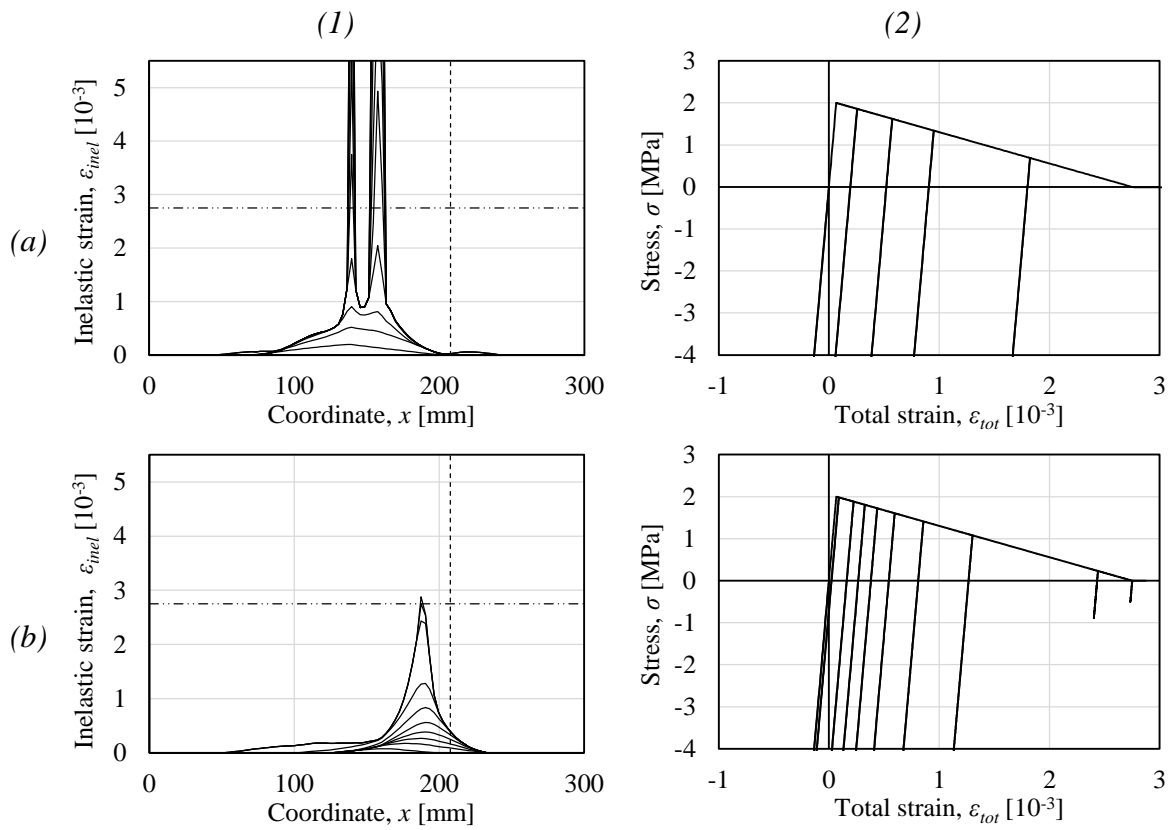
Figure A.9   *(1) Distribution of inelastic strains and (2) corresponding material response for damping (a) $\xi = 1.0$ and (b) $\xi = 3.0$.*

Appendix B   Results for damage model

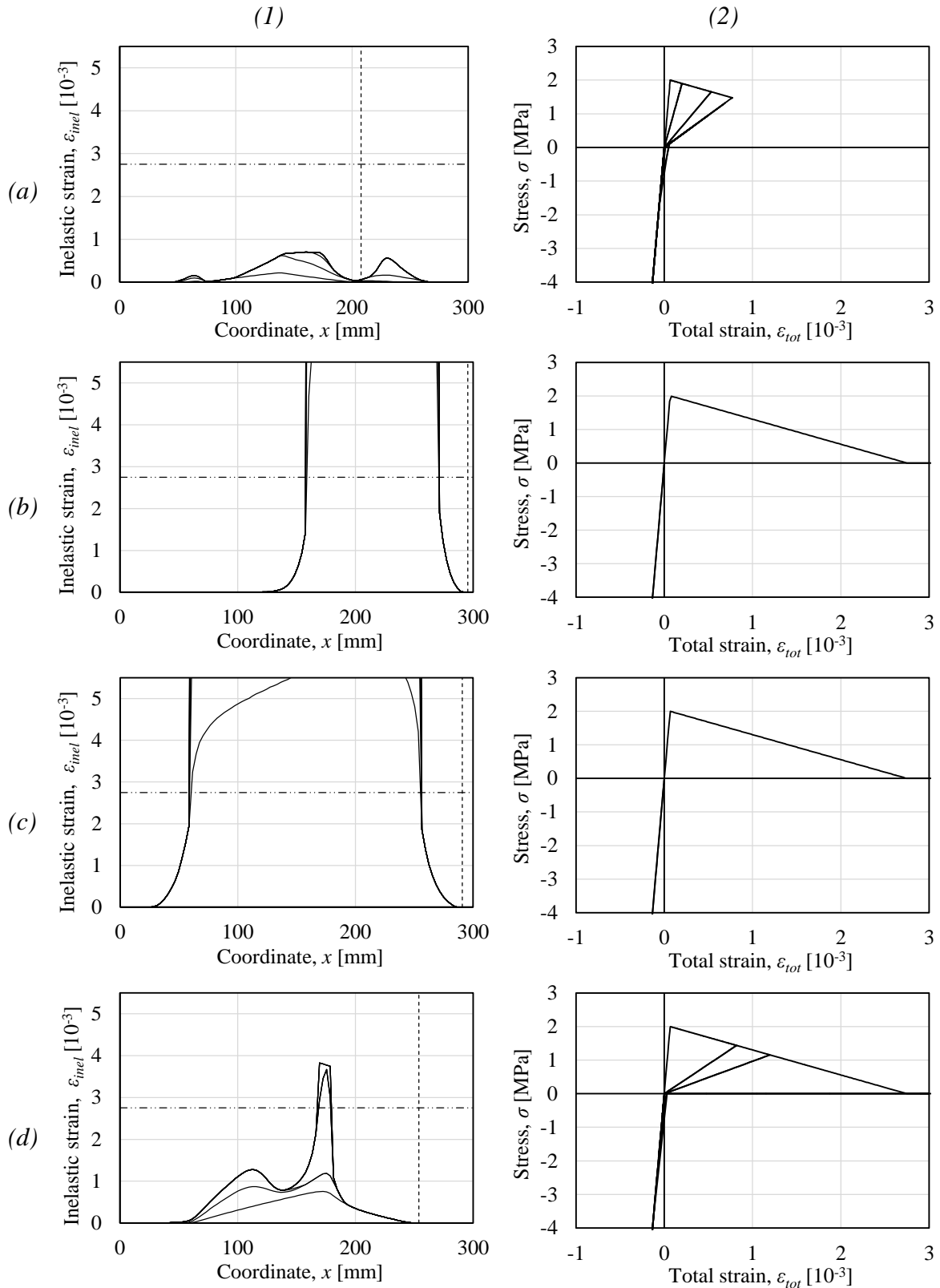## B.1   Load duration

Figure B.1   *(1) Distribution of inelastic strains and (2) corresponding material response for load duration (a) t_{dur} = 1.31 ms, (b) t_{dur} = 0.0655 ms, (c) t_{dur} = 0.131 ms and (d) t_{dur} = 0.655 ms.*

B.2 Concrete thickness

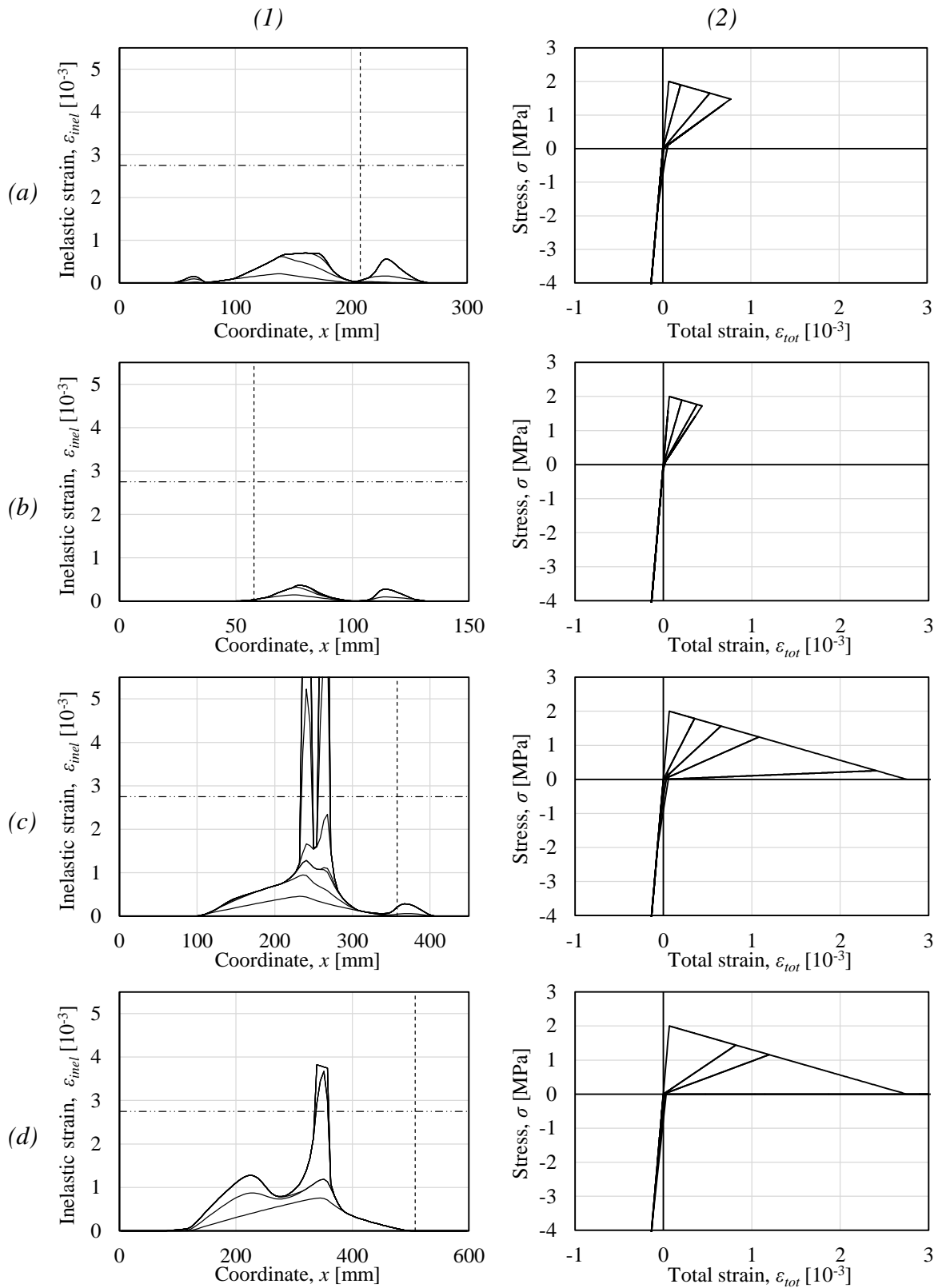*Figure B.2*   *(1) Distribution of inelastic strains and (2) corresponding material response for concrete thickness (a) L = 300 mm, (b) L = 150 mm, (c) L = 450 mm and (d) L = 600 mm.*

B.3 Peak pressure
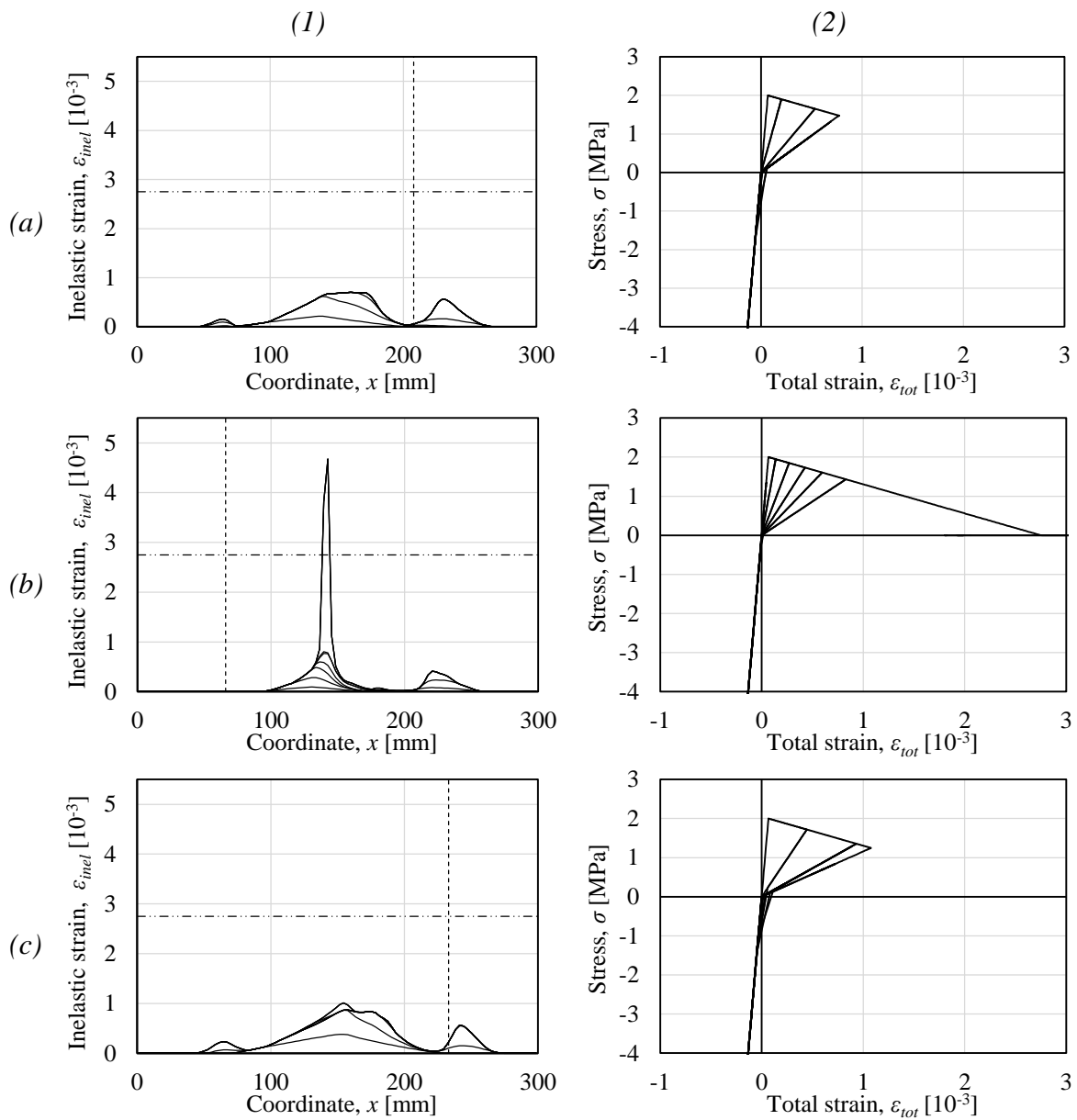
Figure B.3 *(1) Distribution of inelastic strains and (2) corresponding material response for peak pressure (a) P_{peak} = 50.74 MPa, (b) P_{peak} = 20 MPa and (c) P_{peak} = 70 MPa.*

B.4   Tensile strength

(1)   *(2)*
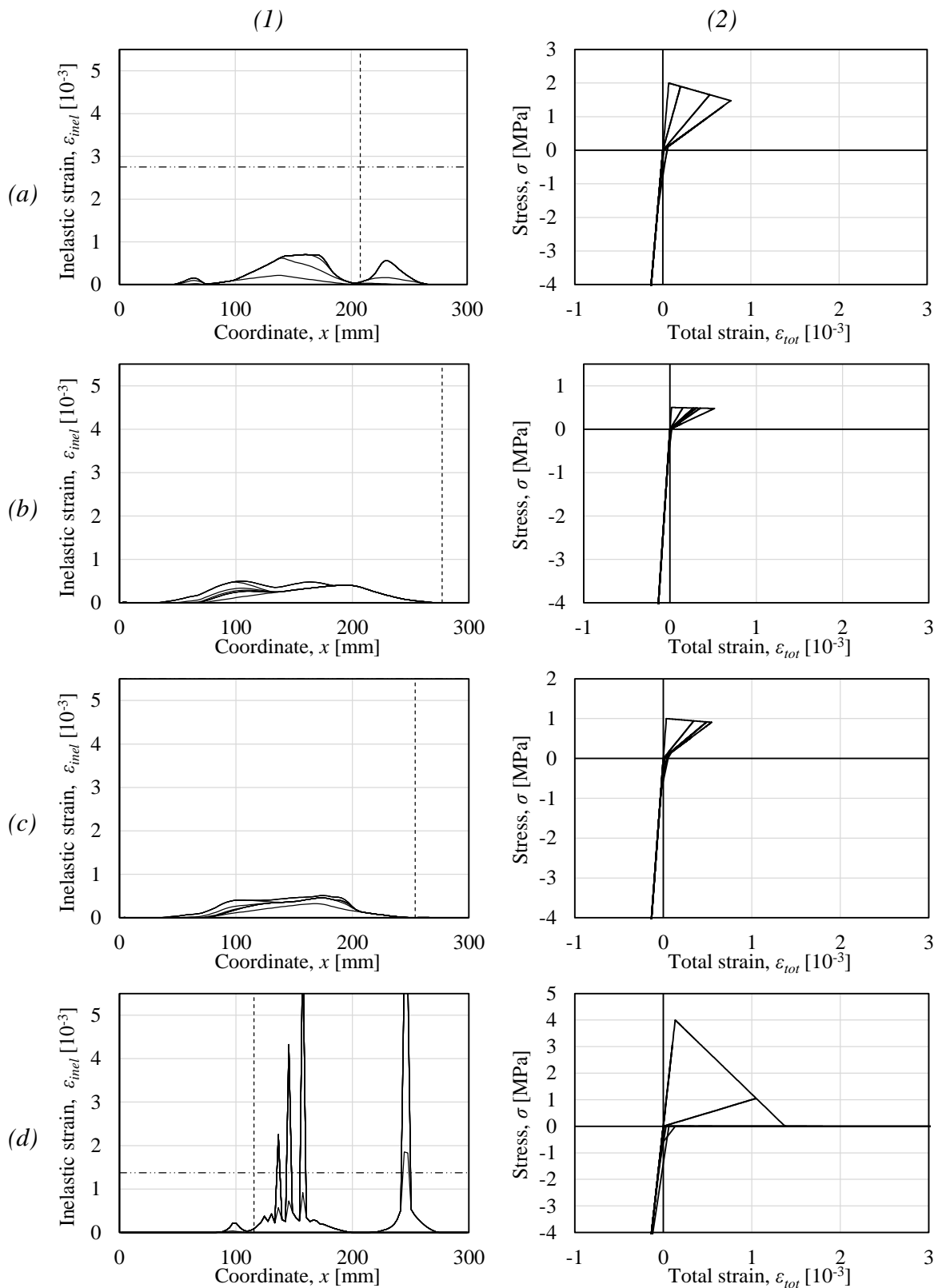
Figure B.4   *(1) Distribution of inelastic strains and (2) corresponding material*
response for tensile strength (a) f_{ct} = 2 MPa, (b) f_{ct} = 0.5 MPa,
(c) f_{ct} = 1 MPa and (d) f_{ct} = 4 MPa.

B.5   Number of elements

(1)   *(2)*

(a)

(b)

(c)

(d)
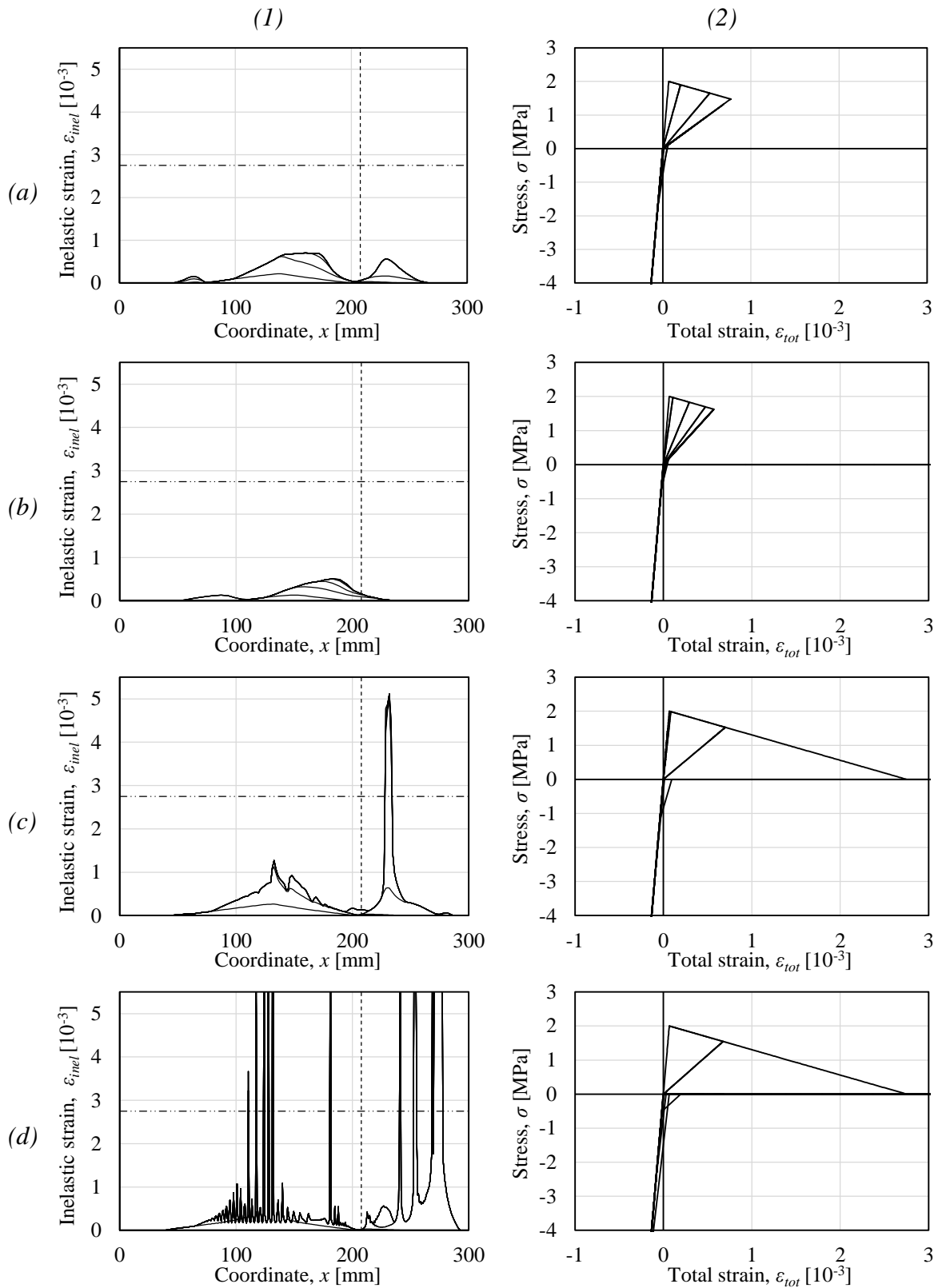
Figure B.5   (1) Distribution of inelastic strains and (2) corresponding material response for number of elements (a) N = 100, (b) N = 50, (c) N = 200 and (d) N = 400.
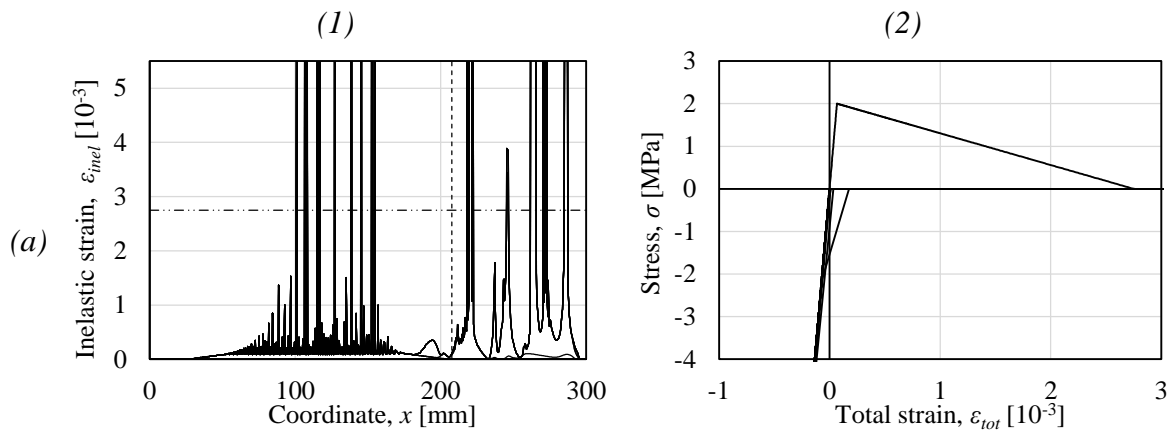
Figure B.6 *(1) Distribution of inelastic strains and (2) corresponding material response for number of elements a) N = 800.*

B.6 Damping ratio

Figure B.7 *(1) Distribution of inelastic strains and (2) corresponding material response for damping (a) ξ =1.0, (b) ξ =0.1, (c) ξ =0.3 and (d) ξ =0.7.*
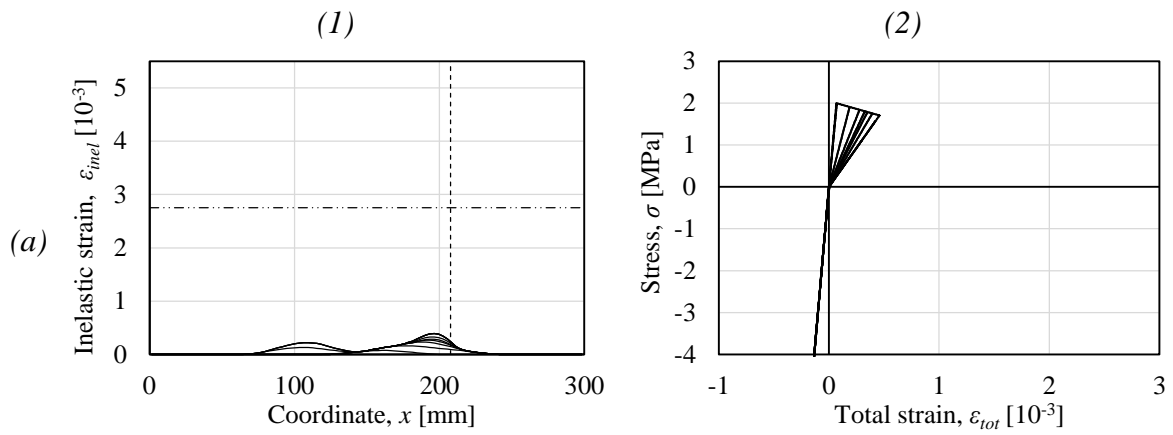
Figure B.8   *(1) Distribution of inelastic strains and (2) corresponding material response for damping (a) ξ = 3.0.*

Appendix C   Results for damage-plasticity model

C.1   Load duration
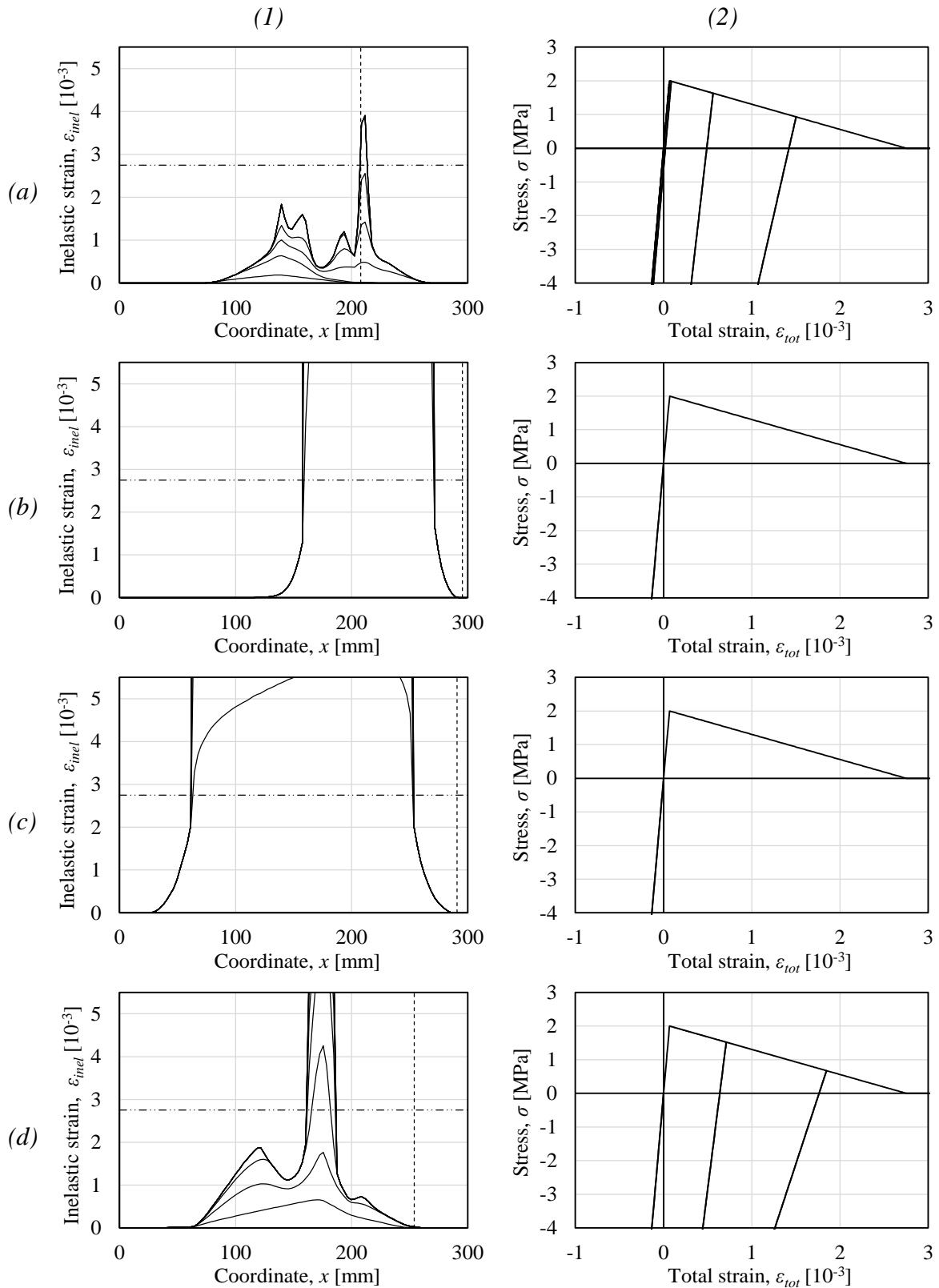
Figure C.1   *(1) Distribution of inelastic strains and (2) corresponding material response for load duration (a)* t_{dur} *= 1.31 ms, (b)* t_{dur} *= 0.0655 ms, (c)* t_{dur} *= 0.131 ms and (d)* t_{dur} *= 0.655 ms.*

C.2   Concrete thickness

(1)   *(2)*

(a)

(b)

(c)

(d)
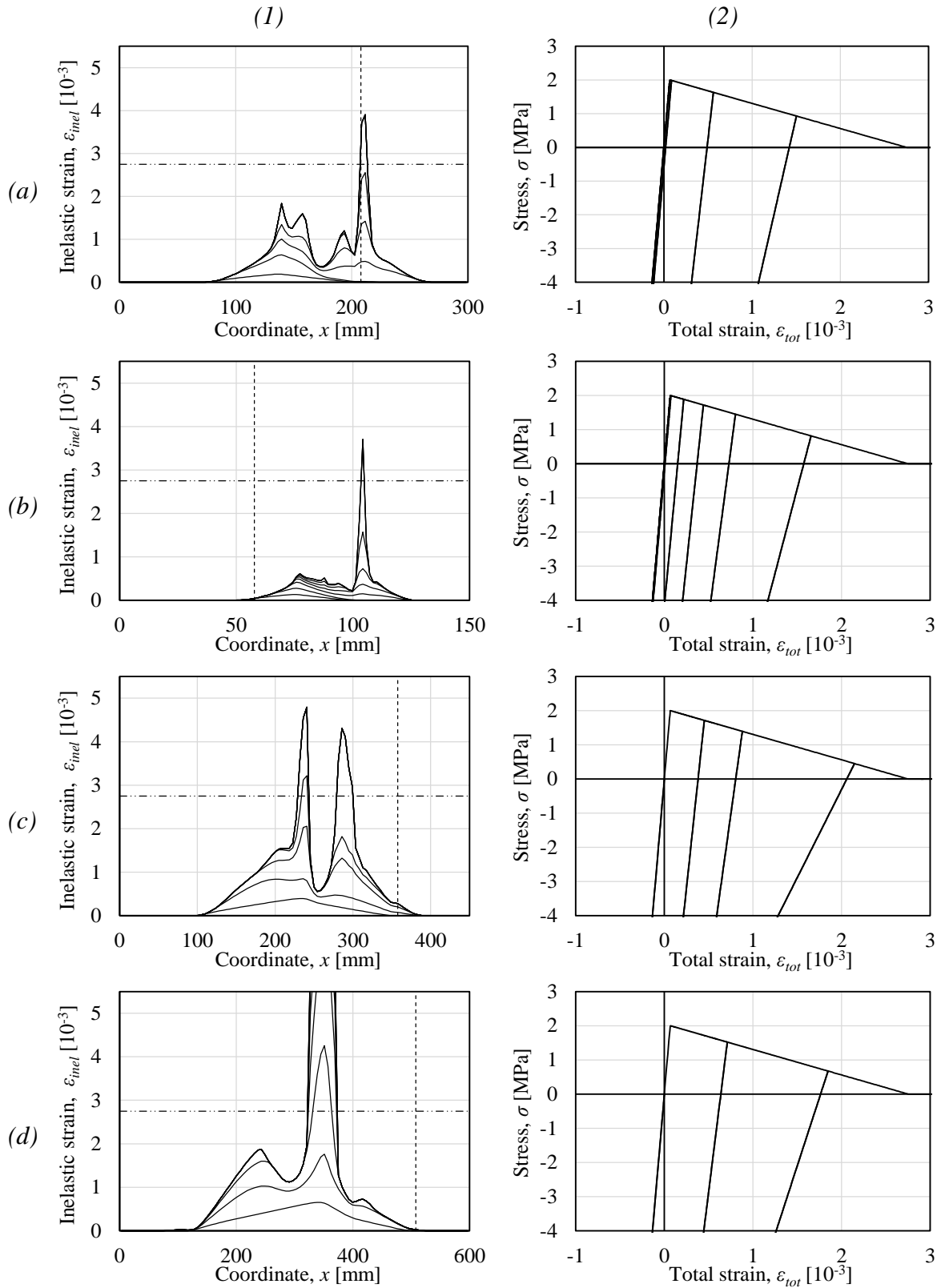
Figure C.2   *(1) Distribution of inelastic strains and (2) corresponding material response for concrete thickness (a) L = 300 mm, (b) L = 150 mm, (c) L = 450 mm and (d) L = 600 mm.*

C.3   Peak pressure

(1)   *(2)*

(a)

(b)

(c)
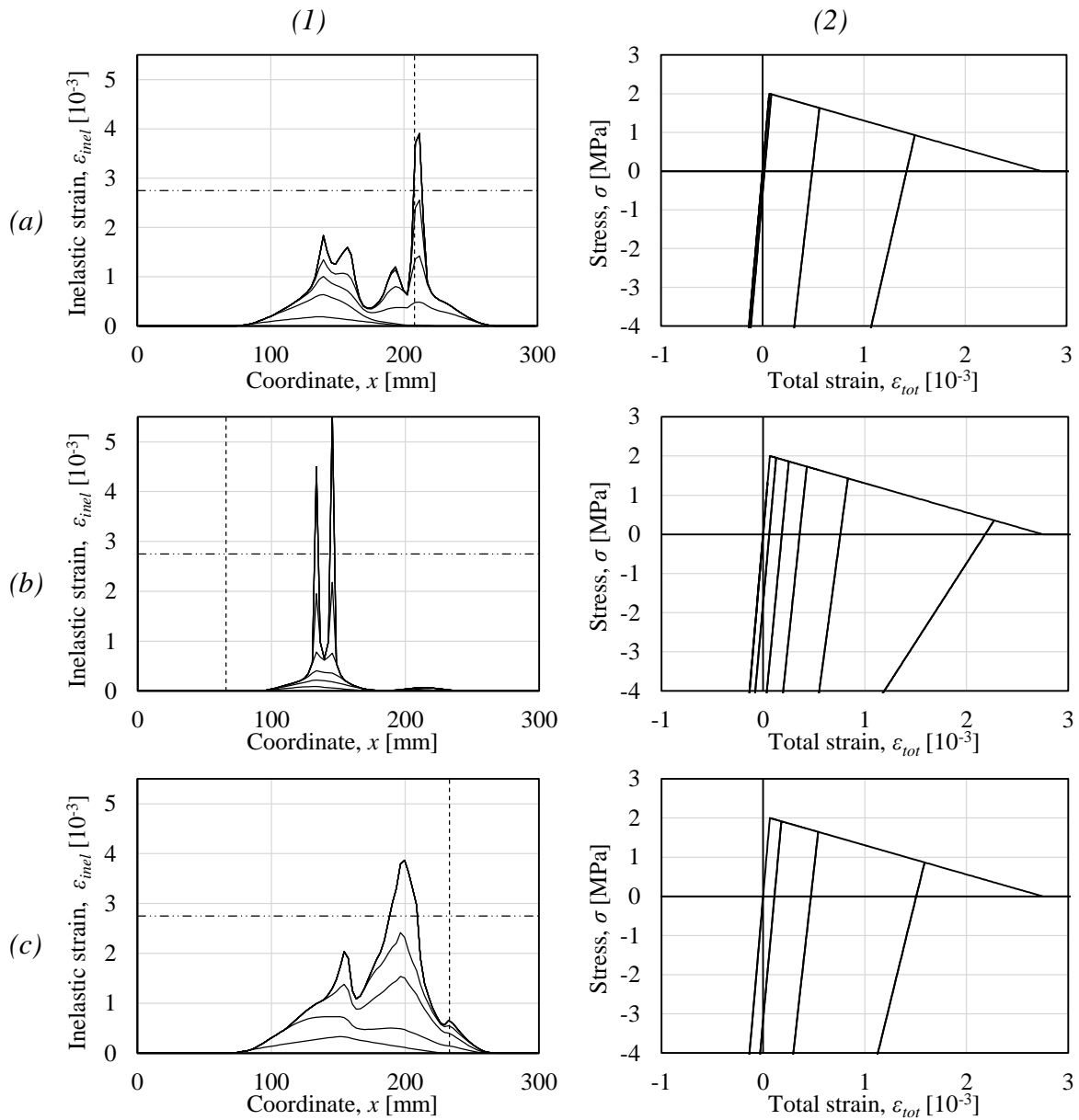
Figure C.3   (1) Distribution of inelastic strains and (2) corresponding material response for peak stress (a) P_{peak} = 50.74 MPa, (b) P_{peak} = 20 MPa and (c) P_{peak} = 70 MPa.

C.4 Tensile strength
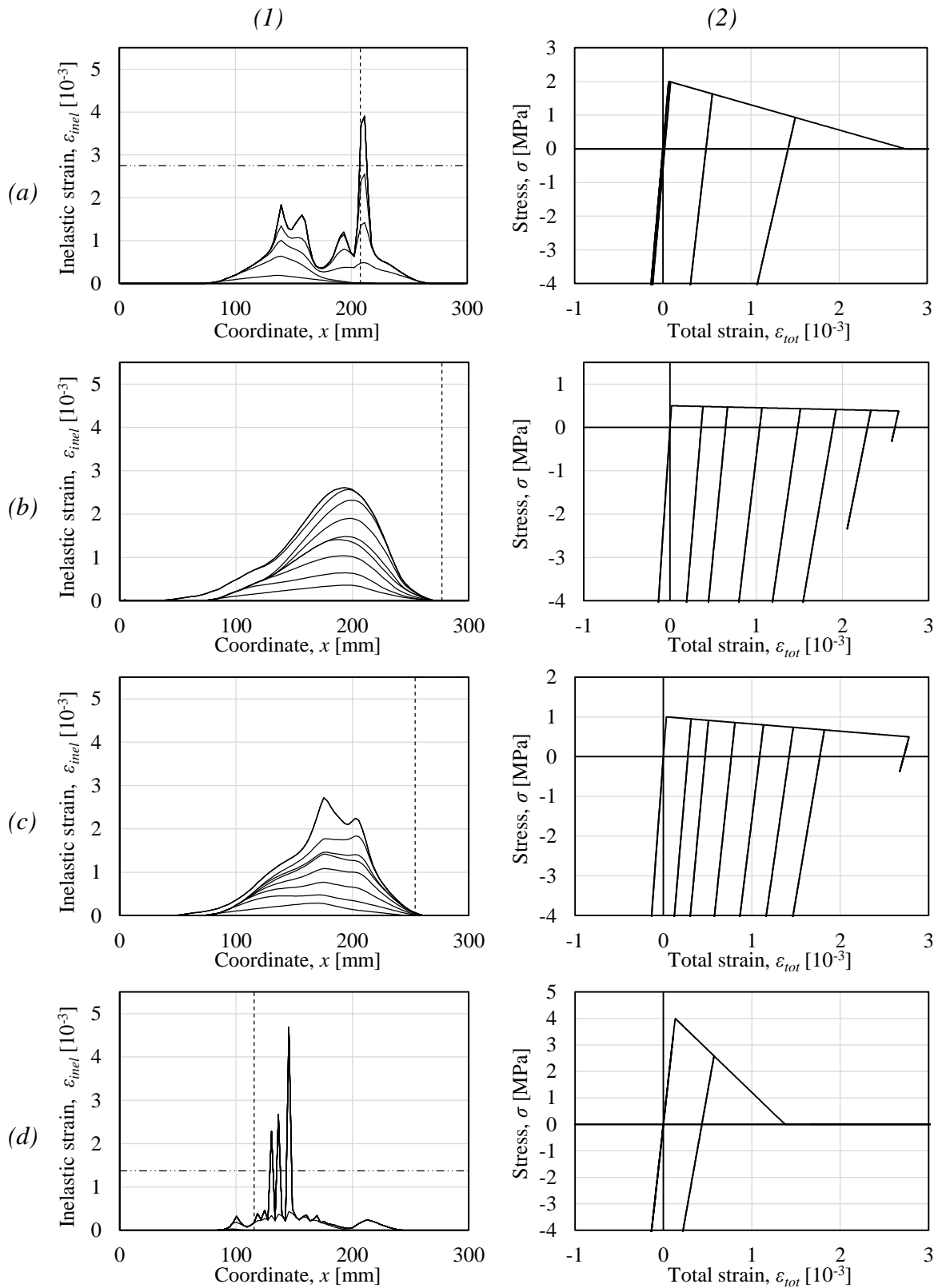
Figure C.4 *(1) Distribution of inelastic strains and (2) corresponding material response for tensile strength (a) $f_{ct} = 2$ MPa, (b) $f_{ct} = 0.5$ MPa, (c) $f_{ct} = 1$ MPa and (d) $f_{ct} = 4$ MPa.*

C.5　Number of elements

(1)　　　　　　　　　　　　　　　*(2)*

(a)

(b)

(c)

(d)

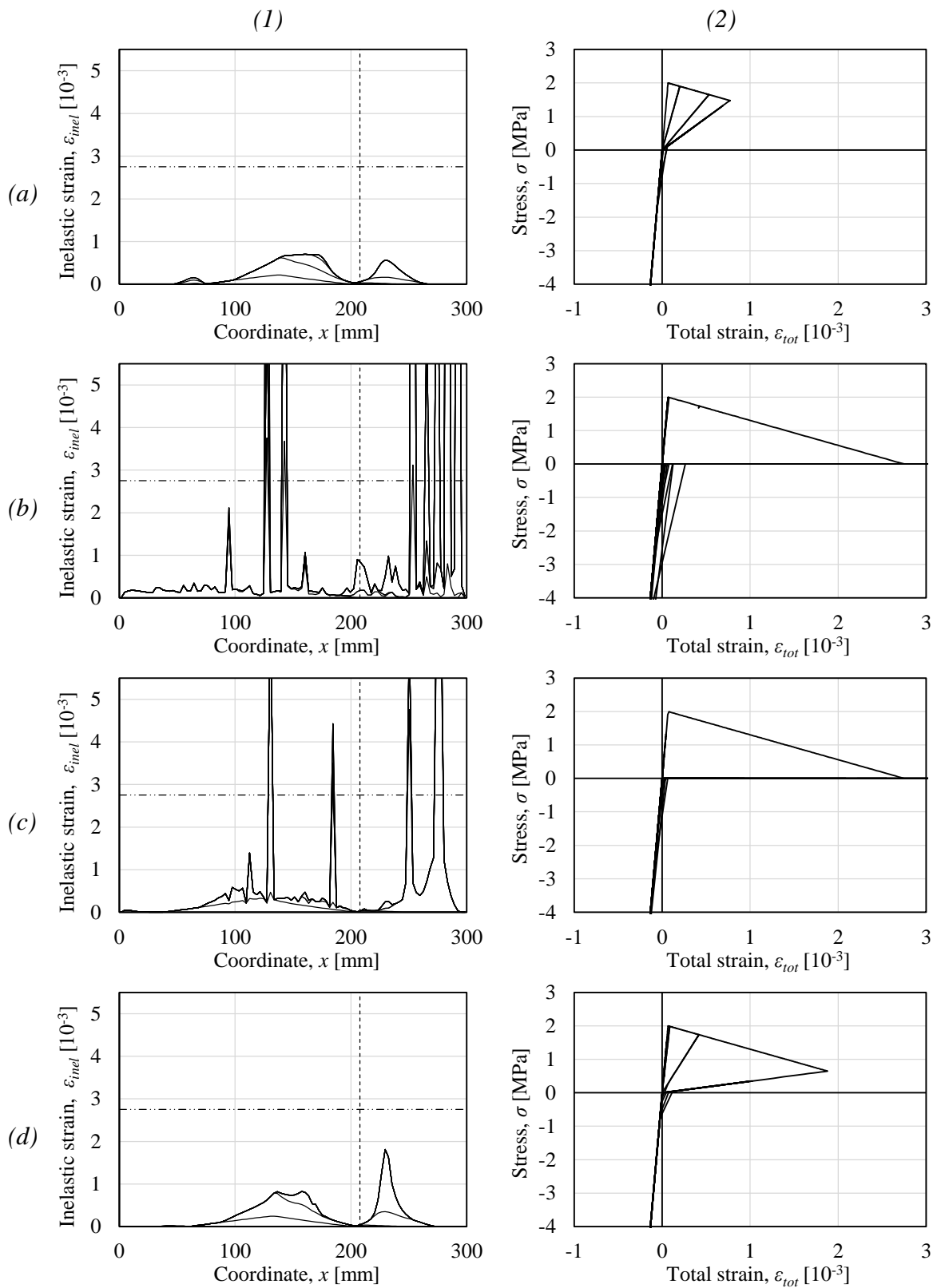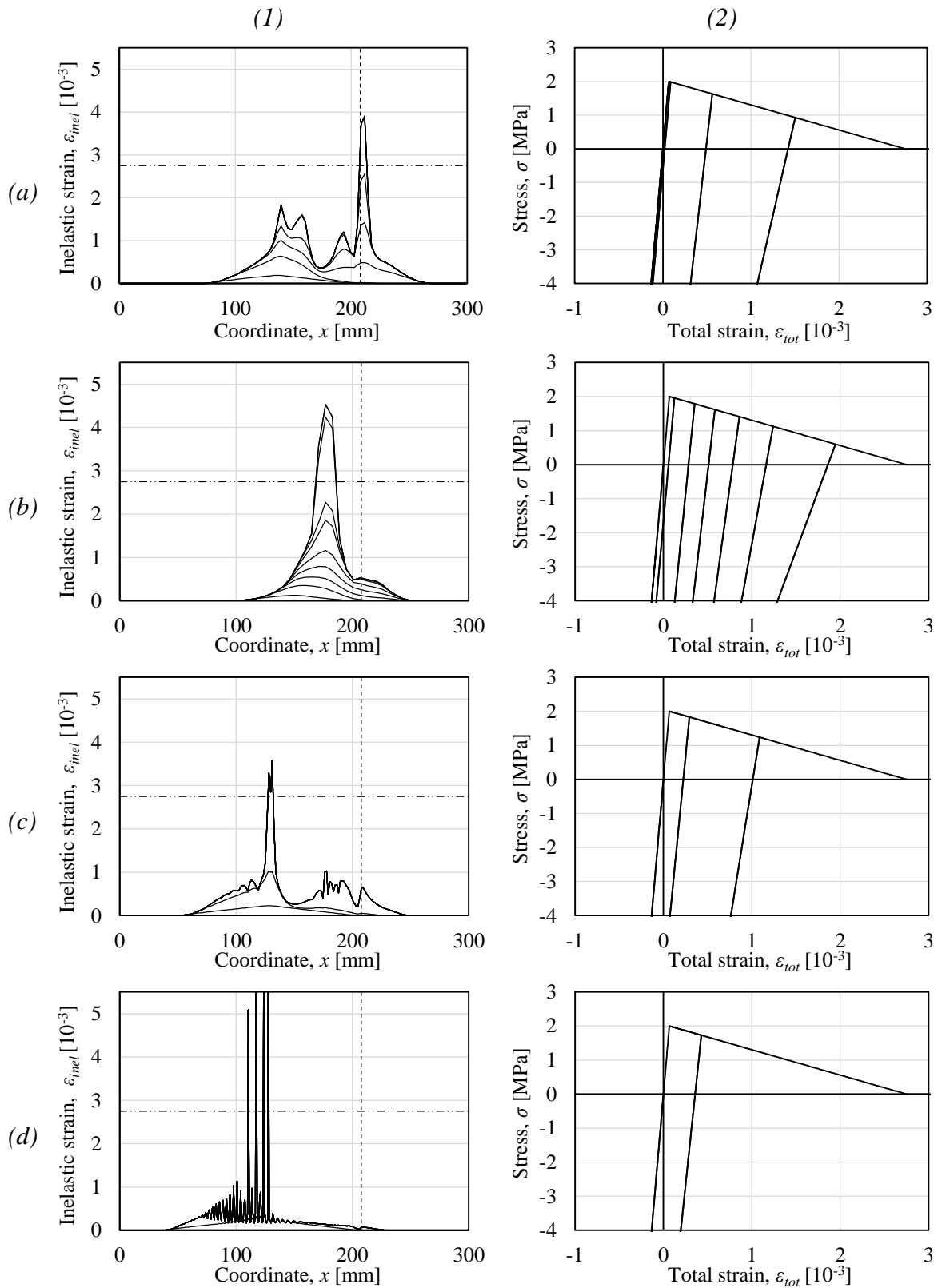*Figure C.5*　　*(1) Distribution of inelastic strains and (2) corresponding material response for number of elements (a) N = 100, (b) N = 50, (c) N = 200 and (d) N = 400.*

(1)   *(2)*

(a)
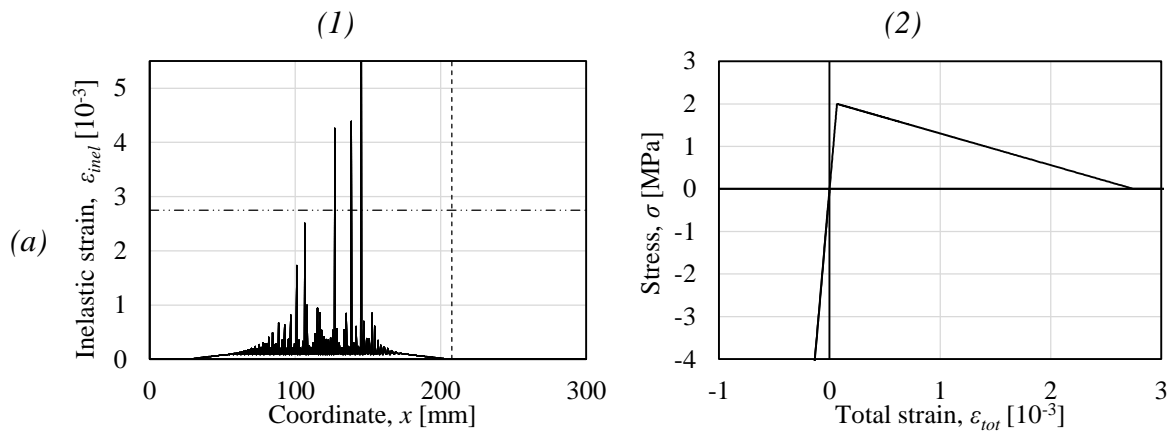
Figure C.6   *(1) Distribution of inelastic strains and (2) corresponding material response for number of elements (a) N = 800.*

C.6 Damping ratio

Figure C.7 *(1) Distribution of inelastic strains and (2) corresponding material response for damping (a) ξ = 1.0, (b) ξ = 0.1, (c) ξ = 0.3 and (d) ξ = 0.7.*

(a)

(1)   *(2)*

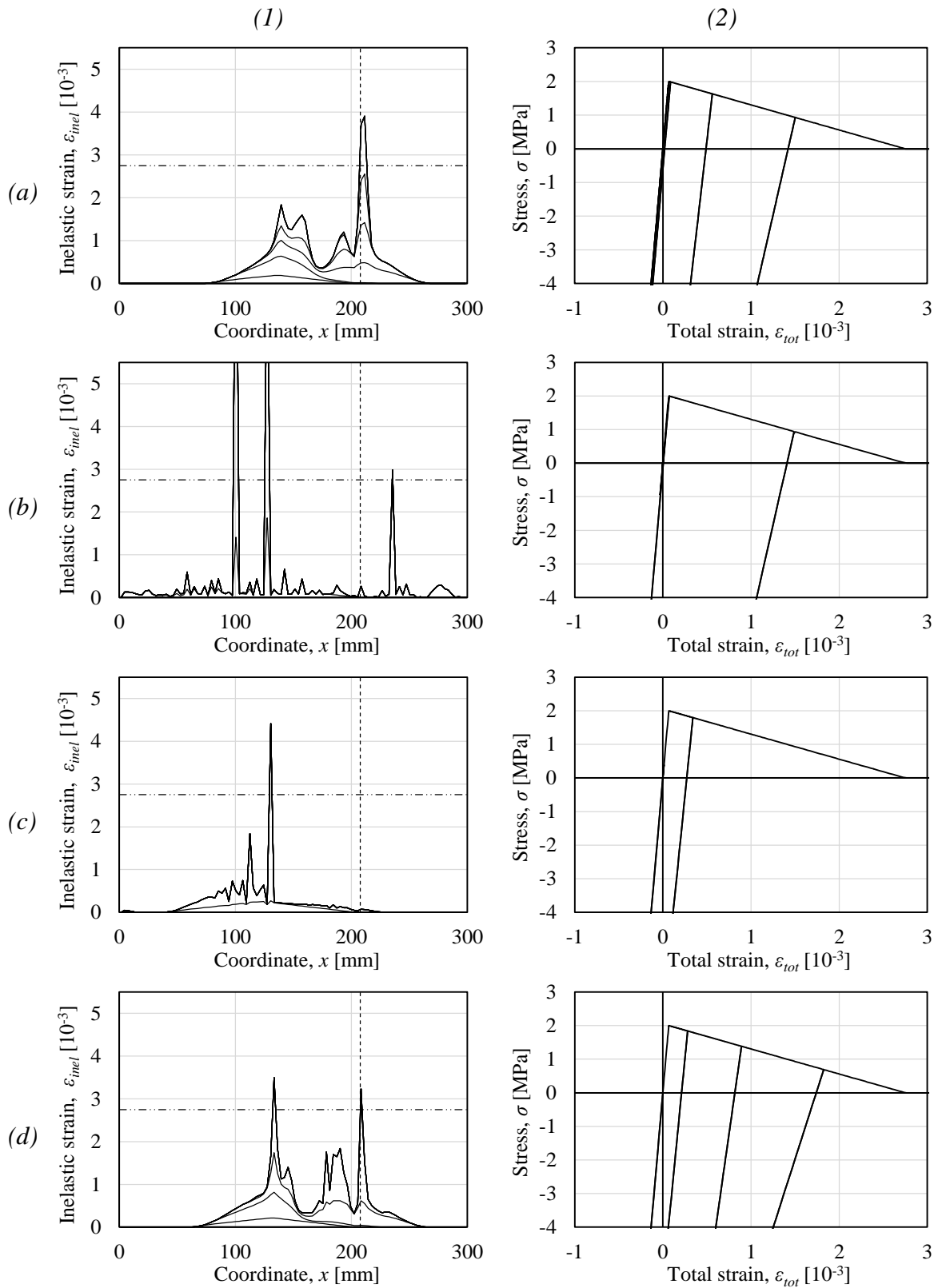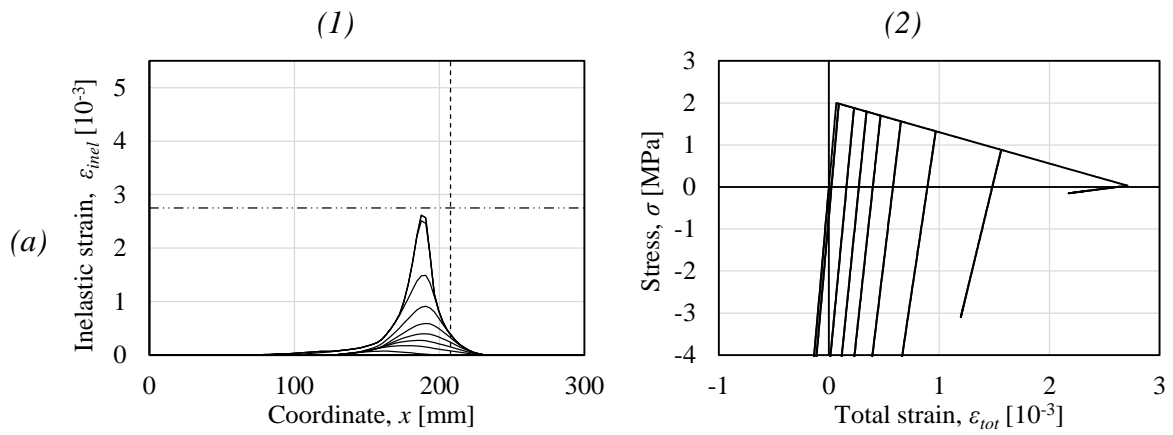*Figure C.8*   *(1) Distribution of inelastic strains and (2) corresponding material response for damping (a) $\xi = 3.0$.*

Appendix D   MATLAB code

```matlab
%===============================================%
% Model to evaluate spalling in concrete        %
%    (Plasticity model)                         %
% Written by Jonas Ekström 2014                 %
% Modified by Erik Flinck & Martin Olsson 2016 %
%===============================================%
clc
clear all
close all

tic
% == Variable input variation ===============
yield_s=2;                % Tensile strength [MPa]
Gf=132e-3;                % Fracture energy [N/mm]
ml=16;                    % Material length [mm]
l_frac=3;                 % Length of fracture zone
L=300;                    % Lenght [mm]
n_el=100;                 % Number of elements
p_peak=50.74;             % Peak pressure [MPa]
n_refl=20;                % Number of reflections in analysis
dt_load=1.31e-3;          % Load duration [s]
crit_p=0.3;               % Factor for critical time step [0-1]
damp=1.4;                 % Damping factor

% == Elastic material prop =================
E=30e3;                   % Young's modulus [MPa]
rho=2.35e-9;              % Concrete density [g/mm3]
A=1;                      % Element area [mm2]

% == Calculate ultimate crack opening ======
w_u=2*Gf/yield_s;

% == Calculate wave speed ==================
speed=sqrt(E/rho);
T1=L/speed;

if dt_load<2*T1
    disp('Short load duration');
    else
    disp('Long load duration');
end

% == Number of L-elastic travels ===========
load_duration=dt_load/T1;

% == Numerical input ====================
x=linspace(0,L,n_el+1);
x_m=linspace(x(2)/2,L-x(2)/2,n_el);
n_nodes=size(x,2);
el_dat=[1:n_el;1:n_nodes-1;2:n_nodes]';
E_el=E*ones(n_el,1);
yield=ones(n_el,1)*200;
yield(:)=yield_s;
size_=n_nodes;
```

```matlab
% == Element properties ====================
L_el=L/n_el;
ki=E*A/L_el;
mi=L_el*A*rho;
M_el=mi*ones(n_nodes,1);

% == Calculate ultimate strain =============
epsu=w_u/(ml*l_frac);

% == Hardening parameters ==================
Et=-yield_s/(epsu-yield_s/E);
H=Et/(1-Et/E);

% == Time step =============================
dtc=L_el/sqrt(E/rho);
dt=crit_p*dtc;

% == Analysis length ======================
t_analysis=L/sqrt(E/rho)*n_refl;
n_ts=t_analysis/dt;
n_ts_loaddur=n_ts/n_refl*load_duration;
n_ts=ceil(n_ts);

% == Start input 0-config ==================
I=eye(size_);
vec=zeros(size_,1);
Ki=[ki -ki; -ki ki];
K=zeros(size_);
Mg=zeros(n_nodes);
M=Mg;
Kg=1*(zeros(n_nodes));
qg=zeros(n_nodes,1);
d=zeros(n_nodes,1);
sigprev=zeros(n_el,1);
sigcurr=zeros(n_el,1);
epsprev=zeros(n_el,1);
epsncurr=zeros(n_el,1);
epscurr=zeros(n_el,1);
deps=zeros(n_el,1);
dincr=d;
Ct=E*ones(n_el,1);

% == Mass matrix for spring and bar elements
%Mi=0.5*[mi 0; 0 mi];
Mi=1/6*[2*mi mi; mi 2*mi];

% == First assembly =======================
for i=1:n_el

    m1=i;
    m2=i+1;
    xi=[x(i) x(i+1)]';
    vi=[m1 m2]';
    vg=i;
    de=d(vi);
    dincr_e=dincr(vi);

    % == Tangent stiffness matrix =========
    [sn,epsn,En]=pstress1d_BL(sigprev(i),epsprev(i),deps(i),E,...
                              Et,yield(i),epsu);
```

```matlab
        sigcurr(i)=sn;
        epscurr(i)=epsn;
        Ct(i)=En;

        nodes=el_dat(i,2:3);
        B=1/L_el*[-1 1];
        Kei=(A*L_el)*B'*Ct(i)*B;
        qei=(A*L_el)*B'*sigcurr(i);

        Kg(vi,vi)=Kg(vi,vi)+Kei;
        qg(vi)=qg(vi)+qei;

        Mi=M_el(i)/6*[2 1;1 2];
        Mg(nodes,nodes)=Mg(nodes,nodes)+Mi;

    end

    sigprev=sigcurr;
    epsprev=epscurr;

    % == Damping of system ====================
    delta=2/max(eig(inv(Mi)*Kei))^.5*damp;
    C=delta*Kg;

    % == Define acceleration, velocity etc. ====
    a=vec;
    v=vec;
    v(1)=0;
    u=vec;
    f=zeros(n_el,1);
    F=vec;
    F(1)=p_peak;

    t=0;
    color=['b','r'];

    Fint=zeros(n_el,n_ts+1);
    w_an=zeros(n_el,n_ts+1);
    strain=zeros(n_el,n_ts+1);
    plastic_strain=zeros(n_el,n_ts+1);

    count=0;
    k=1;
    loadprop=[];
    for ii=1:n_ts
        % == Pressure profile ==============
        %n=0 Rectangular
        %n=1 Triangular
        %n>1 Exponential
        n=1;

        Ft=F*(1-ii/n_ts_loaddur)^n;

        if Ft(1)>0
            loadprop(k)=Ft(1);
            k=k+1;
        end
        if (n_ts_loaddur-ii)/n_ts_loaddur<0
            Ft=F*0;
```

```matlab
        end

    u_i=u(:,ii)+dt*v(:,ii)+0.5*dt^2*a(:,ii);
    u(:,ii+1)=u_i;                    % Displacement vector u_n+1
    qg=zeros(n_nodes,1);

    for i=1:n_el
        m1=i;
        m2=i+1;
        xi=[x(i) x(i+1)]';
        vi=[m1 m2]';
        vg=i;
        de=u(vi,ii+1);
        dincr_e=u(vi,ii+1)-u(vi,ii);
        B=1/L_el*[-1 1];
        deps(i)=B*dincr_e;            % Strain increment vector e_n+1
        strain(i,ii+1)=B*u(vi,ii+1);

        %== Tangent stiffness matrix ==========
        [sn,epsn,En,sigB,sig0]=pstress1d_BL(sigprev(i),epsprev(i),...

deps(i),E,Et,yield(i),epsu);
        sigcurr(i)=sn;
        epsncurr(i)=epsn;
        nodes=el_dat(i,2:3);

        qei=(A*L_el)*B'*sigcurr(i);
        qg(vi)=qg(vi)+qei;

    end

    % == Input for next iteration =============
    a_i=(Mg+dt/2*C)\(Ft-C*(v(:,ii)+dt/2*a(:,ii))-qg);
    v_i=v(:,ii)+dt/2*(a(:,ii)+a_i);
    a(:,ii+1)=a_i;
    v(:,ii+1)=v_i;
    t=[t, t(ii)+dt];

    % == Input material response =============
    sigprev=sigcurr;
    epsprev=epsncurr;
    Fint(:,ii+1)=sigcurr;
    plastic_strain(:,ii+1)=epsncurr;

    prog=ceil(100*ii/n_ts);

    if ismember(prog,4:4:100)
        clc
        fprintf('Progress: %1.0f%% \n',(ii/n_ts)*100)
    end

end
FC=C*v;
toc


bb=[];
j=1;
for i=1:10:length(t);
```

```matlab
    place=t(i)*T1;
    tp=L*t(i)/T1;
    if t(i)>T1
        tp=L-L*(t(i)/T1-1);
        if t(i)>2*T1
            tp=L*(t(i)/T1-2);
            if t(i)>3*T1
                tp=L-L*(t(i)/T1-3);
            end
        end
    end
    subplot(4,1,1)
    plot(x,u(:,i),'-go')
    axis([0 L 0 max(max(u))])
    hold on
    plot(tp,0,'ro')
    hold off

    subplot(4,1,2)
    plot(x,v(:,i),'-ro')
    axis([0 L 0 max(max(v))])

    subplot(4,1,3)
    plot(x_m,Fint(:,i),'-o')
    axis([0 L -5 4])
    axis([0 L -50 5])
    hold on
    plot(x,FC(:,i),'k')
    plot([0 L],[yield_s yield_s],'b--')
    FF2(j)=getframe;
    hold off

    subplot(4,1,4)
    plot(x_m,plastic_strain(:,i),'-o')
    axis([0 L 0 2*epsu])
    hold on
    plot([0 L],[epsu epsu],'b')
    hold off
    j=j+1;
end

% == MOVIE ===================================
% movie2avi(FF2,'name','compression','none','fps',24)
```

```matlab
%===============================================%
% Function file for material model              %
%     (Plasticity model)                        %
% Written by Jonas Ekström 2014                 %
% Modified by Erik Flinck & Martin Olsson 2016  %
%===============================================%
function [sn,epsn,En,sigB,sig0]=pstress1d_BL(so,epso,de,E,...
                                   Et,yield,epsu)


H=Et/(1-Et/E);
if epso<epsu
    sig0=yield+H*epso;
else
    sig0=0;
end


sigB=so+E*de;

if (sigB)<=sig0
    sn=sigB;
    epsn=epso;
    En=E;
    %do nothing
else
    sn=sigB-E/(E+H)*(sigB-sign(sigB)*sig0);
    epsn=epso+(abs(sigB)-sig0)/(E+H);
    En=Et;

end
```

CHALMERS, *Civil and Environmental Engineering*, Master's Thesis BOMX02-16-26